Sergiy Mayilo

Exploiting Energy Transfer in Hybrid Metal and Semiconductor Nanoparticle Systems for Biosensing and Energy Harvesting
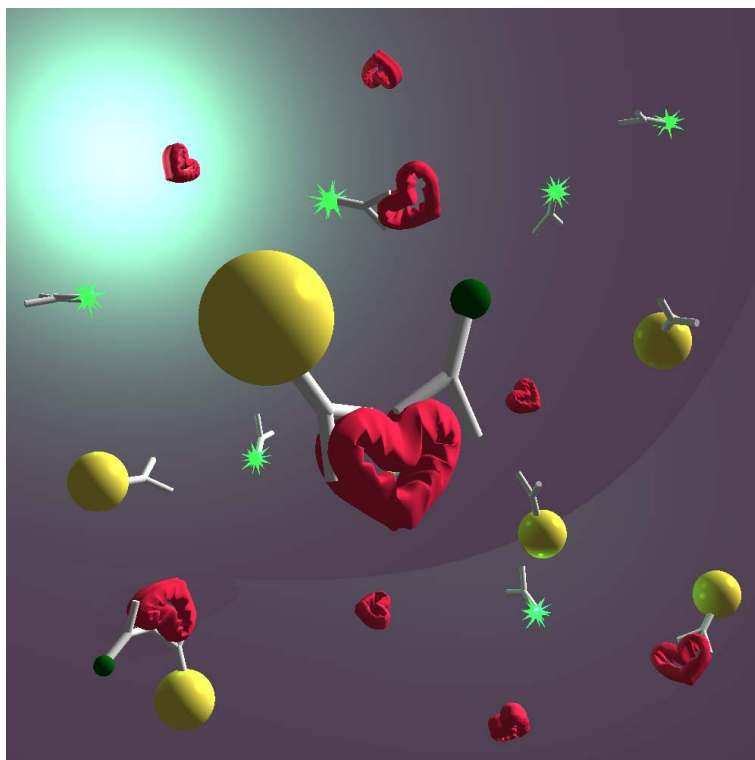
München 2009

Exploiting Energy Transfer in Hybrid Metal and Semiconductor Nanoparticle Systems for Biosensing and Energy Harvesting

Dissertation an der Fakultät für Physik

der Ludwig-Maximilians-Universität München

vorgelegt von

Sergiy Mayilo

aus Mykolayiv (Ukraine)

München, im Mai 2009

Contents

Abstract

In this work, gold and semiconductor nanoparticles are used as building blocks for nanostructures, in which energy transfer is investigated. Nanoparticles have size-dependent controllable optical properties. Therefore, they are interesting objects to study different aspects and applications of energy transfer.

Fluorescence quenching by gold nanoparticles is investigated and used to develop novel immunoassays for medically relevant molecules. The range of fluorescence quenching by gold nanoparticles is effective over longer distances than for dye molecules. The reason for this is the large absorption cross-section of gold nanoparticles and the radiative rate suppression of dyes caused by gold nanoparticles. The influence of gold nanoparticles on radiative and non-radiative rates of Cy3 and Cy3B dyes is studied here.

A competitive, homogeneous immunoassay for digoxigenin and digoxin, a drug used to cure heart diseases, is developed. Dye-labeled digoxigenin is bound to the gold nanoparticles functionalized with anti-digoxigenin antibodies, quenching the dye fluorescence. Unlabeled digoxigenin partially replaces the dye-labeled digoxigenin leading to an increase of fluorescence. The assay has a limit of detection of 0.5 nM in buffer and 50 nM in serum. Time resolved spectroscopy reveals that the quenching is due to energy transfer with an efficiency of 70%.

A homogeneous sandwich immunoassay for cardiac troponin T, an indicator of damage to the heart muscle, is developed. Gold nanoparticles and fluorophores are functionalized with anti-troponin T antibodies. In the presence of troponin T the nanoparticles and fluorophores form a sandwich structure, in which the dye fluorescence is quenched by a gold nanoparticle. The limit of detection of the immunoassay in buffer is 0.02 nM and 0.11 nM in serum. Energy transfer, with up to 95% efficiency, is responsible for the fluorescence quenching, as found through time resolved spectroscopy.

Energy transfer is demonstrated in clusters of CdTe nanocrystals assembled using three methods. In the first method, clusters of differently-sized water soluble CdTe nanocrystals capped by negatively charged mercaptoacid stabilizers are produced through electrostatic interactions with positively charged Ca^{2+} cations. The two other methods employ covalent binding through dithiols and thiolated DNA as linkers between nanocrystals. Energy transfer from smaller nanocrystals to larger nanocrystals in aggregates is demonstrated by means of steady-state and time-resolved photoluminescence spectroscopy, paving the way for nanocrystal-based light harvesting structures in solution.

Multi-shell onion-like CdSe/ZnS/CdSe/ZnS nanocrystals are presented. In these structures the CdSe core and the CdSe shell produce two emission peaks upon UV light excitation. When the emission peaks are well matched, the resulting emission appears as pure white light. The shade of the white light can be controlled by annealing the particles. Evidence for intra-nanocrystal energy transfer is presented.

Kurzfassung

In dieser Arbeit werden Gold- und Halbleiternanopartikel als Bausteine für Nanostrukturen eingesetzt, in denen Energietransfer untersucht wird. Nanopartikel haben größenabhängige, kontrollierbare optische Eigenschaften. Dadurch sind sie interessant für die Erforschung von unterschiedlichen Aspekten und Anwendungen von Energietransfer.

Fluoreszenzlöschung durch Gold-Nanopartikel wird untersucht und benutzt um neuartige Immunoassays für medizinisch relevante Moleküle zu entwickeln. Die Reichweite der Fluoreszenzlöschung durch Gold-Nanopartikel ist länger als mit Farbstoffen als Energieakzeptoren. Grund hierfür ist der große Absorptionsquerschnitt von Gold-Nanopartikel und die durch sie hervorgerufene Unterdrückung der strahlenden Rate. Der Einfluss der Gold-Nanopartikel auf die strahlende und nichtstrahlende Rate der Farbstoffe Cy3 und Cy3B wird hier untersucht.

Ein kompetitives, homogenes Immunoassay für Digoxigenin und Digoxin, ein Medikament, das bei Herzkrankheiten eingesetzt wird, wird entwickelt. Das mit Farbstoff markierte Digoxigenin wird an die mit Anti-Digoxigenin funktionalisierten Gold-Nanopartikel gebunden, und die Fluoreszenz wird gelöscht. Das nicht markierte Digoxigenin ersetzt zum Teil das mit Farbstoff markierte Digoxigenin, was zur Fluoreszenzerhöhung führt. Das Detektionslimit des Assays liegt bei 0.5 nM in Puffer und 50 nM in Serum. Zeitaufgelöste Spektroskopie zeigt, dass die Fluoreszenzlöschung durch den bis zu 70% effizienten Energietransfer von einem Farbstoffmolekül zum Gold-Nanopartikel verursacht wird.

Ein homogenes Sandwich-Immunoassay für kardiales Troponin T, einen Marker für Beschädigungen des Herzmuskels, wurde entwickelt. Gold-Nanopartikel und Farbstoffe werden mit Anti-Troponin T Antikörpern funktionalisiert. Sie bilden eine Sandwichstruktur in Anwesenheit des Troponins T, in der die Fluoreszenz durch Gold-Nanopartikel gelöscht wird. Das Detektionslimit des Assays in Puffer liegt bei 0,02 nM und 0,11 nM in Serum. Mithilfe zeitaufgelöster Spektroskopie wird nachgewiesen, dass der Energietransfer mit bis zu 95% Effizienz für die Fluoreszenzlöschung verantwortlich ist.

Energietransfer in Clustern von CdTe Nanokristallen, die durch drei Methoden zusammengefügt werden, wird demonstriert. Bei der ersten Methode werden Cluster aus CdTe Nanokristallen, die mit dem Stabilisator Merkaptosäure bedeckt sind, durch elektrostatische Wechselwirkungen mit Ca^{2+} Kationen hergestellt. Die beiden anderen Methoden verwenden die kovalente Bindung durch Dithiole und thiolisierte DNA als Verknüpfung zwischen den Nanokristallen. Energietransfer von kleinen zu größeren Nanokristallen in Aggregaten wird mithilfe zeitintegrierter und zeitaufgelöster Spektroskopie demonstriert, was einen Weg für nanokristallbasierte Lichtsammelkomplexe in Lösung zeigt.

Zwiebelartige CdSe/ZnS/CdSe/ZnS Nanokristalle mit mehrenen Schalen werden vorgestellt. In diesen Strukturen erzeugen der CdSe Kern und die CdSe Schale zwei Emissionspeaks unter UV-Licht Anregung. Wenn die beiden Emissionsfarben richtig angepasst sind, sieht die resultierende Emission weiß aus. Der Ton des Weißlicht kann durch Heizen der Teilchen kontrolliert werden. Anzeichen für intra-nanokristallischen Energietransfer werden präsentiert.

Publications on results of this thesis

- S. Sapra, S. Mayilo, T. A. Klar, A. L. Rogach, J. Feldmann
  Bright White Light Emission from Semiconductor Nanocrystals: by Chance and by Design
  Advanced Materials 2007, 19, 569-572

- S. Mayilo, J. Hilhorst, A. S. Susha, C. Höhl, T. Franzl, T. A. Klar, A. L. Rogach, J. Feldmann
  Energy Transfer in Solution-Based Clusters of CdTe Nanocrystals Electrostatically Bound by Calcium Ions
  Journal of Physical Chemistry C 2008, 112, 14589-14594

- S. Mayilo, B. Ehlers, M. Wunderlich, T. A. Klar, H.-P. Josel, D. Heindl, A. Nichtl, K. Kürzinger, J. Feldmann
  Competitive Homogeneous Digoxigenin Immunoassay Based on Fluorescence Quenching by Gold Nanoparticles
  Submitted

- S. Mayilo, M. Kloster, M. Wunderlich, F. Stefani, T. A. Klar, A. Nichtl, K. Kürzinger, J. Feldmann
  Cardiac Troponin T Sandwich Immunoassay Based on Long-Range Fluorescence Quenching by Gold Nanoparticles
  Manuscript in preparation

Further publications

- A. Bek, R. Jansen, M. Ringler, S. Mayilo, T. A. Klar, J. Feldmann
  Fluorescence Enhancement in Hot Spots of AFM-Designed Gold Nanoparticle Sandwiches
  Nano Letters 2008, 8 (2), 485-490

- A. Sukhanova, A. S. Susha, A. Bek, S. Mayilo, A. L. Rogach, J. Feldmann, B. Reveil, B. Donvito, J. H. M. Cohen, I. Nabiev
  Nanocrystal-Encoded Fluorescent Microbeads for Proteomics: Antibody Profiling and Diagnostics of Autoimmune Diseases
  Nano Letters 2007, 7 (8), 2322-2327

Talks at conferences and workshops

- *Energy Transfer in Solution-Based Complexes of CdTe Nanocrystals Electrostatically Bound by Calcium Ions*
  S. Mayilo, J. Hilhorst, A.S. Susha, C. Höhl, T.A. Klar, A.L. Rogach, J. Feldmann
  IDK-NanoBioTechnology summer school, Aiterbach, 07/2008

- *Energy Transfer in Solution-Based Complexes of CdTe Nanocrystals Electrostatically Bound by Calcium Ions*
  S. Mayilo, J. Hilhorst, A.S. Susha, C. Höhl, T.A. Klar, A.L. Rogach, J. Feldmann
  72d Annual Meeting of the DPG, Berlin, 02/2008

- *Fluorescence Biosensors*
  S. Mayilo
  Workshop "Nano for Life Science", Riezlern (Austria), 06/2007

- *Tailor Made White Light Emission from Semiconductor Nanocrystals*
  S. Mayilo, S. Sapra, T. A. Klar, A. L. Rogach, J. Feldmann
  World of Photonics Congress, Munich, 06/2007

- *Balancing the White Light Shade of Dual-Color Emitting Nanocrystals*
  S. Mayilo, S. Sapra, T.A. Klar, A.L. Rogach, J. Feldmann
  71st Annual Meeting of the DPG, Regensburg, 03/2007

Poster contributions to conferences and workshops

- *Using Nanoscale Architectures for Shaping the Emission Spectra of Semiconductor Nanocrystals*
  S. Mayilo, J. Hilhorst, A.S. Susha, F. Stefani, A. Lutich, S. Sapra, T.A. Klar, A.L. Rogach, J. Feldmann
  Materials Research Society 2008 Fall Meeting, Boston (USA), 12/2008

- *Competitive Homogeneous Hapten Immunoassay Based on Fluorescence Quenching by Gold Nanoparticles*
  S. Mayilo, B. Ehlers, M. Wunderlich, T. A. Klar, H.-P. Josel, D. Heindl, A. Nichtl, K. Kürzinger, J. Feldmann
  CeNS Workshop "Complex nanosystems: assembly, control and functionality", Venice (Italy), 09/2008

- *Energy Transfer in Solution-Based CdTe Nanocrystals Electrostatically Bound by Calcium Ions*
  S. Mayilo, J. Hilhorst, A.S. Susha, C. Höhl, T. Franzl, T.A. Klar, A.L. Rogach, J. Feldmann
  Workshop "Optical Properties of Coupled Semiconductor and Metallic Nanoparticles", Dresden, 07/2008

- *Energy Transfer in Solution-Based Complexes of CdTe Nanocrystals Electrostatically Bound by Calcium Ions*
  S. Mayilo, J. Hilhorst, A.S. Susha, C. Höhl, T.A. Klar, A.L. Rogach, J. Feldmann
  NIM-workshop on "Interactions in hybrid nanosystems", Frauenwörth, 05/2008

- *Nanocrystal-Encoded Microbeads for Diagnostics of Autoimmune Diseases*
  S. Mayilo, A.S. Susha, A. Bek, J. Feldmann, A.L. Rogach, A. Sukhanova, B. Reveil, B. Donvito, J.H.M. Cohen and I. Nabiev
  Workshop "Macromolecular Systems for NanoScience - Chemistry, Physics and Engineering Aspects", Irsee, 09/2007

- *Balancing the White Light Shade of Dual-Color Emitting Nanocrystals*
  S. Mayilo, S. Sapra, T.A. Klar, A.L. Rogach, J. Feldmann
  The NINT-CeNS Winter School on Nanotechnology Convergence, Edmonton (Canada), 03/2007

- *Balancing the White Light Shade of Dual-Color Emitting Nanocrystals*
  S. Mayilo, S. Sapra, T.A. Klar, A.L. Rogach, J. Feldmann
  CeNS Workshop "Emerging Nanosystems - From Quantum Manipulation to Nanobiomachines", Venice (Italy), 09/2006

For my parents

Моїм батькам

1. Introduction

Energy transfer is a photophysical process inherent to many molecular and nano-structured systems. It involves transfer of excitation energy from one part of the system to an other. This short scale energy migration that takes place in natural processes, such as photosynthesis [1], has recently found a great number of technological applications in biosensing [2], light-emitting diodes [3], lasing [4] and solar cells [5].

Nanoparticles open new ways to investigate the characteristics and applications of energy transfer due to their unique and controllable optical properties. This work is focused on the employment of gold nanoparticles (AuNPs) as energy acceptors, CdTe nanocrystals (NCs) as both energy donors and acceptors and multi-shell CdSe/ZnS/CdSe/ZnS nanocrystals as objects in which energy can be transferred within the same nanoparticle.

Energy transfer is often referred to as a "nanoscopic ruler" enabling the determination of distances in the nanometer range due to its strong donor to acceptor distance dependence. This process can take place for fluorophore separations of 4-8 nm [6]. AuNPs allow this distance limit to be overcome. They are efficient energy acceptors and quench fluorescence of a molecule over distances longer than 10 nm [7–9]. Energy transfer takes place from the molecular transition dipole to the collective oscillation of the electron gas (plasmon) in the AuNP.

AuNPs are superior quenchers for a number of reasons. Due to the size of the particles, the distance dependence of the energy transfer rate is less steep than the well-known R^{-6} in the case of a dye as an acceptor. Due to their symmetry, energy transfer to spherical AuNPs can take place for any orientation of the dye transition dipole moment in respect to the surface of AuNPs unlike in dye-dye systems [10]. AuNPs have 10^4-10^5 times larger absorption cross-sections than dyes [11]. Most importantly, AuNPs have a special property

to quench fluorescence due to radiative rate suppression [12], which is not the case for dye acceptors.

The outstanding fluorescence quenching properties of AuNPs make them attractive for creating biosensors for proteins because these have sizes often larger than 10 nm. Therefore, energy transfer with conventional donors and acceptors applicable up to about 7 nm would fail. The aim of this work was to investigate long-distance fluorescence quenching by AuNPs in bioconjugated systems and to develop small molecule and protein biosensors based on these findings.

The majority of the publications on the use of fluorescence quenching by AuNPs does not study the quenching mechanism in detail. This could lead to artifacts because AuNPs are also known to enhance fluorescence under certain conditions [13]. The understanding of the underlying physics of fluorescence quenching processes would allow optimization of the biosensors in future because the critical parameters influencing quenching efficiency can be identified.

In this work biosensors of the immunoassay type are developed. Immunoassays are biosensors, which involve the use of antibodies that can specifically bind to analyte molecules. AuNPs are functionalized with antibodies. Fluorescent markers can be attached to the analyte molecule. Fluorescence quenching is expected upon binding of the labeled analyte to the antibodies on the AuNP. This approach can be used to detect small molecules. Proteins are large molecules, to which several antibodies can bind at different places. AuNPs and fluorescent markers can be attached to two different antibodies sensitive to two positions on the protein. The addition of the protein would result in the formation of a sandwich structure where dye is brought close to the AuNP and quenched.

The development of biosensors based on the suggested approach promises a number of advantages. First, AuNPs are not toxic to cells and can be applied safely in biological systems [14]. Second, the proposed detection scheme uses a homogeneous approach, which does not involve separation of unbound fluorescent markers. This approach is thus simpler and faster than the heterogeneous (involving separation) approach used in many established immunoassays. The usage of AuNPs in biosensors has resulted in a significant amount of research, which is summarized in a number of recent reviews on the topic [15–17]. This thesis

presents the first immunoassay based on fluorescence quenching by AuNPs in an immunoassay of sandwich type for proteins.

The second part of the work presented in this thesis deals with energy transfer in colloidal semiconductor nanocrystals. Controlled assemblies of NCs, in which energy transfer takes place, are useful in a number of applications. It was recently theoretically demonstrated that optical gain of NCs pumped by energy transfer can be increased [18], which is of interest for NC-based lasing. NCs are also promising materials for light emitting diodes [19, 20] and photovoltaics [21, 22]. NCs are more stable than dyes in terms of bleaching. This means that eventual devices could have a longer lifetime using NCs than organic dye molecules. Moreover, NCs have relatively large quantum yields and extinction coefficients 10-100 times larger than dyes [23].

Cascaded energy transfer with NCs was demonstrated in layers [24, 25] and on nanowires [26], but creating structures that pump energy into a single NC in the center stays a challenge. There are only few studies in this direction [27]. The aim of this work was to create solution-based aggregates of nanocrystals in a controlled way, enabling energy transfer cascades from the particles with a broader band gap to those with a narrower band gap. The approaches to achieve this aim were electrostatic conjugation through Ca^{2+} ions and controlled covalent conjugation using dithiol surface stabilizers and thiolated DNA.

Recently, the creation of multi-shell NCs has become possible. Multi-shell NCs consisting of CdSe and ZnS layers were shown to have several emission lines [28]. CdSe/ZnS/CdSe/ZnS particles are very interesting as biolabels and single photon sources [29]. However the question about the interaction between the CdSe shell and the CdSe core separated by a ZnS layer stays largely unresolved. The aim of this thesis was to investigate intra-NC energy transfer.

The main experimental technique used in this work for the investigation of dye-AuNP- and NC-based systems is time resolved photoluminescence spectroscopy. This technique is perfectly suited to study the energy transfer process, which has peculiar time-dependent energy dynamics. Fluorescence intensity of dye and NCs after pulsed laser excitation can be followed in time. This allows the determination of the changes in the radiative and non-radiative rates of the donor and acceptor. Consequently, energy transfer rate and efficiency can be calculated.

This thesis consists of nine chapters. Chapters 5, 6, 7 and 8, containing experimental results, start with short introductions and are closed with conclusions.

Chapter 2 introduces the theoretical background and main concepts that are used for this work. The theory of energy transfer, mechanisms of interactions of AuNPs with dye molecules as well as the main concepts of biosensing and optical properties of semiconductor nanocrystals are presented.

Chapter 3 introduces the materials used for the experiments and describes the methods of sample preparation.

Chapter 4 describes the experimental techniques used in this work. These included steady state and time resolved fluorescence spectroscopy as well as steady state absorption spectroscopy.

Chapters 5 contains the results on fluorescence quenching by AuNPs in a competitive small molecule immunoassay.

Chapter 6 describes fluorescence quenching in the sandwich immunoassay, in which AuNP and a dye molecule are separated by a protein, providing a large dye-AuNP distance.

Chapter 7 contains results of investigations of energy transfer in CdTe clusters. Three approaches are presented: electrostatic conjugation with Ca^{2+} ions and covalent binding with the help of dithiols and thiolated DNA.

Chapter 8 presents the measurements on white light-emitting multi-shell nanocrystals. Energy transfer from the CdSe shell to the CdSe core is discussed.

Chapter 9 summarizes all the obtained results and puts them into the present scientific context. Further possibilities of research are shown.

The appendix contains equations used for binding kinetics simulations in a sandwich-type immunoassay.

2. Concepts and theoretical background

2.1 Energy transfer

Energy transfer can take place between two molecules, semiconductor NCs or AuNPs. When one molecule, called a donor, is optically excited, it can transfer its energy non-radiatively to the other molecule, called an acceptor. The interaction between donor and acceptor can be mediated through Coulombic or intermolecular orbital overlap interactions.

Coulombic interaction has long range ($>$ 1 nm) and short-range ($<$ 1 nm) components. In the former, the dipole-dipole interaction is dominant (Förster mechanism). In the latter, multi-polar effects play a significant role. In Coulombic interaction the donor in the excited state relaxes to the ground state and the acceptor is simultaneously excited (figure 2.1). It is the predominant interaction for allowed optical transitions.

Intermolecular orbital overlap requires that wave functions of two interacting systems overlap. Therefore it can take place only when donor-acceptor distances are short ($<$ 1 nm). The interaction process can be described as electron exchange between the donor and the acceptor (figure 2.1). This interaction dominates when transitions are optically forbidden.
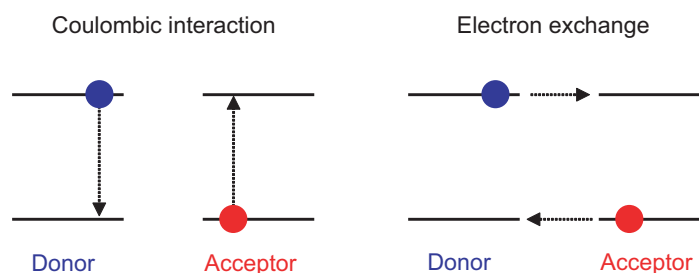
Figure 2.1: Schemes of the energy transfer mediated through Coulomb and electron exchange interactions. Adapted from [30].

2.1.1   Förster resonance energy transfer (FRET)

The process of non-radiative energy transfer through Coulomb interaction was first predicted by Perrin [31]. Förster developed a classical and later on a quantum mechanical description of this phenomenon [32]. The theory and main concepts of Förster energy transfer are well presented in a number of up-to-date reviews [33, 34] and books [6, 30, 35, 36].

The Förster theory is based on the assumption that molecular transition dipoles can be treated as point dipoles. According to the Förster theory, the energy transfer rate Γ_{ET} is

$$\Gamma_{ET} = \frac{1}{\tau_D} \left(\frac{R_0}{R} \right)^6, \tag{2.1}$$

where τ_D is the donor fluorescence lifetime in the absence of an acceptor, R is the distance between the donor and the acceptor point dipoles and R_0 is the so called Förster radius, at which the probability of energy transfer from the donor is equal to the probability of its spontaneous decay. R_0 can be determined from spectral properties of donor and acceptor as

$$R_0^6 = \frac{9000(\ln 10)\kappa^2 Q_D J}{128\pi^5 N_A n^4}. \tag{2.2}$$

In this formula κ^2 is the orientation factor defined as $\kappa^2 = (\cos\theta_{DA} - 3\cos\theta_D \cos\theta_A)^2$, where θ_{DA} is the angle between the transition dipole moments of donor and acceptor, θ_D and θ_A are angles between donor and acceptor transition moments and the distance vector $\mathbf{R}$ between them. The orientation factor κ^2 can have values between 0 (when transition moments are perpendicular) and 4 (parallel transition moments) depending on the relative orientations of the two transition dipole moments. In the case of random orientation it is in average equal to 2/3 [30]. Q_D is the quantum yield of the donor in the absence of the acceptor. $J = \int_0^\infty I_D(\lambda)\varepsilon_A(\lambda)\lambda^4 \mathrm{d}\lambda$ describes the overlap between the normalized ($\int_0^\infty I_D(\lambda)\mathrm{d}\lambda = 1$) fluorescence emission spectrum of the donor $I_D(\lambda)$ and the molar absorption coefficient of the acceptor $\varepsilon_A(\lambda)$. N_A is the Avogadro constant and n is the refractive index of the surrounding medium.

The efficiency of energy transfer is defined as

$$
\begin{aligned}
\Phi_{ET} &= \frac{\Gamma_{ET}}{\Gamma_D + \Gamma_{ET}} & (2.3) \\
&= 1 - \frac{\tau_{DA}}{\tau_D} & (2.4) \\
&= \frac{1}{1 + (R/R_0)^6}, & (2.5)
\end{aligned}
$$

where Γ_{ET} is the energy transfer rate, Γ_D is the radiative rate of the donor and τ_{DA} is the donor lifetime in the presence of the acceptor.

The theory implies several conditions that need to be considered in choosing a working donor-acceptor pair. There must be an overlap between the emission spectrum of the donor and absorption spectrum of the acceptor. Additionally, the transition dipole moments of the donor and acceptor should not be oriented perpendicular to each other. Energy transfer normally takes place when donor and acceptor are situated not further than 7 nm from each other.

The fact that energy transfer takes place in a given donor-acceptor system can be noticed from several experimental observations [37]. The fluorescence intensity and the excited state lifetime of the donor are decreased. If the acceptor is fluorescent, an increase or appearance of the acceptor fluorescence is observed. A peak appears in the photoluminescence excitation spectrum of the acceptor at the wavelength corresponding to the donor absorption. A characteristic R^{-6} energy transfer efficiency behavior upon the changing donor-acceptor distance is observed. The shapes of the donor and acceptor spectra remain unchanged.

It should be noted that the Förster theory presented here holds for the case of very weak coupling [30]. This means that the interaction energy is much smaller than the vibronic and absorption bandwidth. In this case, the energy transfer rate is proportional to the sixth power of the donor-acceptor distance. In the other two regimes, called strong coupling (interaction energy is larger than the vibronic and absorption bandwidth) and weak coupling (interaction energy is smaller than the vibronic bandwidth, but larger than the absorption bandwidth), the energy transfer rate is proportional to the third power of the donor-acceptor distance [30].

2.1.2 Dexter energy transfer

If the distance between donor and acceptor is very small (typically less than 1 nm) energy transfer is mediated through exchange interactions due to intermolecular orbital overlap. This type of energy transfer was first theoretically described by Dexter [38]. The energy transfer rate in this case has the following distance dependence

$$\Gamma_{ET,Dexter} \sim Je^{-2R/l}, \tag{2.6}$$

where J is the spectral overlap between the normalized donor emission and acceptor absorption spectra $J = \int_0^\infty I_D(\lambda)\varepsilon_A(\lambda)\mathrm{d}\lambda$, R is the donor-acceptor distance and l is the typical penetration depth of the wave function in the environment.

2.2 Interactions between dyes and gold nanoparticles

2.2.1 Plasmons in gold nanoparticles

The skin depth of bulk gold for visible light is 35 nm [39]. Therefore, the incident light can go through the AuNPs of diameters of 10 and 20 nm. The electromagnetic wave thus leads to a polarization of a particle. Electrons are shifted to one side of the particle and the atomic cores remain as a positive charge on the other side of the particle upon illumination (figure 2.2). The Coulombic attraction of electrons and positive atomic cores leads to the collective oscillatory movement of the electrons in the particle. This collective oscillation is called a plasmon-polariton, often referred to simply as *plasmon* in the literature.
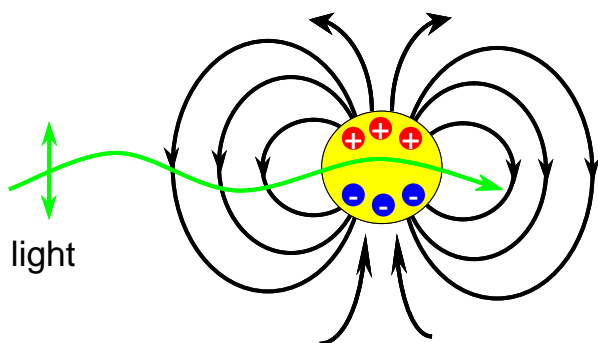
Figure 2.2: The incident light wave induces a collective oscillation of the electron gas in a AuNP. This oscillation is described as a quasi-particle called a plasmon. Therefore, a dipole moment can be ascribed to the AuNP, which interacts with the transition dipole moment of the dye in its vicinity.

2.2.2 Influence of a gold nanoparticle on dye in its vicinity

AuNPs influence the emission of dye molecules in several ways. The fluorescence signal from the molecule close to an AuNP can be described as

$$S \sim K(\hat{\mathbf{d}}, \mathbf{R})\Phi(\hat{\mathbf{d}}, \mathbf{R}),$$ (2.7)

where $K(\hat{\mathbf{d}}, \mathbf{R})$ is the enhancement factor and $\Phi(\hat{\mathbf{d}}, \mathbf{R})$ is the quantum efficiency of the molecule [40, 41]. $\hat{\mathbf{d}}$ is the unit vector in the direction of the molecule's transition dipole $\mathbf{d}$. $\mathbf{R}$ is the radius vector of the molecule in relation to the center of the AuNP. In the presence of the gold nanoparticle the parameters $K(\hat{\mathbf{d}}, \mathbf{R})$ and $\Phi(\hat{\mathbf{d}}, \mathbf{R})$ are influenced.

The enhancement factor is defined as the ratio of excitation rates of the dye molecule with and without an AuNP

$$K(\hat{\mathbf{d}}, \mathbf{R}) = \frac{|\mathbf{d} \cdot \mathbf{E}_{loc}(\mathbf{R})|^2}{|\mathbf{d} \cdot \mathbf{E}_{inc}(\mathbf{R})|^2},$$ (2.8)

where $\mathbf{E}_{inc}(\mathbf{R})$ is the incident electric field at the position of the molecule without the AuNP and $\mathbf{E}_{loc}(\mathbf{R})$ is the local electric field in presence of the AuNP. The incident excitation field $\mathbf{E}_{inc}$ induces a dipole moment $\mathbf{p} = 4\pi\alpha\mathbf{E}_{inc}$ in the AuNP, where α is the electrostatic polarizability of the AuNP. This leads to a change in the local field around the particle $\mathbf{E}_{loc}(\mathbf{R}) = \mathbf{E}_{inc}(\mathbf{R}) + \mathbf{E}_{scat}(\mathbf{p}, \mathbf{R})$, where an additional scattered field $\mathbf{E}_{scat}(\mathbf{p}, \mathbf{R})$ due to the dipole in the AuNP appears. Thus, the enhancement of the absorption rate would also lead to an increased fluorescence emission intensity without modifying the excited state lifetime [42]. When $\mathbf{R}$, $\mathbf{p}$ and $\mathbf{d}$ are co-linear, the enhancement of excitation is maximal [41].

The second parameter in equation 2.7 is the quantum efficiency of the molecule

$$\Phi(\hat{\mathbf{d}}, \mathbf{R}) = \frac{\Gamma_r(\hat{\mathbf{d}}, \mathbf{R})}{\Gamma_r(\hat{\mathbf{d}}, \mathbf{R}) + \Gamma_{nr}(\hat{\mathbf{d}}, \mathbf{R})}$$ (2.9)

$$= \frac{\Gamma_r(\hat{\mathbf{d}}, \mathbf{R})}{\Gamma_{tot}(\hat{\mathbf{d}}, \mathbf{R})}$$ (2.10)

where $\Gamma_r(\hat{\mathbf{d}}, \mathbf{R})$ and $\Gamma_{nr}(\hat{\mathbf{d}}, \mathbf{R})$ are the radiative and non-radiative decay rates of the molecule, $\Gamma_{tot}(\hat{\mathbf{d}}, \mathbf{R})$ is the total decay rate, which is equal to the reciprocal value of the experimentally measurable fluorescence lifetime of a molecule $\tau = \frac{1}{\Gamma_{tot}}$.

(a) constructive interference   (b) destructive interference
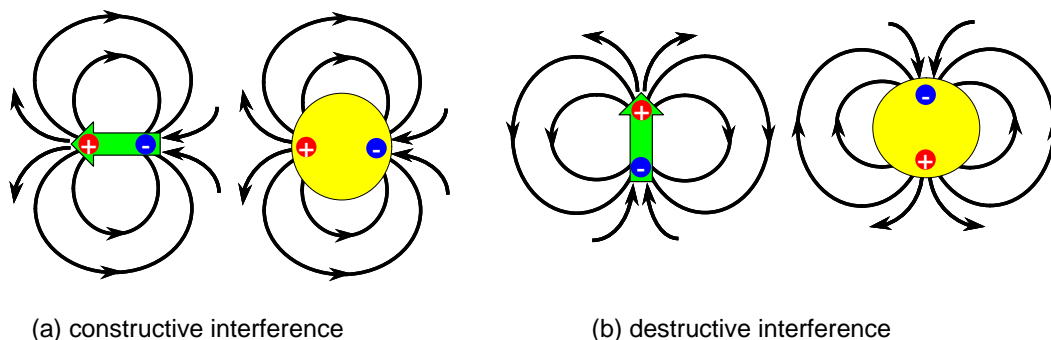
Figure 2.3: Constructive (a) and destructive (b) interference of the dipole fields of the dye and the AuNP lead to the enhancement or to suppression of the radiative rate of the molecule respectively.

Both radiative and non-radiative rates are modified in the presence of an AuNP resulting in a change of the fluorescence lifetime $\tau' = 1/\Gamma'_{tot} = 1/(\Gamma'_r + \Gamma'_{nr})$. The parameters are designated with a prime in the following when they describe processes in the vicinity of the AuNP.

In the case of the radiative rate, it is the dipole-dipole interaction between the transition dipole moment of the dye and the image dipole in the AuNP that plays a role. The relative orientation of these dipole moments determines the resulting effect on the radiative rate (figure 2.3). In the case of tangential orientation of the dye dipole moment to the surface of the AuNP, the total dipole moment will decrease and consequently the radiative rate will decrease [12, 43]. If the molecule's transition dipole moment is oriented perpendicular to the AuNP surface, the total dipole moment will increase leading to enhanced fluorescence [13, 44]. This situation can simply be described as interference of two dipoles. Interference is constructive in the case of perpendicular orientation and destructive in the case of parallel orientation (figure 2.3).

The non-radiative rate of the molecule in the presence of the AuNP $\Gamma'_{nr} = \Gamma_{nr} + \Gamma_{ET}$ is increased because it obtains an additional contribution Γ_{ET} due to energy transfer to the AuNP. In contrast to the energy transfer between two dye molecules, the orientational factor takes values from 1 to 4 depending on the dye-AuNP orientation [45]. This means that energy transfer between the dye and the AuNP takes place at any orientation of the dye to the AuNP surface. Another distinct feature of AuNPs as energy acceptors is that they can

quench fluorescence over longer distances than conventional dyes. The distance can reach up to 40 nm for particle diameters of 5 to 40 nm [9]. This fact can be explained by the following simple reasoning. Energy transfer rate from a dye to a gold surface obeys a R^{-3} distance dependence [46]. The dependence is R^{-6} for the the energy transfer rate to another point dipole [47]. Therefore, an AuNP that is in the middle between these two limiting cases will have the energy transfer rate distance dependence following the $R^{-\alpha}$, where α is between 3 and 6. Moreover, due to the high absorption cross-section of AuNPs the Förster radius of an AuNP would be longer than for conventional dyes because the absorption spectrum of the acceptor $\varepsilon_A(\lambda)$ in the overlap integral is not normalized: $R_0^6 \sim \int_0^\infty I_D(\lambda)\varepsilon_A(\lambda)\lambda^4 \mathrm{d}\lambda$.

Generally, because of different distance dependencies of all the discussed factors, AuNPs can cause both enhancement and quenching of molecular fluorescence. The total effect depends on the relative orientation of the molecular transition dipole moment and the surface of the AuNP and the separation distance between the two [13].

2.2.3 Theoretical approaches to describe dye-AuNP interactions

A number of theoretical models have been developed to model the interactions of a molecule and an AuNP. The Förster model for energy transfer introduced above cannot describe this system properly because an AuNP can hardly be treated as a point dipole. Moreover, the Förster theory does not consider the influence of the AuNP on the radiative rate of the dye molecule in its vicinity. A full electrodynamic theory for the dye-AuNP interactions was developed by Ruppin [48]. He calculated the radiative and non-radiative decays of a molecule near a silver sphere. It was found that the lifetime of the molecule decreases when the molecule is closer to the particle than the wavelength of the emitted light. Chew extended the model to calculate the rates for a molecule situated inside and outside the dielectric sphere [49].

A recent publication [50] demonstrated that multipole effects are important at small distances between an emitter and a metal nanoparticle. The absorption spectrum of the dye is changed in this interaction regime. Also, quantum mechanical effects become important when the distance between the dye and AuNP is very small or the particle radius is less than 10 nm [51]. The wave nature of electrons has to be taken into account when a molecule is

almost at the surface of the particle.

Energy transfer from the dye to an AuNP was also described quantum mechanically [10, 45]. It was found that the energy transfer rate actually depends on the orientation of the dye to the AuNP surface, and becomes maximal when the dye transition dipole is perpendicular to the AuNP surface. The authors discovered that for distances comparable to the nanoparticle size the distance dependence goes as R^{-3} or R^{-4} and at long distances it approaches the typical Förster R^{-6} law. Also, a mixed approach, where the molecule is treated quantum mechanically and the AuNP classically, was used [52].

It has been demonstrated that the electrostatic Gersten-Nitzan model gives results similar to the full electrodynamic theory if the particle size and dye-AuNP distance are smaller than the penetration depth of electromagnetic field in gold [53]. In this thesis AuNPs of 10 nm and 20 nm diameters were used. The dye-AuNP distance did not exceed 25 nm. Therefore, the Gersten-Nitzan model is applicable for the systems considered in this work. Moreover, this model is computationally less expensive than the full electrodynamic theory.

2.2.4 Gersten-Nitzan model

J. Gersten and A. Nitzan developed an electrostatic theoretical model [47, 54] to describe interactions of a fluorescent molecule with a metal nanoparticle. The following depiction of the model is based on the reference [54].

The model holds for the case when the diameter of the spherical particle is much smaller than the wavelength of light. The whole system is treated electrostatically, so retardation effects are neglected. The particle has a dielectric constant $\varepsilon(\omega)$, which does not depend on the k vector of the incident wave. The dye molecule is approximated as a dipole. The system is submerged in a medium with dielectric constant ε_m. The particle has a radius a and the distance from the dye to the center of the AuNP is R.

The radiative rate can be calculated from the emitted power into the solid angle Ω by the dye with dipole moment $\mathbf{d}$

$$\frac{dP_r}{d\Omega} = \frac{\sqrt{\varepsilon_m}\omega^4 |B\mathbf{d}|^2 \sin^2\theta}{8\pi c^3}, \tag{2.11}$$

where θ is the zenith angle, the parameter B describes the change of the dipole moment in

the presence of an AuNP. B is calculated for the perpendicular and parallel orientations of the dye dipole moment to the surface of the AuNP as

$$B_{\parallel} = 1 - \frac{(\varepsilon - \varepsilon_m)a^3}{(\varepsilon + 2\varepsilon_m)R^3} \qquad (2.12)$$

$$B_{\perp} = 1 + \frac{2(\varepsilon - \varepsilon_m)a^3}{(\varepsilon + 2\varepsilon_m)R^3}. \qquad (2.13)$$

The radiative rate is obtained by spatially integrating the expression (2.11) and dividing it by the photon energy

$$\Gamma_r = \frac{\sqrt{\varepsilon_m}\omega^3|B\mathbf{d}|^2}{3\hbar c^3}. \qquad (2.14)$$

The influence of the AuNP on the non-radiative decay is described as energy dissipation in this model. The radiating molecular dipole induces a plasmon in the AuNP, which is modeled as a resistor with conductivity σ. The current flow in the particle is hindered by this finite conductivity and the power is dissipated into heating as

$$P_{nr} = \int \frac{\sigma|\mathbf{E}|^2}{2}d\mathbf{r} \qquad (2.15)$$

where $\mathbf{E}$ is the electric field of the molecular dipole.

The non-radiative rate of the molecule can be obtained by dividing the expression (2.15) by the photon energy and considering the relation between the conductivity and dielectric constant of the AuNP $\sigma = \frac{Im(\varepsilon)\omega}{4\pi}$

$$\Gamma_{nr} = \frac{Im(\varepsilon)}{8\pi\hbar} \int |\mathbf{E}|^2 d\mathbf{r}. \qquad (2.16)$$

Finally, the non-radiative decay rate for two orientations of a dye can be expressed as

$$\Gamma'_{nr,\parallel} = -\frac{|d|^2}{4\hbar a^3} \sum_{n=1}^{\infty} n(n+1)(2n+1) \left(\frac{a}{R}\right)^{2n+4} Im\left[\frac{1}{n\varepsilon + (n+1)\varepsilon_m}\right], \qquad (2.17)$$

$$\Gamma'_{nr,\perp} = -\frac{|d|^2}{2\hbar a^3} \sum_{n=1}^{\infty} (n+1)^2(2n+1) \left(\frac{a}{R}\right)^{2n+4} Im\left[\frac{1}{n\varepsilon + (n+1)\varepsilon_m}\right]. \qquad (2.18)$$

The theory gives the expressions for perpendicular and parallel orientations of the molecular transition dipole to the AuNP surface. Such ideal situations might not necessarily be

29
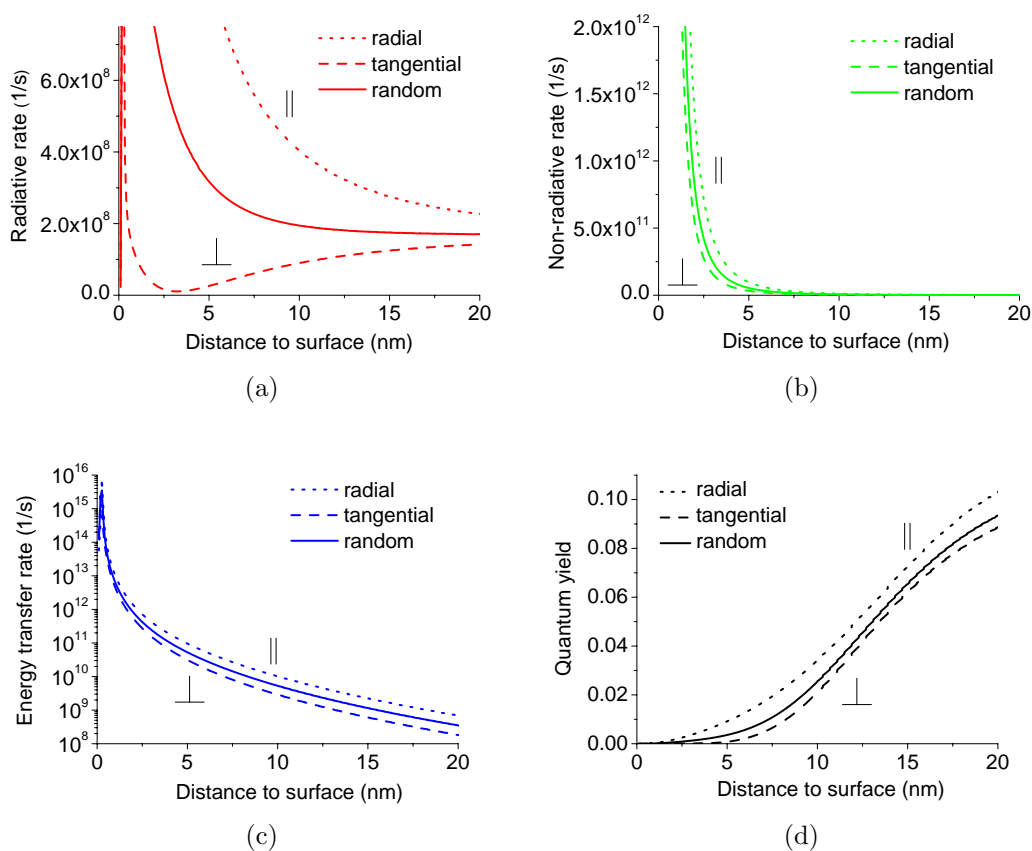
Figure 2.4: Distance dependencies of the radiative (a), non-radiative (b), energy transfer (c) rates and quantum efficiency (d) for tangential, radial and random orientations of the dye transition dipole moment to AuNP surface calculated with Gersten-Nitzan theory. Modeling is performed for a dye with 11 % quantum efficiency and 690 ps fluorescence lifetime near a 20 nm AuNP.

the case in reality. Real dyes conjugated to AuNPs through biomolecules often have no defined dipole orientation, so a random orientation to the AuNP surface would consist of 2/3 of the pure tangential and 1/3 of the pure radial contributions from the corresponding radiative and non-radiative rates and, consequently, quantum efficiencies. Figures 2.4(a), 2.4(b), 2.4(c) and 2.4(d) show the distance dependencies of the radiative, non-radiative, energy transfer rates and quantum efficiency for tangential, radial and random orientations for a dye with 11 % quantum efficiency and 690 ps fluorescence lifetime near a 20 nm AuNP. Calculations are made for the relevant distance range for the systems investigated in this work. The results show that at very short distances below 5 nm energy transfer dominates and quantum

efficiency diminishes. The calculation was performed using the software developed by E. Dulkeith and M. Ringler [55].

2.3 Antigen-antibody binding

Antigens are molecules that upon appearing in an organism result in generation of antibodies by the immune system (figure 2.5) [56]. An epitope is the binding site on the antigen, where an antibody can attach. Antigens are called haptens if they have only one epitope. Larger molecules, like proteins, may have several epitopes.

Antibodies in the human immune system are represented by several classes of proteins called immunoglobulins (Ig). These include IgA, IgD, IgE, IgG, and IgM. These classes differ in their functions, location in the body and their biological properties. Among these IgG is responsible for the majority of antibody defense, it is also the class used in this work.

IgG has a Y-shaped structure as shown in figure 2.5. It consists of two Fab regions (fragment, antigen binding) connected to the Fc fragment (fragment, constant/crystallizable). The Fab fragments have regions called paratopes on their tips which are responsible for specific antibody binding. For some purposes it is more convenient to work only with sensitive Fab fragments and not with the whole antibodies. Fab fragments can be separated from Fc in two different ways [57]. First, one can obtain two separate Fab fragments and one Fc using an enzyme called papain. Second, one can obtain Fc and two Fab fragments still connected with each other through a flexible sulfur bridge (this structure is called F(ab')2) by applying an enzyme called pepsin. F(ab')2 adsorbs on gold more readily than Fab. Therefore F(ab')2
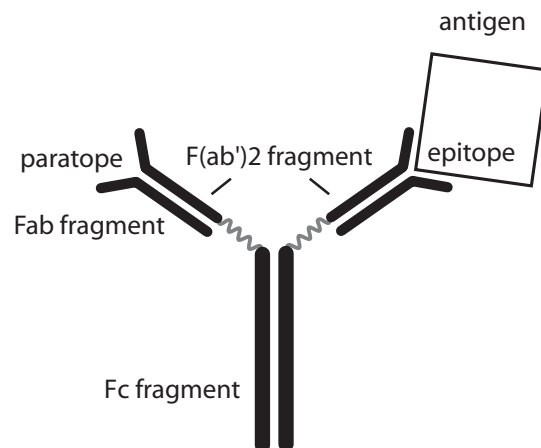
Figure 2.5: Structure of the antigen-antibody complex. An antibody consists of two Fab regions (fragment antigen binding) connected to the Fc fragment (fragment constant/crystallizable). Fab fragments have regions called paratopes on their tips which are responsible for specific antibody binding.

was used in the experiments shown in this work.

2.3.1   Biosensors and immunoassays

A device for the detection of biomolecules is called a biosensor. Immunoassays are biosensors that use antibody-antigen interaction in their detection procedure [58]. A molecule that is to be detected is called an analyte. For some immunoassays a separation step can be included, which involves washing the system to remove unbound molecules [59]. Such assays are called heterogeneous. If the separation step is omitted, the assay is called homogeneous. The latter type was used in this work because it is potentially quicker and simpler than the heterogeneous type. Homogeneous assays can be automated easier and are theoretically more sensitive than heterogeneous because no losses of the analyte happen during the separation process [60]. Homogeneous assays, however, have a disadvantage that free labels stay in the same solution with analyte-label, so that the background signal from the label reduces the whole observable effect.

The quality of an immunoassay is based on a number of validation parameters that determine its practical applicability [61]. The first parameter is the specificity of the test. It determines whether the assay detects only the analyte and does not give a false reaction to other components present in the solution, such as different proteins present in serum in the case of our system. The second parameter is the accuracy of the immunoassay. This is determined in a number of measurements comparing the analyte concentration value obtained from the novel test with established reference values. The third parameter is the linearity of the test. This means that the signal delivered by the assay should depend linearly on the analyte concentration. The fourth parameter is the precision of the test. This refers to the reproducibility of the results delivered by the test under specific conditions under variation of the location, test operator, equipment, etc. The fifth parameter is the test range, i.e. the interval of concentrations, where the test is applicable. The sixth parameter is the limit of detection (LOD), which is the smallest amount of analyte that can be distinguished from the absence of analyte. Formally LOD is defined as $LOD = \frac{3 \cdot SD}{m}$, where SD is the standard deviation of the signal from the blank and m is the slope of the analytical curve showing the dependence of the signal on the analyte concentration [61]. The seventh biosensor

characteristic is the limit of quantitation (LOQ), which is the concentration at which different amounts of analyte can be distinguished and quantified. It is defined as $LOQ = \frac{10 \cdot SD}{m}$ [61]. The eighth parameter determining the quality of an immunoassay is its robustness. This is determined by the deliberate variations of different values and parameters in the test and check of the assay result.

2.4 Excitons in semiconductor nanocrystals

Semiconductor nanocrystals are tiny crystalline materials of sizes of about 2-10 nm possessing ordered lattice structures like bulk materials. Due to their small size, the wave-functions of electrons and holes are strongly confined in a 3-dimensional quantum box. This is decisive in determining the optical properties of NCs. Quantum confinement takes place when the size of a semiconductor becomes smaller than the exciton Bohr radius of this material. Depending
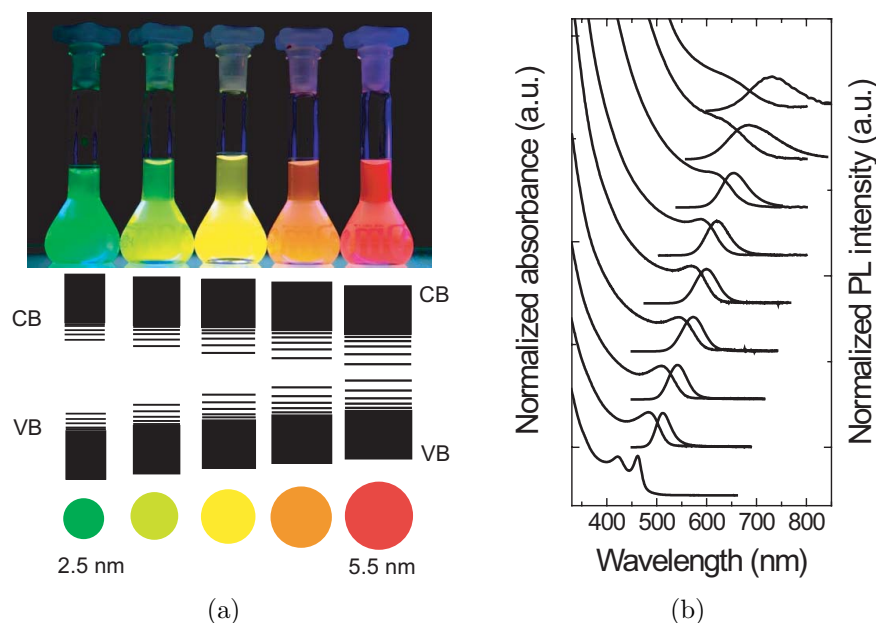
Figure 2.6: (a) Photographs of CdTe NCs of different sizes and schematic representation of the quantum confinement effect. Emission wavelength of NCs is determined by the band gap between the conduction (CB) and valence bands (VB) of the particles. Image courtesy of A.L. Rogach, with permission. (b) Absorption and PL intensities of CdTe NCs of different sizes. The smaller the particle, the further in the blue it absorbs and emits. Reprinted with permission from [62]. Copyright 2002 American Chemical Society.

on the width of 3-dimensional quantum box the band gap energies of NCs also vary, directly affecting their light absorption and emission properties. Thus, smaller NCs with a higher degree of confinement have a larger band gap and emit at shorter wavelengths than larger NCs with a lower band gap emitting at longer wavelengths (figure 2.6(a) and 2.6(b)). The mobility of electrons and holes is strongly reduced in NCs. This effect puts the properties of NCs between those of bulk semiconductors and molecules.

Generally, when the dimensionality of a materials changes, energy bands are affected and the density of states at the band edge is decreased and states become discrete [63–65]. This leads to quantization of energy levels in NCs. Figures 2.7(a)-2.7(d) show how the density of states depends on energy for materials in different dimensionalities. NCs belong to the 0-dimensional case and are therefore often called quantum dots (QDs).
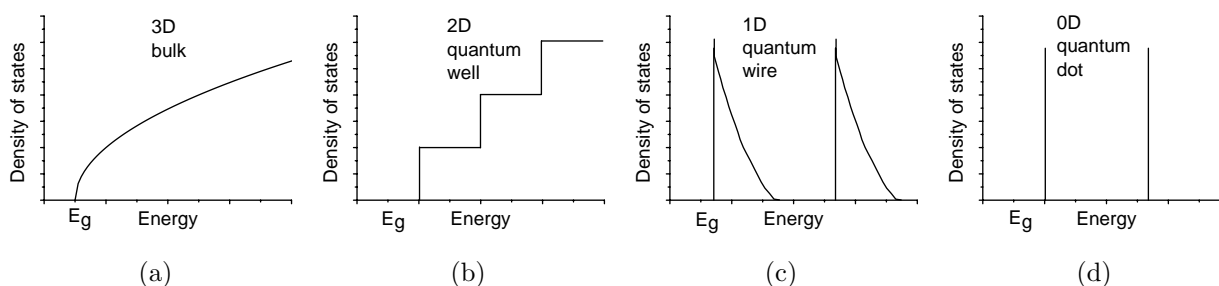
Figure 2.7: Density of states of a charge carrier confined in different dimensions. E_g is the band gap of the bulk material. Quantum dots have discrete energy levels.

Since the surface to volume ratio in NCs is much larger than in bulk materials, the surface of NCs can play a crucial role in their optical properties. Special surface treatment of NCs is applied when one is interested in emission properties of NCs. One option is the coverage of the NC with other crystalline materials creating a shell around the light-emitting core. This surface passivation strategy has been applied for CdSe NCs, where a ZnS shell was used to cover the core [66]. ZnS has a wider band gap than CdSe and contributes to the confinement of the electron and hole in CdSe core.

In order to passivate the surface of NCs and to keep them stable as colloidal solutions, organic molecules are bound to the NC surface. Common surface stabilizers are thiolates for water soluble NCs and trioctylphosphine, oleic acid and 1-octadecene molecules for NCs

soluble in organic solvents.

If there are surface defects, oxidized atoms or missing surface stabilizer molecules, these can be so called traps for the charge carriers. Wave functions of an electron or a hole can be strongly localized at such a trap, hindering the radiative recombination of an exciton. These trap states lie below the first excited exciton state and have very low oscillator strengths and do not satisfy the dipole transition selection rules [67, 68].

2.4.1 FRET between semiconductor nanocrystals

Semiconductor NCs have some differences from organic dyes, which make them interesting objects for investigations and applications of energy transfer [23]. There are several peculiar features of NCs, which influence their behavior in energy transfer processes.

Energy transfer can take place from a NC with a large band gap to a NC with the smaller band gap. However, nanocrystals have a certain distribution in their sizes (section 3.2.2). This also means a distribution in band gaps in the ensemble. Therefore, all donors and acceptors are not the same, as in the ensemble of dye molecules. Consequently, resonant energy transfer between quantum dots can happen with phonon assistance [69]. Furthermore, the estimation of the spectral overlap between donors and acceptors needs to account for the spectral inhomogeneity [70]. This fact also leads to the existence of the distribution of energy transfer rates in NC systems instead of single transfer rate in molecular systems.

Another peculiarity of NCs is their absorption spectra, which are very broad and reach the UV range (figure 2.6(b)). This implies that if both donor and acceptor are NCs, both might be excited. Therefore, energy transfer from one NC to another will display itself as an enhancement of the acceptor fluorescence in the presence of the donor.

NCs are larger than organic dye molecules and have sizes comparable with distances at which FRET takes place. Therefore NCs cannot be considered point dipoles [69].

Because of the large size of NCs, the distance between donor and acceptor-NCs is normally defined as center-to-center distance. However, the issue of the dipole moment in NCs is not finally clarified [71].

There have been a number of studies investigating whether energy transfer between NCs follows the Förster mechanism. Both theoretical [70, 72–75] and experimental [76] publi-

cations report that in most cases Förster theory is appropriate to describe NC-NC energy transfer.

3. Materials and sample preparation

3.1 Fluorescence quenching biosensors

3.1.1 Cy3 and Cy3B dyes

Two cyanine fluorophores were used in experiments of fluorescence quenching by AuNPs described in chapters 5 and 6. These were Cy3 and Cy3B dyes (figure 3.1). Both dyes were purchased from GE Health Care.

As can be seen from the chemical formulas, Cy3B has a more rigid chemical structure than Cy3. This leads to a higher quantum efficiency of 67 % in comparison with 4 % of Cy3 and a longer fluorescence lifetime of 2.9 ns compared to 300 ps of Cy3 [77, 78]. The Cy3 dye undergoes isomerisation at room temperature, which leads to the low quantum efficiency [79].
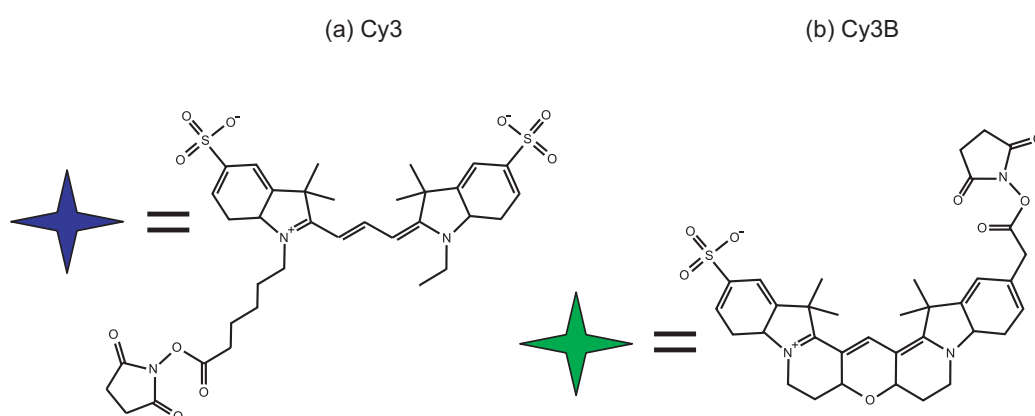
Figure 3.1: Chemical structures of Cy3 (a) and Cy3B (b) dyes. Cy3B has a more rigid backbone than Cy3. Therefore, Cy3B has a longer fluorescence lifetime and a higher quantum efficiency.

(a) (b)
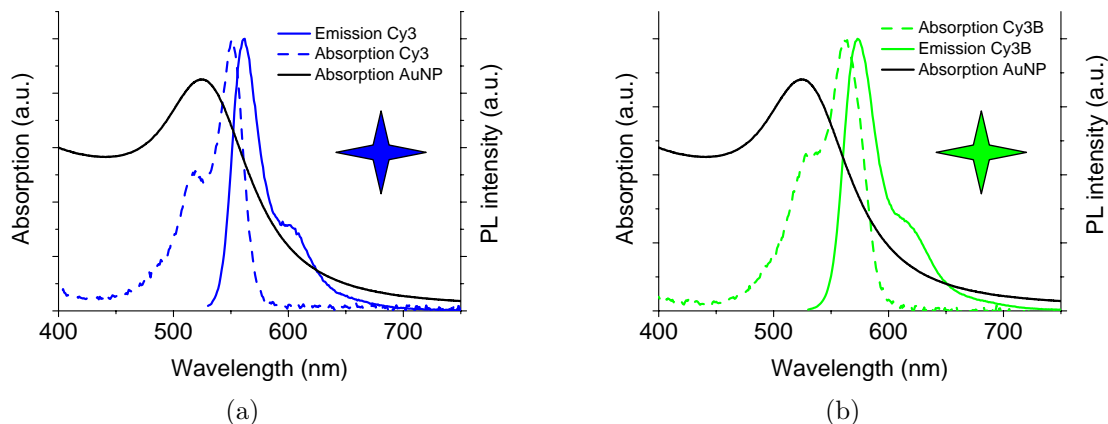
Figure 3.2: Absorption and fluorescence emission spectra of Cy3 (a), Cy3B (b) and absorption spectra of AuNPs (black curves) with diameter of 10 nm. There is a large spectral overlap between the fluorescence emission of the dyes and absorption of AuNPs, which is needed for energy transfer from the dye to the AuNP.

Table 3.1: Quantum efficiencies of Cy3- and Cy3B-conjugates.

Conjugate	quantum efficiency
BSA-Cy3-Dig	0.083 ± 0.004
Cy3-F(ab')2	0.041 ± 0.004
Cy3-IgG	0.041 ± 0.004
BSA-Cy3B-Dig	0.150 ± 0.004
Cy3B-F(ab')2	0.116 ± 0.004
Cy3B-IgG	0.116 ± 0.004

The fluorophores were chosen for a number of reasons. First, they provide a good spectral overlap of their fluorescence spectra with absorption spectra of AuNPs, which is a prerequisite for energy transfer from dye to AuNP (figures 3.2(a) and 3.2(b)). Second, the quenching range of the AuNPs is longer when the PL emission spectrum of the dye is close to the plasmon resonance [9]. Third, cyanine dyes were shown not to be strongly quenched by tryptophan amino acid, which is present in many proteins [80]. Since the topic of this investigation is fluorescence quenching by gold nanoparticles, it is not desirable to have other competing or interfering quenching processes in the system.

Quantum efficiencies of the dye conjugates used in this work were determined in comparison to the quantum efficiency of Cy3, which is equal to 0.04 according to the reference [77]. All obtained values are listed in table 3.1.

3.1.2 Bovine serum albumin

Bovine serum albumin (BSA) is a protein present in the blood serum of cows. For this work BSA was a component of the buffer, in which all the reactions took place and a carrier protein to which digoxigenin and dye molecules were attached. BSA was obtained from Roche Diagnostics.

According to Ferrer et al. [81], BSA in aqueous solution has 8.4×3.2 nm dimensions. The structure of the protein is shown in figure 3.3.

Figure 3.3: Structure of BSA. Lysine amino acids, where Dig and dye are connected are marked as ball and stick. Lysines in the core of the protein are marked in red, if they lie on the boundary, then green and lysines on the surface are marked blue. Only lysines on the surface were available for Dig and dye conjugation. Out of 30 available lysines 2 were occupied by dye molecules and 8 by the Dig molecules. Image produced from the Protein data bank [82], courtesy of M. Wunderlich, with permission.
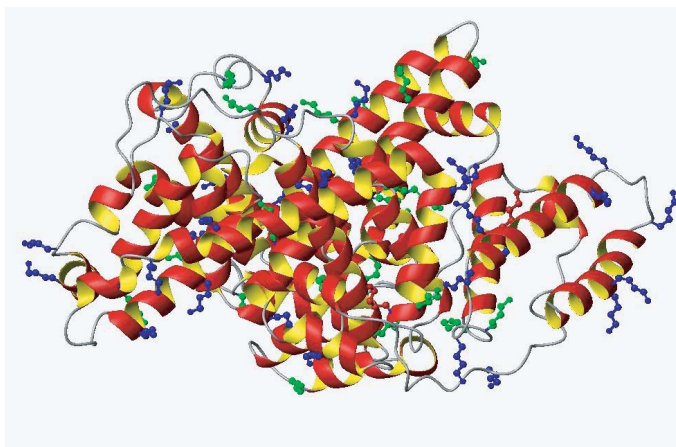
BSA buffer. A general problem in working with proteins is their tendency to adsorb on surfaces (cuvette walls, pipette tips, etc.) [83]. Measurements were performed in a buffer containing a high BSA concentration of 1 mg/ml in order to solve this problem. BSA passivates all surfaces to a maximally possible degree preventing analyte proteins from being lost at the surfaces. Additionally, pipette tips were previously washed with BSA buffer. Since conformations of proteins are pH sensitive, the pH value was kept constant by a tris(hydroxymethyl)aminomethane buffer (Trizma pH 7.5, Sigma) at a concentration of 20 mM.
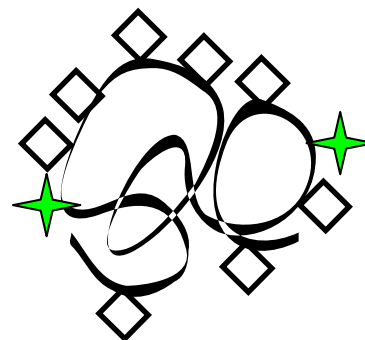
Figure 3.4: One BSA carrier protein hosts two fluorophores and eight digoxigenin molecules.

BSA-digoxigenin-dye conjugation. BSA is readily available and commonly used as a carrier in FRET immunoassays [84]. Conjugation of Dig and dye molecules to BSA was performed through lysine residues (figure 3.3). There are about 30 lysine amino acids on the

outer surface of BSA [85]. Each lysine has a free amino group that can bind to the activated carboxyl ester group, i.e. N-hydroxysuccinimide esters of digoxigenin, Cy3 and Cy3B to form stable amid bonds. Because of the high number of available lysines different degrees of labeling of BSA by Dig or dye are possible. In the experiments presented in this work, one BSA carrier protein hosted two fluorophores and eight digoxigenin molecules (figure 3.4). The conjugation was performed by M. Wunderlich.

3.1.3   Conjugation of dyes with antibodies

F(ab')2 fragments of monoclonal anti-TnT antibodies were dissolved in a phosphate buffered saline (PBS) solution. The concentration of antibodies was determined from their optical density at 280 nm using the formula $c[mg/ml] = OD_{280}/1.4$ [85]. The optical density at 280 nm had to be corrected for the absorption of dyes as $OD_{280}^{corr} = OD_{280} - 0.08 \cdot OD(\lambda_{max})$ [78], where the wavelength of maximal absorption λ_{max} was 550 nm for Cy3 and 561 nm for Cy3B. The typical molecular mass of an antibody is 150 kDa = 2.49 $\cdot 10^{-22}$ kg. A desired amount of fluorophore is added. The reaction solution was slowly shaken under protection from light. The reaction was stopped by the addition of lysine. In the final result the dye molecule was bound to lysine through the peptide bond. The conjugation of Cy3 and Cy3B dyes to antibodies used in all experiments of this work was performed by M. Wunderlich.

In the experiments presented in this thesis there were 5.4 ± 0.3 Cy3 dye molecules per antibody and 2.4 ± 0.2 Cy3B molecules per antibody. These values were determined from absorption measurements at the dye absorption peaks and at the antibody absorption at 280 nm.

3.1.4   Digoxigenin and digoxin

Digoxigenin (Dig) and digoxin (figure 3.5) are examples of haptens, i.e. molecules with only one binding site for an antibody. Dig was used as a model analyte in this work. Both of the substances can bind to the anti-Dig antibody with high affinity constants of $5.1 \cdot 10^{10}$ 1/M [85]. The association constant is $1.8 \cdot 10^6$ 1/Ms and the dissociation constant is $3.5 \cdot 10^{-5}$ 1/s [85]. Since digoxigenin can be bioconjugated easier than digoxin, it was used in the experiments.
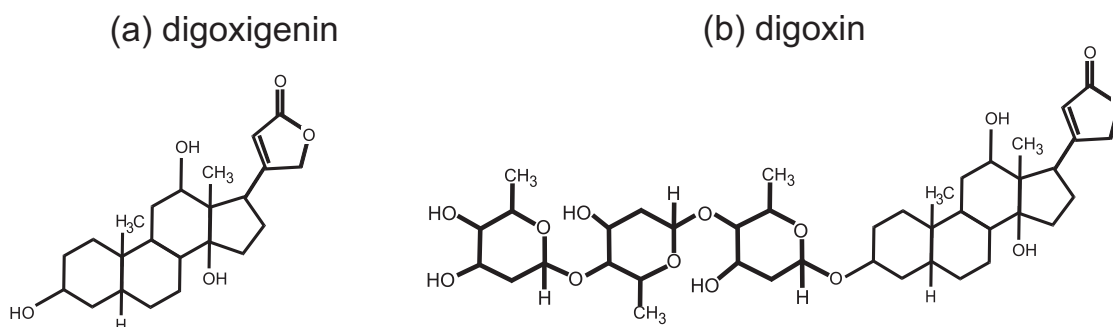
Figure 3.5: Chemical structures of digoxigenin (a) and digoxin (b). Anti-Dig antibody is sensitive to both molecules.

Digoxin is medically relevant since it is used to cure cardiac arrhythmia and heart failure [86]. Digoxin is toxic in high concentrations, so it is critical to be able to detect it in the therapeutic concentration range of 1 to 6 ng/mL [87]. The molecular mass of digoxigenin is 390.5 g/mol, which is two times smaller than the one of digoxin amounting to 780.9 g/mol. Therefore, for Dig the relevant detection concentration range is 0.5 to 3 ng/mL.

Digoxigenin is modified with succinimide (digoxigenin-3-O-methylcarbonyl-ε-aminocapron-acid-N-hydroxysuccinimidester) in order to enable amid bonding to BSA. Labeling of Dig was performed by M. Wunderlich. All Dig samples were obtained from Roche Diagnostics.

3.1.5 Cardiac troponin T

Cardiac troponin T (TnT) is a protein from the human heart muscle. This protein is released into the blood in case of myocardial infarction and is a marker of this disease. It is important to be able to detect low concentrations of this protein in blood in order to treat a patient on time.

The molecular mass of TnT is 37 kDa = $6.1 \cdot 10^{-23}$ kg [88]. TnT is known to have two specific binding sites (epitopes) at different positions on the surface of the molecule. Two antibodies can bind to both epitopes simultaneously thus enabling the possibility of a sandwich-type immunoassay.

The TnT used in the experiments was obtained from Roche Diagnostics. It was delivered originally in the lyophilized (freeze-dried) form together with other serum components. The

sample was then dissolved in 2.5 mL of distilled water to a concentration of 100 nM. This stock solution was accordingly diluted for further experiments. For dilution either BSA buffer or human serum was used. Human serum was provided by Roche Diagnostics.

The experiments shown in figure 6.13 were performed using standardized samples from Roche Diagnostics with known TnT concentrations. These samples were obtained in frozen form, so they had to stay at room temperature for about an hour before the measurements.

3.1.6 Functionalization of gold nanoparticles with antibodies

AuNP of 10 nm diameter (BBInternational) were used for the Dig immunoassays (chapter 5). AuNPs were functionalized with complete monoclonal anti-Dig antibodies.

20 nm AuNPs (Roche Diagnostics) were used for the TnT systems (chapter 6). For the experiments described below two sets of particles were prepared. In the first set AuNPs were functionalized with complete intact monoclonal anti-TnT. In the second set AuNPs were covered with anti-TnT F(ab')2 fragments.

Proteins are adsorbed to the surface of gold through electrostatic and van der Waals interactions. The remaining free sites on the gold surface are passivated with BSA so that the entire surface of the AuNPs is covered. The functionalization of AuNPs used in all experiments of this work was performed by M. Wunderlich according to a method described in [89].

It is important to mention that the antibodies take random positions on the gold surface since functionalization by antibodies is performed by adsorption. Therefore, it is expected that some of the epitopes are not accessible for the analytes. It was estimated that there were about 20 binding sites on 10 nm AuNPs and about 40 on 20 nm AuNPs [85]. Another important aspect arising from this is that the dye was oriented randomly to the surface of the AuNP and also the separation distance of the fluorophore and AuNP is not exactly known. Realistically speaking, there is a distribution of separation of distances between the dye and the AuNP.

3.2 Clusters of CdTe nanocrystals

3.2.1 Synthesis of CdTe nanocrystals

The CdTe particles used in this work were synthesized by A. Susha using the method described in [62, 90]. Thiolate stabilizers are added to $Cd(ClO_4)_2$. The thiol ligands make the growth process slower and allow control over the size of the resulting NCs. The pH is especially adjusted for every thiol stabilizer by adding NaOH. The whole reaction takes place in two stages. First, H_2Te gas produced in the reaction of solid Al_2Te_3 with sulfuric acid H_2SO_4 is passed through the solution containing $Cd(ClO_4)_2$ and stabilizer molecules. The reaction runs without oxygen in a nitrogen atmosphere. At this stage precursors of CdTe are formed. Second, the solution is boiled and CdTe NCs grow. The synthesis can last between one hour and seven days depending on the desired diameter of the NCs. The size of the resulting NCs can be controlled by the reaction time at this stage.

NCs with different thiol surface stabilizers were used in this work (figure 3.6). The synthesis processes for all stabilizers are analogous except the different reaction pH for cysteamine. CdTe NCs with disodium 1,4 - phenylene-bis (dithiocarbamate) (abbreviated as PBDT) surfactant were synthesized with a 9:1 ratio of TGA to PBDT during the synthesis following the method described above.

Red and green NCs described in chapter 7 were capped with thioglycolic acid (TGA) and near-infrared emitting NCs were capped with mercaptopropionic acid (MPA) (figure

disodium 1,4 – phenylene-bis   thioglycolic acid   mercaptopropionic   cysteamine
(dithiocarbamate)   acid
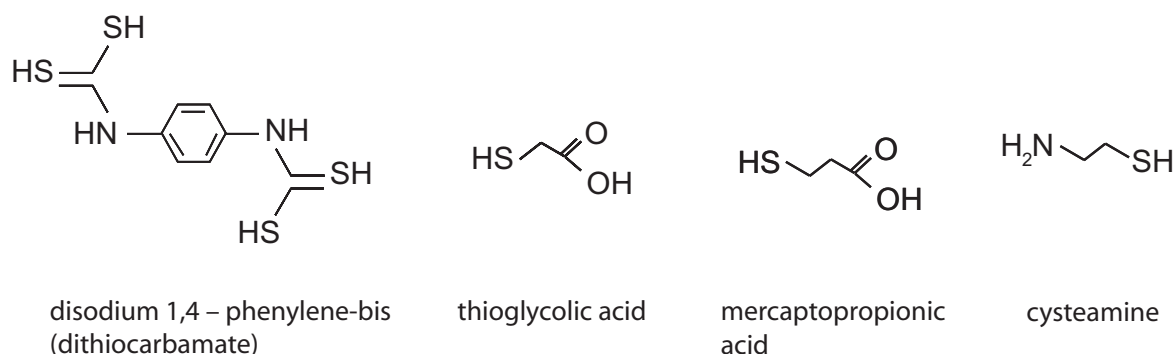
Figure 3.6: Chemical structures of the surface stabilizers for CdTe NCs. Thiol groups (-SH) are connected to the NC surface.

3.6). The thiol group (-SH) connects to the NC surface and -COO$^-$ groups provide negative charge on the outer surface of the NC. The surface of each green NC was covered with approximately 250 TGA molecules, every red NC had about 350 TGA molecules on the surface. The diameter of the NCs can be estimated from the position of the first absorption peak [90]. Thus green NCs were estimated to be 2.5 nm, red NCs 3.5 nm and near infrared NCs 6.5 nm in diameter. The concentration of CdTe NCs in solution can be estimated from the optical density of the solution at the first absorption peak [91].

3.2.2 Size selective precipitation

Freshly synthesized CdTe NCs are of different sizes in the resulting solution. Therefore, in order to obtain NCs with as narrow a size distribution as possible, size-selective precipitation is applied [92, 93]. The process is based on the fact that largest particles precipitate first when non-solvent (2-propanol) is added to the solution. After centrifugation the largest particles stay on the bottom of the test tube, while smaller ones are still in the supernatant. The

(a)   (b)
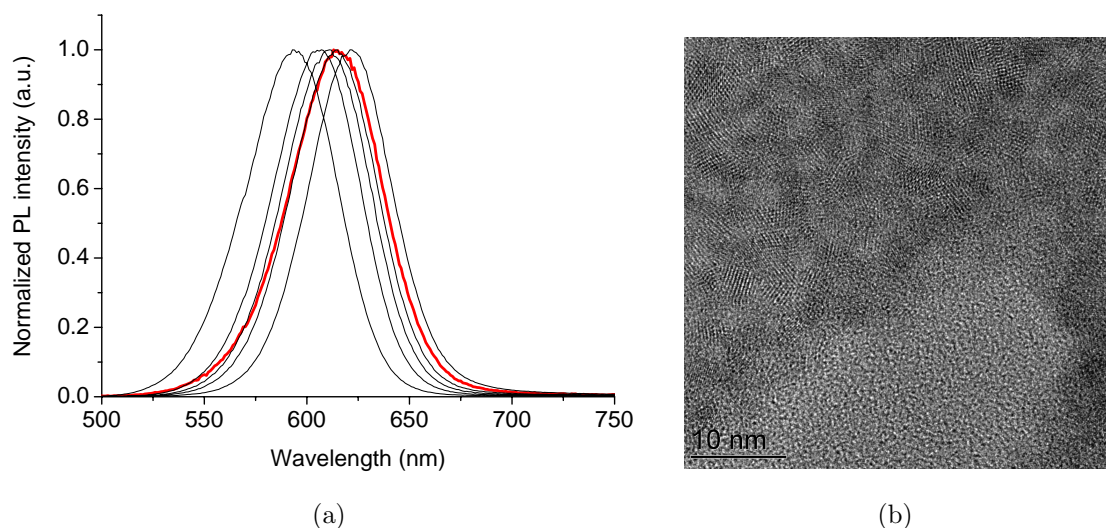
Figure 3.7: (a) PL of the as prepared CdTe NCs (red) and fractions separated by size-selective precipitation (black). After the separation, NCs with different sizes and optical properties are obtained. Image courtesy of A. Susha, with permission. (b) High resolution TEM image of CdTe NCs. The size distribution of NCs in an ensemble is 10-15 %. Image courtesy of M. Döblinger, with permission.

process can be repeated several times to obtain 5-10 fractions containing NCs of different sizes from the same synthesis.

The individual fractions of NCs have emission maxima around a certain wavelength. Due to the nature of the size-selective precipitation, NCs within one fraction still do not have exactly the same diameter resulting in an inhomogeneous distribution of sizes within one fraction. The size distribution of NCs in an ensemble is typically 10-15 % [94]. Consequently, the emission wavelengths of individual NCs in this ensemble also differ spectrally from each other according to the sizes of the particles (figure 3.7(a)). In the high resolution TEM images NCs within one fraction appear to be monodisperse within 10-15% size distribution (figure 3.7(b)).

3.2.3 Cluster preparation with Ca^{2+} ions

In order to prepare clusters, aliquots of 0.01 M $CaCl_2$ (anhydrous, > 90%, Merck) were added to CdTe NCs diluted in 3 mL of deionized water (produced by a Millipore Milli-Q Gradient A-10). The following equilibration happened within 10 min under occasional shaking. After this, measurements were performed. Next, more $CaCl_2$ solution was added and waiting time was again 10 min with occasional shaking. The concentration of $CaCl_2$ (effectively of Ca^{2+} ions) was chosen in a way to have a 100-5000-fold greater concentration of Ca^{2+} ions in comparison to CdTe NCs. Five solutions with different Ca^{2+} ion concentrations were prepared.

The optical density was lower than 0.1 in order to avoid the inner filter effect. Measurements aimed to demonstrate the influence of Ca^{2+} on purely green and red NC (figure 7.2(a) and 7.2(b)) were performed with 185 pmol of green and 110 pmol of red NCs.

The investigations, where energy transfer with varied donor-acceptor ratios was studied (section 7.1.3), were performed with 110 pmol of red NCs and three different amounts of green NCs: 185 pmol, 370 pmol and 740 pmol. This corresponded to 1.7:1, 3.4:1 and 6.8:1 donor-acceptor ratios.

When the mixture of NCs of three different sizes was prepared (section 7.1.4) 370 pmol of green, 185 pmol of red and 27 pmol of near infrared NCs were mixed in 3 mL of water.

3.2.4 Partial removal of surface stabilizer molecules from CdTe NCs

In the experiments where DNA was connected to CdTe NCs and where they were connected covalently through PBDT and DNA (sections 7.2 and 7.3), a washing procedure was applied to partially remove the surface stabilizer from the surface. This was done to create patches of free CdTe material on the surface, where thiol groups could bind. 400 μL of the originally synthesized highly concentrated aqueous NC solutions were diluted by the double volume of methanol (99.8 %, Aldrich). The solution was left to stand until the fluid became turbid. Subsequently, the solution was centrifuged (miniSpin plus, Eppendorf) for 5 min at 5000 rotations per minute. NCs precipitated on the bottom of the test tube after centrifugation. The transparent colorless solution was removed from the test tube leaving only the sediment. Finally, 400 μL of water were added to the sediment. If the solution did not become turbid after the addition of methanol, the amount of methanol was increased.

3.2.5 Conjugation of CdTe NCs through PBDT

PBDT-stabilized NCs (acceptors) were first pushed through 0.2 μm filters in order to remove possible large aggregates. Donor NCs were stabilized with TGA, which was partially removed from the surface as described in section 3.2.4. Donor and acceptor NCs were mixed in a 10:1 ratio in aqueous solution. Measurements were performed within 2 h after mixing.

3.2.6 Conjugation of DNA to CdTe

DNA is a biological polymer composed of units called nucleotides (figure 3.8). There are four nucleotides: guanine, cytosine, adenine and thymine. These are connected to each other by a phosphate deoxyribose backbone. Pairs of nucleotides are complimentary with each other: guanine with cytosine and adenine with thymine. DNA is a double helix, with a major and a minor groove. The ends of a DNA strand have 3' and 5' notations, where 3' denotes the end with a terminal hydroxyl group and 5' refers to the end with a terminal phosphate group.

Short DNA strands were chosen as linkers of NCs (section 7.3). Two complementary sequences consisting only of adenine (A) and thymine (T) bases were used: *AAA AAA AAA*

Figure 3.8: Chemical structure of DNA. It consists of four nucleotides connected to each other by the phosphate deoxyrhybose backbone. Pairs of nucleotides are complimentary with each other: guanine with cytosine and adenine with thymine. The image is taken from [96].
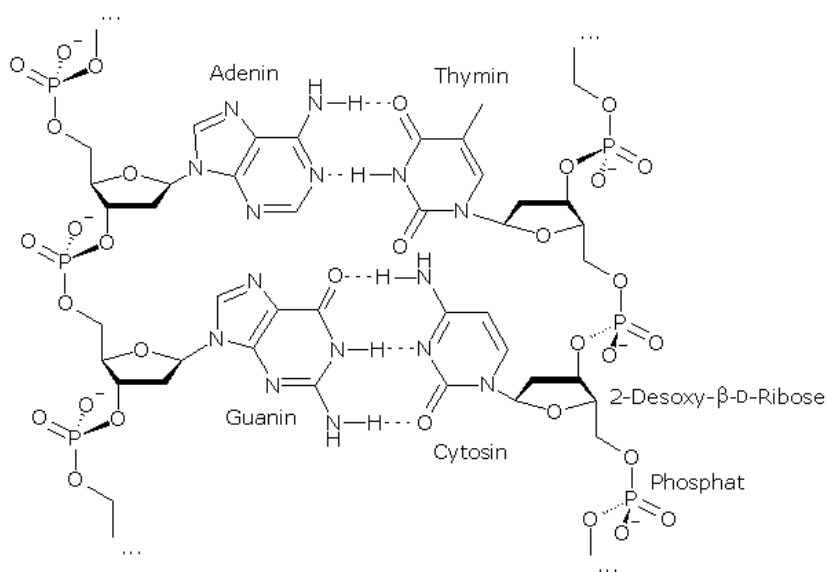
(denoted as sequence 1) and *TTT TTT TTT* (denoted as sequence 2). DNA was purchased from Metabion International AG. Both oligonucleotides were functionalized with a thiol group at the 3' end. These short DNA strands were intended to provide a sufficiently small distance between the donor and acceptor NCs so that energy transfer could take place. The sequence was chosen so that it remained stable at room temperature and the DNA did not disassemble into single strands. Moreover, DNA sequences containing thymine were shown to have little non-specific adsorption to NCs [95].

The thiolated DNA contained a CH_3-S-S- protection group on the 3' end. It was removed with the help of dithiotreitol [97]. The purchased DNA, which came in lyophilized form, was dissolved in water to a concentration of 200 μM. 200 μL of the 100 mM dithiotreitol solution in 17 mM sodium phosphate (pH 8) were added to 500 μL of the DNA solution. Then the mixture was shaken for 30 min. Finally the solution was purified. For this it was flushed through a PolyPak cartridge (Glen Research) as specified by the manufacturer. In the end, DNA was diluted in 1 mL of the 20 % acetonitrile aqueous solution. After this DNA was added to the 1 nmol solution of washed NCs in the DNA-NC ratio of 5:1. The reaction took place for about 16 hours at 4 °C. The measurements shown in figure 7.16(a) and 7.16(b) were performed in an aqueous solution with pH 6 and 300 mM NaCl required for DNA hybridization.

3.3 CdSe/ZnS/CdSe/ZnS nanocrystals

3.3.1 Synthesis of multi-shell nanocrystals

The synthesis method for CdSe/ZnS onion-like NCs was first introduced by Battaglia et al. [28]. Particles used in this work were prepared by S. Sapra using the procedure described in [98]. First, CdSe cores were synthesized. CdO was dissolved in oleic acid and 1-octadecene and heated in an argon atmosphere. Another solution containing Se in 1-octadecene was injected into the first solution with Cd. In order to create a ZnS shell around the core, ZnO dissolved in oleic acid and 1-octadecene, was added and heated. S solved in 1-octadecene was injected. The same solution as the one used to produce cores was employed to grow the CdSe shell. Finally, particles were precipitated with acetone. The resulting NCs were passivated by oleic acid/1-octadecene molecules and solved in hexane.

3.3.2 Structural and optical properties of multi-shell nanocrystals

Core-shell NCs were initially developed to increase the quantum efficiency of CdSe NCs [66]. The presence of the ZnS shell around the CdSe core improves the surface properties of CdSe.

The optical properties of these NCs give an indication that through the variation of the shell thickness one can obtain emission from the CdSe shell at a different wavelength. Absorption and emission spectra of multi-shell NCs with ZnS shell thicknesses of four (c4s2s) and six (c6s2s) atomic layers are shown in figure 3.9(a) and 3.9(b). In all cases the shells are grown around identical cores. The CdSe shell consists of two atomic layers in all samples. One can notice a clear correlation between the absorption and emission peaks. This is similar to data reported in [28].

High resolution TEM investigations of the multi-shell NCs used in this work were performed by a collaborator, Y.M. Lam, in order to clarify the material distribution in these structures. In the resulting images (figure 3.10) one can see that NCs maintain spherical shapes, but separate shells cannot be distinguished. However, when interplanar spacing in the core region is evaluated, a value of 0.22 nm can be found. This corresponds to the (110) plane in wurzite CdSe. In the surrounding of the core, where a shell is expected, the inter-
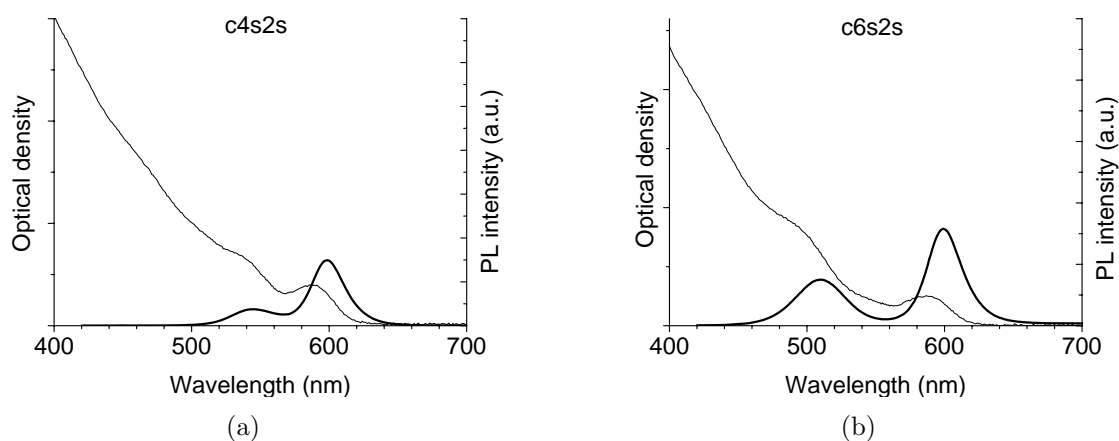
Figure 3.9: Absorption and emission spectra of multi-shell NCs with different ZnS shell thicknesses. In all cases the shells are grown around identical cores. CdSe shell consists of two atomic layers in all samples. The ZnS shell has a thickness of four (a) and six (b) atomic layers. When the ZnS shell between the CdSe core and CdSe shell in thicker, the emission of the CdSe shell is shifted to the blue. The wavelength of the core emission stays the same.
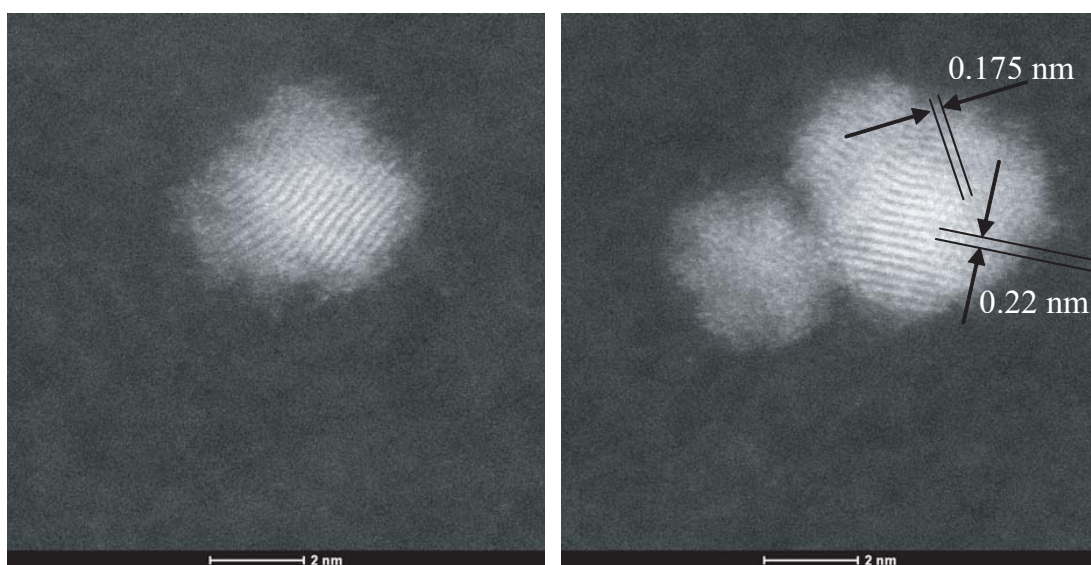
Figure 3.10: High resolution TEM images of onion-like NCs. The interplanar spacing in the core is close to 110 plane of wurtzite CdSe, in the shell the interplanar spacing corresponds to the (103) plane in wurtzite ZnS. Magnification is 10^7 times. Image courtesy of C. Boothroyd, with permission.

planar spacing is about 0.175 nm. This is in good agreement with the (103) plane in wurzite ZnS. Therefore, a conclusion can be made that both materials are present in one NC.

Another experiment performed by Y.M. Lam used small angle X-ray scattering (SAXS) to
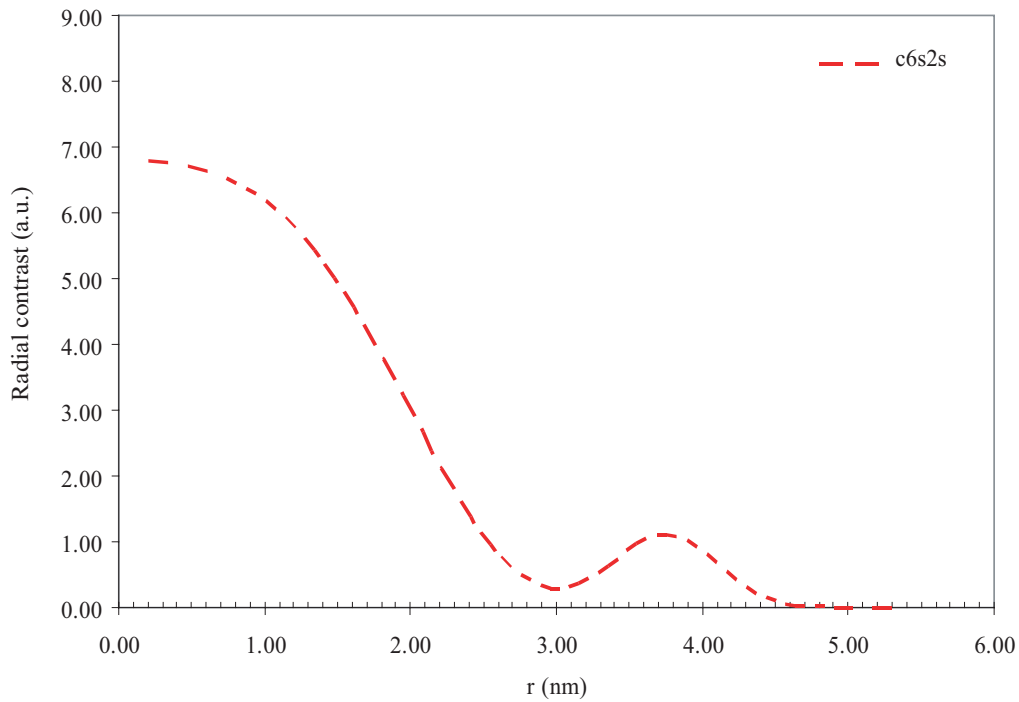
Figure 3.11: Radial contrast profile of onion-like NCs obtained from a SAXS measurement. The curve shows the distribution of CdSe in the NC with 6 monolayers of ZnS and 2 atomic layers of CdSe in the outmost shell. The material distribution shows the core-shell-like distribution of material inside the crystal. Image courtesy of Y.M. Lam, with permission.

study the material distribution inside these NCs. A radial contrast profile of onion-like NCs obtained from a SAXS measurement is shown in figure 3.11. The curve shows the distribution of CdSe in the NC with 6 monolayers of ZnS and 2 atomic layers of CdSe in the outmost shell. The material distribution shows the core-shell-like distribution of material inside the crystal.

4. Experimental methods

4.1 Steady state absorption spectroscopy

A Cary 50 (Varian) UV-Vis spectrophotometer was used in order to study the absorption[1] of samples and to measure their concentrations. A flash Xenon lamp is used as an excitation source. A wavelength is then chosen by the monochromator and the transmitted light is measured by a photomultiplier tube (PMT). The measurements are performed and compared with a blank sample containing only solvent. This allows calibration of the measurement and the removal of the effects from the solvent in the spectra and from the reflections of light from the cuvette walls.

According to the Beer-Lambert Law, the intensity transmitted through the sample at wavelength λ is

$$I(\lambda) = I_0(\lambda)e^{-\sigma(\lambda)nd}, \tag{4.1}$$

where $I_0(\lambda)$ is the incident light intensity on the sample, σ is the extinction cross section, n is the particle density and d is the sample thickness. The extinction cross section consists of scattering and absorption contributions $\sigma(\lambda) = \sigma_{abs}(\lambda) + \sigma_{scat}(\lambda)$. In experiments performed in this work the optical density (OD) was measured:

$$OD(\lambda) = \log_{10}\frac{I(\lambda)}{I_0(\lambda)}. \tag{4.2}$$

When the extinction coefficient $\varepsilon(\lambda) = \frac{\sigma(\lambda)N_A}{\ln 10}$ of the sample and its thickness d are known, an

---

[1]The correct term for these measurements is the extinction, which is composed of absorption and scattering contributions. However, since the term *absorption* has become established and common, it will be used in the rest of the work.

OD measurement allows the determination of the sample concentration c from the relation

$$OD(\lambda) = -\frac{\sigma(\lambda)cN_Ad}{\ln 10} = \varepsilon(\lambda)cd, \tag{4.3}$$

where N_A is the Avogadro number.

4.2 Steady state photoluminescence spectroscopy

In a fluorescence spectrophotometer the signal is collected at an angle of 90° with respect to the excitation beam. Since fluorescence is emitted in all directions this allows the exclusion of the excitation light from the detection.

Two devices were used: a Cary Eclipse (Varian) for strongly luminescent samples and a Fluorolog 3-22iHR (HORIBA Jobin-Yvon) for weakly luminescent samples. Both devices allow photoluminescence (PL) and photoluminescence excitation (PLE) measurements to be performed. For PL measurements the excitation is performed at a fixed wavelength and the detected emission wavelength is varied. For PLE measurements the excitation wavelength is varied and the emission wavelength is fixed.

It is important to perform the PL measurements in diluted solutions (OD < 0.05) so that reabsorption of light in the solution (called the inner filter effect) is avoided.

Cary Eclipse. The light source is a Xenon flash lamp with an excitation wavelength range of 190-1100 nm. The monochromator allows the wavelength from the spectrum of the lamp to be chosen. In the detection light path another monochromator allows fluorescence to be detected at specific wavelengths.

Fluorolog. A more sensitive fluorescence spectrometer was used to measure the fluorescence intensity in samples with troponin T (chapter 6). The sensitivity is provided by a R928P photomultiplier. Double excitation and emission monochromators provide better spectral resolution and increase the signal to noise ratio by background suppression. A 450 W Xenon lamp serves as the excitation source (250-1700 nm) followed by a double monochromator which limits the excitation wavelength range to 250-1000 nm. In the detection light path a second double monochromator selects the detection wavelength. The PMT needs to be cooled to 9° C during operation and can detect wavelengths between 250 and 850 nm.

4.3 Time resolved photoluminescence spectroscopy

4.3.1 Laser excitation

For the experiments in chapters 5 and 6 an excitation wavelength of 565 nm was used, which was provided by an optical parametrical oscillator pumped by a Ti:sapphire (Ti:Sa) laser. In order to provide correct polarization weighting, experiments were performed in the magic angle configuration [30], i.e. exciting with linearly polarized light and placing a polarizer in the detection path with an angle of 54.7° to the polarization plane of the laser. This was done in order to compensate for the polarization dependent light transmission of the monochromator. Under the magic angle condition the bias of a certain polarization is avoided and fluorescence with different polarization is detected equally.

Ti:sapphire laser. A Ti:Sa oscillator (Mira 900-F, Coherent) is pumped by a solid-state neodymium-doped yttrium aluminium garnet (Nd:YAG) laser (Verdi, Coherent) with a 532 nm wavelength and a continuous-wave power of 10 W. The Ti:Sa laser is tunable in the wavelength range from 750 to 1000 nm. The principle of operation of the Mira laser is based on Kerr lens mode locking, in which the intensity-dependent change of the refractive index of the gain material is used. The beam traveling in the laser cavity has a Gaussian profile. This beam is transmitted through an adjustable aperture, which only transmits the central part of the beam. By adjusting the aperture diameter, the leading and trailing edges are blocked and pulses of about 120 fs duration can be produced. A short change in the resonator length is induced in the beginning in order to mode lock the laser [99]. The repetition rate of the laser was 75.6 MHz.

Optical parametrical oscillator. Wavelengths in the visible range can be produced by an optical parametric oscillator with intracavity frequency doubling (OPO Advanced ring, Angewandte Physik & Elektronik GmbH). When pumped by the Ti:Sa laser it can deliver wavelengths in the 520 - 675 nm range. The pump laser frequency is split into two (called signal and idler) through a nonlinear process. The signal part of the light pulse is further doubled in another nonlinear crystal. Wavelength tuning is based on the change of the pump wavelength, temperature of the phase-matching crystal and the adjustment of the cavity length [100, 101]. Additional stabilization is needed since at the chosen wavelength both

Mira and OPO produced significant fluctuations in intensity. This was performed with the help of a circular variable metallic neutral density filter. The filter was fixed on a step motor with a feedback loop connected to a photodiode constantly monitoring the laser power. When the laser power deviated from the desired value, the filter rotated correcting for the intensity fluctuations.

Amplifier. In the experiments described in chapter 7, samples were excited at 400 nm. The excitation source was a 800 nm Ti:Sa regenerative amplifier (RegA 9050, Coherent) frequency doubled in an optical parametrical amplifier 9450 (Coherent) with a 100 kHz repetition rate and a pulse width of about 70 fs.

4.3.2 Streak camera

A streak camera (Hamamatsu) was used in order to perform fluorescence lifetime measurements. It can be operated with two different plug-ins allowing the measurement of fluorescence lifetimes in long and short time ranges. Fluorescence is measured in a 90° configuration
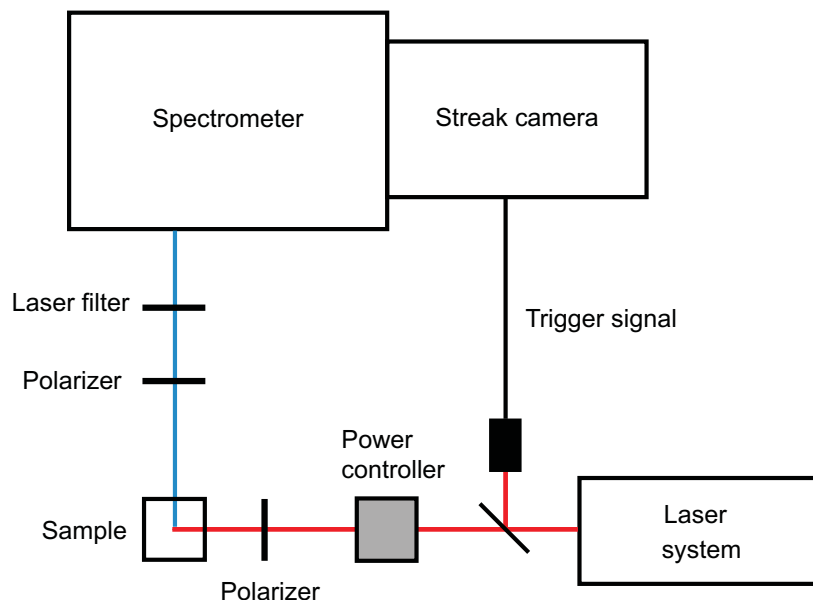
Figure 4.1: Schematic of the streak camera setup. For the experiments in chapters 5 and 6 a laser system composed of Ti:Sa laser and OPO was used, for the measurements described in chapter 7 an amplifier was used as an excitation source.

(figure 4.1). Photons first pass through the spectrometer (Chromex) and enter the streak camera spectrally dispersed.

Synchroscan plug-in (M5675 unit) was used for all time resolved measurements in chapters 5 and 6. Photons from the spectrometer are focused on the photocathode and produce photoelectrons (figure 4.2). These electrons are accelerated on an electrode. Next, they are deflected in a periodical electric field triggered by the excitation laser. In this way electrons are spatially diverted according to their arrival time creating a steak picture of the decay dynamics. Finally, the electrons are multiplied by a microchannel plate, they hit a phosphor screen producing photons which make an image on a CCD camera. A streak camera combined with a spectrometer provides simultaneously spectral and temporal information of the luminescence. The Synchroscan plug-in allows measurement of decays with lifetimes not longer than 2 ns with a time resolution of 2 ps. Measurements were performed in the photon counting mode.

Single sweep plug-in (M5677 unit) was used for the measurements described in chapter 7. This unit allows measurement of fluorescence decays in different time ranges from 5 ns to 10 ms. The highest possible time resolution is 50 ps in the fastest time range.
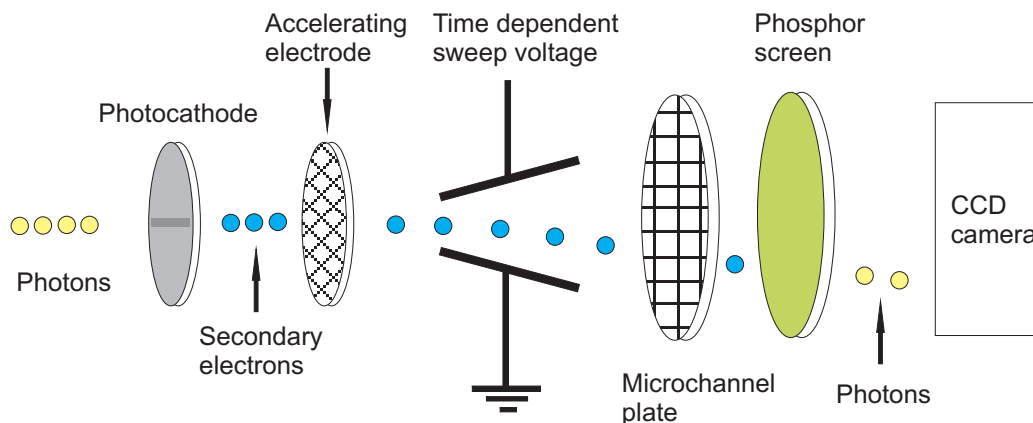
Figure 4.2: Schematic of a streak camera. Adapted from [102].
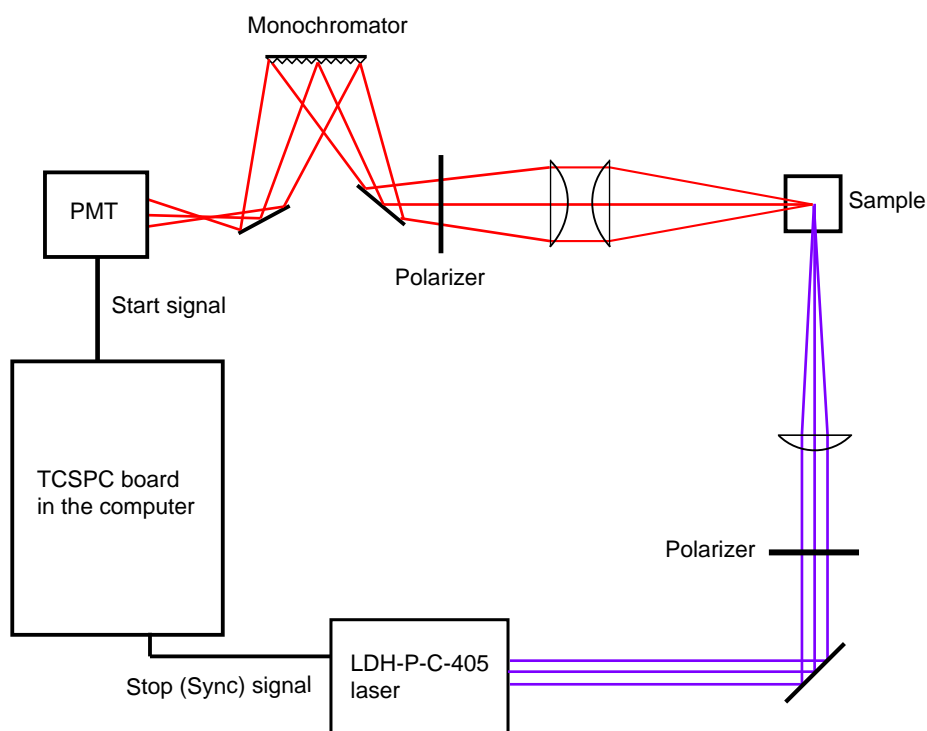
Figure 4.3: Schematic of the FluoTime 200 setup.

4.3.3 Time correlated single photon counting

A commercial fluorescence lifetime spectrometer FluoTime 200 (PicoQuant) was used for the experiments described in chapter 8 and section 7.2. The setup is shown schematically in figure 4.3. A pulsed LDH-P-C-405 diode laser with 400 nm wavelength and the repetition rate of 250 kHz was used. The instrument response function was less than 300 ps.

This device uses a technique called Time-Correlated Single Photon Counting (TCSPC). The time that has passed between the last laser pulse and detection of the photon is measured with the help of the electronics. This information is then plotted as a histogram displaying the number of registered photons depending on their detection time.

The intensity of the pulsed laser needs to be such, that the detection count rate is less than 1% of the laser repetition rate to avoid the pile-up of photons. The repetition rate of the laser has to be chosen so, that the time between the pulses is longer than the fluorescence lifetime of the molecule.

4.4 Further devices used in this work

A Zetasizer Nano ZS (Malvern instruments) is a device based on dynamic light scattering that was used to measure the sizes of aggregates of CdTe NCs in chapter 7.

A transmission electron microscope (TEM) JEOL JEM 1011 was used to obtain the images of multi-shell NCs described in chapter 8.

High resolution TEM was performed with a FEI aberration corrected and monochromated Titan TEM microscope fitted with a FEG filament and an acceleration voltage of 300 kV. This device was used to characterize CdTe and multi-shell NCs (chapter 3).

A SAXSess camera (Anton-Paar, Graz, Austria) with an X-Ray generator (PANalytical, PW3830, standalone laboratory X-ray source) operating at 40kV and 50 mV with a sealed-tube Cu anode was used to perform the small angle X-Ray scattering (SAXS) experiments. SAXS experiments allowed the investigation of the material distribution in multi-shell CdSe/ZnS/CdSe/ZnS NCs (chapter 3).

5. Fluorescence quenching for small molecule biosensing

This chapter describes the use of long-range fluorescence quenching by gold nanoparticles (AuNPs) for an immunoassay for a small molecule called digoxigenin (Dig). The principle of fluorescence quenching is tested on small molecules, which are expected to provide relatively short separation distance from the dye molecule to the AuNP ensuring highly efficient quenching. Two test formats are introduced here: A simple and a competitive assay. The simple assay is used to optimize the quenching effect and to determine the fluorescence quenching mechanism. The competitive assay is used for the detection of the label-free Dig. Two cyanine dyes Cy3 and Cy3B are tested in order to find the fluorescent marker leading to the highest quenching. Fluorescence quenching mechanisms are investigated using time resolved spectroscopy. The results of time resolved measurements are compared with the Gersten-Nitzan theory.

5.1 Principle of simple and competitive immunoassays

Gold nanoparticles can quench fluorescence very efficiently. This allows for their applications in medical diagnostics. Digoxigenin (Dig) is a small molecule used as an analyte here.

The simplest possible configuration for biomolecule detection is the so called simple assay depicted in figure 5.1. A dye-labeled analyte binds to the antibody on the AuNP and the dye's fluorescence is quenched. In the reference AuNP functionalized with anti-troponin T (anti-TnT), to which Dig does not bind, are used. So the fluorescence in the reference stays unchanged. This method, however, has the critical disadvantage of the necessity to label all analytes with dyes. This is not practical in real applications, where it is necessary to detect the native unlabeled molecules in blood. Therefore a so called competitive test format is used in this work.[1]
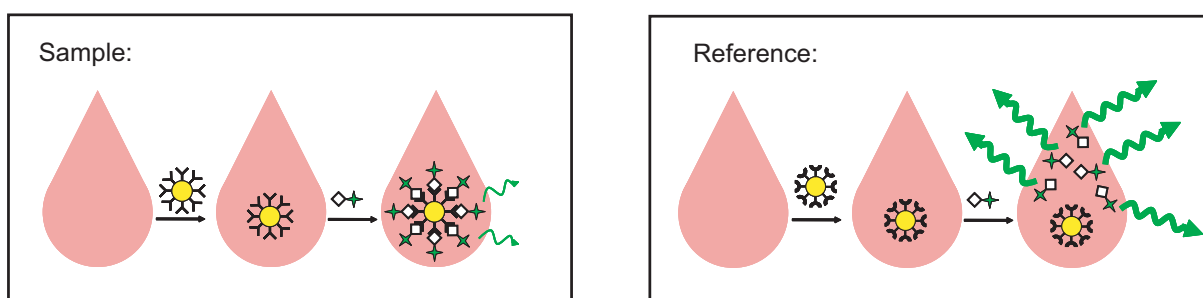
Figure 5.1: Principle of operation of the simple fluorescence quenching test. A dye-labeled analyte binds to the antibody on the AuNP and its fluorescence is quenched. In the reference, the marker does not bind to the AuNP and the fluorescence is not changed.

The principle of operation of the competitive test is shown in figure 5.2. Two samples are needed for the test: a sample with analyte (further called sample) and one without the analyte (further called reference). Two solutions with the same volumes and concentrations of AuNPs functionalized with anti-Dig antibodies are taken. A certain volume of analyte is added to the sample. The same volume of buffer is injected in the reference to ensure equivalent measurement conditions. Analytes occupy the available binding sites on the antibodies on the AuNP. Next, the fluorophore-labeled analyte (marker) is added to both solutions. There are less available binding possibilities in the sample than in the reference, because the analytes

---

[1]Sometimes in literature this test format is also called a displacement test [103].
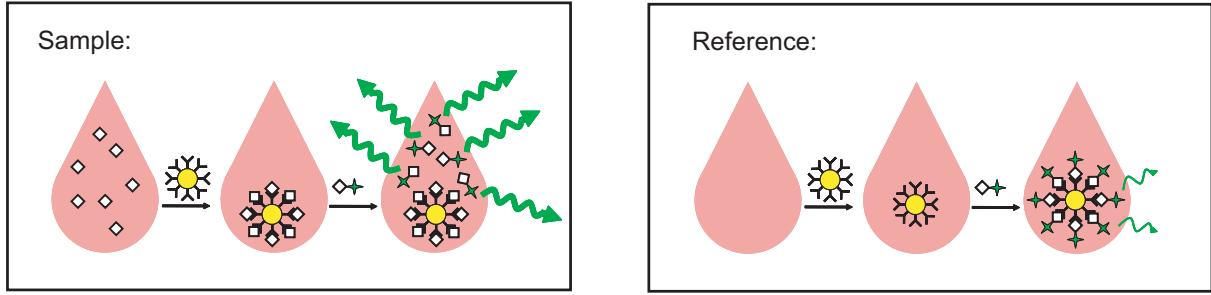
Figure 5.2: Principle of operation of the competitive test for Dig. AuNPs, functionalized with anti-Dig antibodies are incubated with Dig (sample) or without Dig (reference). The photoluminescence is measured after the incubation upon addition of fluorophore-labeled Dig. When no Dig is present in the solution, the fluorophore-labeled Dig can bind to anti-Dig and the fluorescence is quenched. If Dig is present in the solution, the binding sites of anti-Dig are occupied by Dig molecules and fluorophore-labeled Dig cannot bind to the AuNPs. Hence, the fluorescence is increased in comparison to the reference measurement.

already bound to AuNPs. Therefore the labeled analytes can bind to a larger extent in the reference than in the sample. Finally, the fluorescence of both samples is measured and compared. The fluorescence of the sample has a larger intensity than of the reference because there are more unbound fluorophores in the solution that are not quenched.

The difference between a simple and a competitive immunoassays is that in the simple assay quenching is observed in the sample. The reference is quenched in the competitive test. Therefore fluorescence quenching for both assays is calculated differently. In the simple assay fluorescence quenching is calculated as

$$FQ_{simple} = \left(1 - \frac{I_{sample}}{I_{reference}} \right), \tag{5.1}$$

in the competitive assay it is defined as

$$FQ_{competitive} = \left(1 - \frac{I_{reference}}{I_{sample}} \right), \tag{5.2}$$

where $I_{reference}$ is the PL intensity of the reference measured at the peak, and I_{sample} is the PL intensity of the sample with analyte measured at the peak.

5.2 Systems under consideration

In order to maximize the fluorescence quenching and consequently to approach the limits of the assay sensitivity, different fluorophores were tested. Bovine serum albumin (BSA) was used as a carrier protein, to which both Dig and Cy3 (figure 5.3(a)) or Cy3B (figure 5.3(b)) molecules were conjugated. One BSA molecule had two fluorophores and eight Dig molecules on it (section 3.1.2). AuNP with 10 nm diameter were functionalized with complete intact anti-Dig antibodies.

Measurements with variable ratios of AuNP to marker concentrations [AuNP]/[Marker] were performed to determine which marker is optimally quenched by AuNPs (figures 5.4(a) and 5.4(b)). In the graphs the fluorescence intensities of sample and reference are plotted for the simple assays. AuNPs functionalized with anti-troponin T (anti-TnT) were used as a reference.

It can be seen that in all cases the black curves, corresponding to the sample, lie below the blue and green colored reference curves. Fluorescence quenching increases with increasing [AuNP]/[Marker] ratio. This happens because more and more labeled analyte molecules bind to AuNPs. At some point, however, the number of labeled Dig molecules becomes larger than the number of available binding sites and no increase in fluorescence quenching is observed anymore. Thus, there is an optimal ratio between the concentrations of markers and of AuNPs, where quenching is maximal. When there are more markers available than

(a)

AuNP with anti-Dig
+
BSA-Cy3-Dig

(b)

AuNP with anti-Dig
+
BSA-Cy3B-Dig
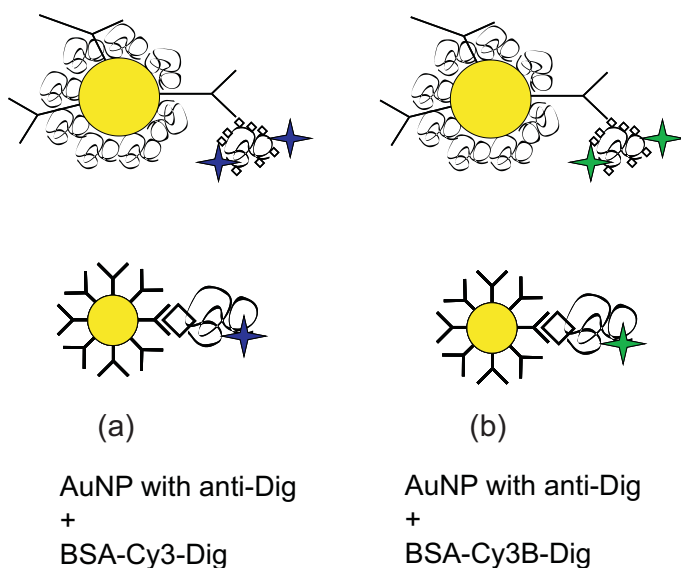
Figure 5.3: Dig systems under investigation represented schematically and pictographically. In all cases 10 nm AuNPs are functionalized with anti-Dig antibodies. The remaining free space on the surface of AuNPs was covered with BSA. A BSA carrier protein is used to host Dig molecules and Cy3 (a) or Cy3B (b) labels.

binding sites on AuNPs, then most of them remain unbound in the solution. Therefore they emit fluorescence and contribute to the background, thus lowering the observed fluorescence quenching. However, when there are less markers than binding sites on AuNP, there is a high probability that the markers will be bound and quenched.

The maximal quenching efficiency that could be achieved for the BSA-Cy3-Dig marker was 58 % and 76 % for the BSA-Cy3B-Dig marker. Therefore, the BSA-Cy3B-Dig marker is more useful for making sensitive assays.
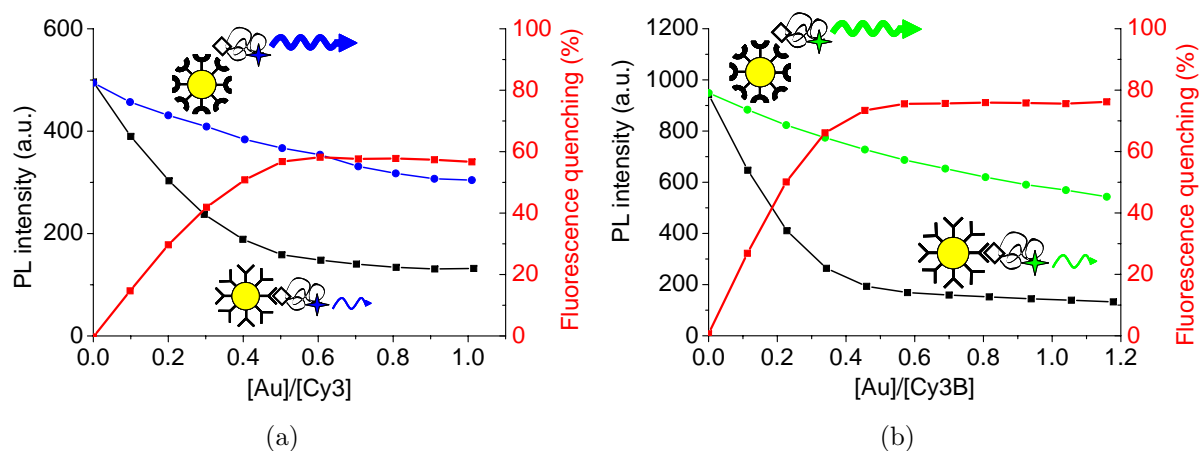
Figure 5.4: A saturation experiment with BSA-Cy3-Dig (a) and BSA-Cy3B-Dig (b) markers. The blue and green curves refer to the reference, where Dig cannot bind to AuNPs functionalized with anti-TnT antibodies. The black curve is the quenched sample. Fluorescence quenching (equation 5.1) is plotted in red. Lines connecting the points are guides for the eye.

5.3 Binding kinetics

In the previous section two markers were considered concerning their maximal achievable quenching efficiency for the case of the simple assay. Now the competitive assay is considered in order to study the dynamics of the competitive binding of the analyte to anti-Dig antibodies on AuNPs. This leads to a greater understanding and control of the maximally achievable detection sensitivity of the immunoassay. Since BSA-Cy3B-Dig was shown to produce the largest fluorescence quenching among the markers, it was used for the assay sensitivity assessment described in this section.

Fluorescence intensity can be used to observe the binding dynamics in the system under investigation. Figure 5.5(a) shows how the intensity develops within 10 min after the addition of the marker. In the reference, pure binding dynamics of the labeled analyte can be observed. In the sample, however, two species compete for the binding sites on the AuNPs. Therefore, the amount of bound labeled analytes is lower, so the quenching dynamics are slower. These time-dependent measurements enable the determination of the optimal measurement time point, where quenching is maximal. Time dependent fluorescence quenching (figure 5.5(b)) shows that 155 s after mixing the sample the effect reaches its maximum. After this point an equilibrium is established in the system. It can also be concluded from these measurements that sample and reference need to be measured simultaneously to obtain a correct value for fluorescence quenching.
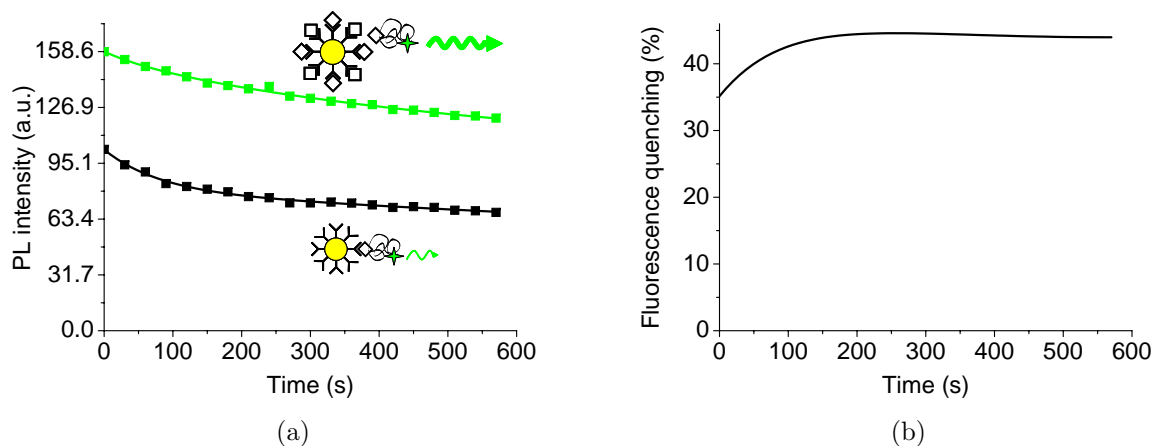
Figure 5.5: (a) Development of fluorescence intensity with time in the sample (green line) and in the reference (black line) within 10 min. In both cases binding of the dye-labeled analyte and subsequent fluorescence quenching by the AuNP can be seen. The quenching dynamics in the sample is different from the reference because in the sample a competition between the labeled and unlabeled analytes takes place. (b) Dependence of fluorescence quenching (equation 5.2) in time. After the steep increase due to faster binding of the reference the maximal effect is reached at 155 s followed by saturation.

5.4 Immunoassay sensitivity

The concentrations of the marker and the AuNPs have to be chosen properly to maximize the sensitivity of this competitive test. This should be done in a way that a maximal quenching effect can be seen. Under these conditions, the presence of analyte delivers a detectable difference in fluorescence intensity between the sample and the reference. However, for small concentrations of analyte there will be many free markers in the solution providing an undesirably high background level. Following this logic, a lower concentration of dye should be chosen. It is difficult to detect the fluorescence because of the signal weakness if the fluorophore concentration becomes too low. Also, the AuNP concentration cannot be chosen too high because of the increasing reabsorption of fluorescence by AuNPs. Therefore a compromise should be made in choosing the dye and AuNP concentrations for the test.

The limit of detection and quantitation (section 2.3.1) of the test in buffer were determined from a series of measurements with blank samples. The limit of detection (LOD) equals 0.49 nM and the limit of quantitation (LOQ) is 1.64 nM (corresponding to 0.19 ng/mL and 0.64 ng/mL respectively). The dynamic range of the assay ranges from 1 to 8 nM (0.39 - 3.12 ng/mL), where the fluorescence quenching depends linearly on the analyte concentration (figure 5.6).

The therapeutically relevant concentration range for digoxin is 1 to 6 ng/mL [87]. This corresponds to 0.5 to 3 ng/mL for digoxigenin, considering the difference in molecular masses between digoxin and digoxigenin (section 3.1.4). Therefore the obtained dynamic range of
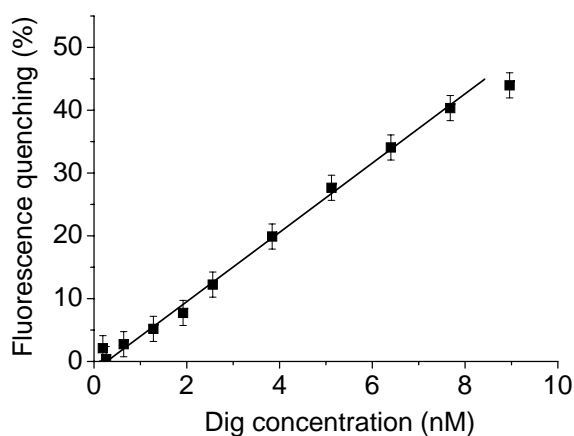
Figure 5.6: Fluorescence quenching (equation 5.2) effect as a function of the digoxigenin concentration. The dynamic range of the assay ranges from 1 to 8 nM, where the effect depends linearly on the analyte concentration.

0.39 - 3.12 ng/ml would also cover the interesting detection range for digoxin if the assay were applied to detect it.

The developed detection method was tested in human serum in order to study the possibility of practical applications. A measurement in serum can be a challenge for an immunoassay, because of the high content of proteins and other organic molecules in serum. Different non-specific reactions are possible in serum. Additionally, the large optical density of serum in the visible range poses a problem, because it creates a high scattering background signal at the wavelength where the fluorescence is measured (figure 5.7(a)). Due to the high specificity of antibodies to the antigen, the first issue did not pose a problem. But absorption of serum required adjustments. The measurements in serum needed to be carried out under laser illumination near the cuvette wall. In this way the illumination power was sufficient to excite the fluorophores in the cuvette despite of serum absorption and scattering. The laser went parallel and close to the cuvette wall closer to the detector. This allowed the fluorescence light to have only a short optical path in serum before leaving the cuvette, thus minimizing reabsorption. The fact that fluorescence quenching was detectable in this configuration means that eventually very small volumes of serum could be used for the experiments.

Serum content in this experiment was 90% of the total solution volume (figure 5.7(b)).
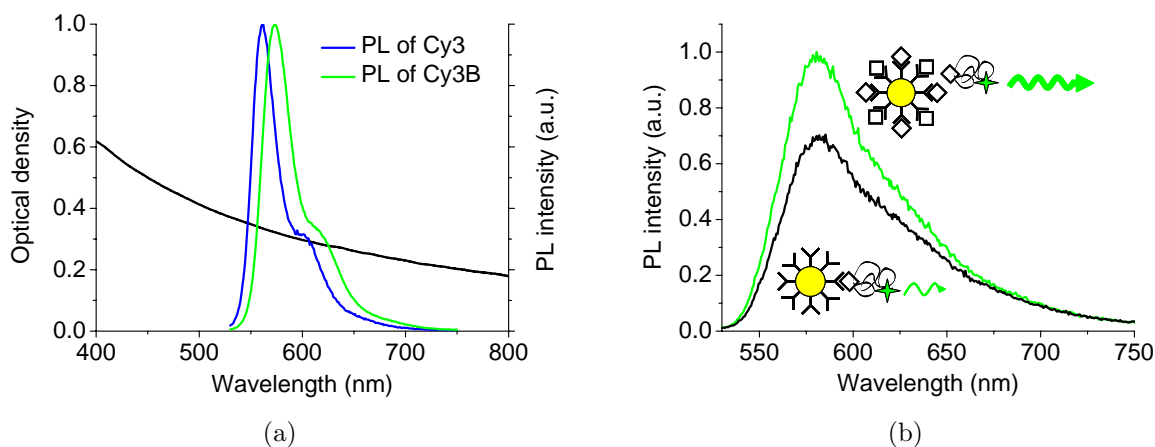
Figure 5.7: (a) Optical density of human serum measured in a cuvette with a 1 cm optical path. Serum absorbs strongly in the visible range where dye fluorescence occurs. (b) Fluorescence intensities of sample (green) and reference (black) in serum. The amount of serum in the measured solution is 90%. The Dig concentration is 50 nM.

The competitive digoxigenin test in serum allowed the detection of a concentration of 50 nM. This is a significantly higher concentration than what can be detected in buffer because the reabsorption of serum could not be completely overcome. So, the assay in serum needs further optimization to reach lower concentrations. This could be achieved by using cuvettes with a shorter optical path.

There are a number of established assays for digoxin, both commercial and non-commercial [104–108]. These tests are based on different detection principles such as the use of microparticle enzyme immunoassay (MEIA/AxSYM from Abbott), electroluminescence assays (Elecsys from Roche Diagnostics), chemiluminescence assays (ACS from Bayer/Siemens, Vitros from Ortho/Johnson&Johnson), turbidimetric assay (TinaQuant from Roche, Synchron-LX from Beckman), enzyme-multiplied immunoassay technique (EMIT from Syva-Behring/Siemens) and fluorescence polarization immunoassay (TDx from Abbott). The lowest limit of detection achievable in these tests is 0.2 ng/mL [108]. These commercial assays have been optimized in the product development process. The fluorescence quenching assay developed in this work has a limit of detection of 0.19 ng/mL in buffer, which is very close to the commercial achievement. Further development of the test in serum and systematic effort on improvement of the test sensitivity were not the subject of this investigation. However, the fluorescence quenching test developed in this work has an advantage that no separation step of the bound and unbound systems is involved. The measurement of fluorescence quenching as such is very quick and can be performed in about 300 s. However, the preparatory incubation time here was 30 min, which might be shortened in future assay optimization. This approach can also be used to detect other small molecules.

5.5 Investigation of fluorescence quenching mechanisms

It was introduced previously that AuNPs can quench the fluorescence of dye molecules through radiative rate suppression and energy transfer (section 2.2.2). Time-resolved PL measurements allow the determination of processes underlying fluorescence quenching by AuNPs. The radiative, non-radiative and energy transfer rates of the molecule can be determined by analyzing the transients. These measurements also allow the determination the

true quenching efficiencies of fluorescent markers because the background of free unbound markers can be subtracted.

Experiments were performed for the simple assay, i.e. without the non-labeled analyte, because the focus of investigation was the quenching process as such. AuNPs functionalized with anti-troponin T, to which Dig does not bind, were taken as a reference.

5.5.1 Determination of radiative and non-radiative rates

A free dye without an AuNP is expected to have a mono-exponential decay of fluorescence intensity $I(t) \sim e^{-t/\tau}$ after optical excitation. When AuNPs are added to the system, only a part of them binds to the fluorophores. Therefore, two fluorescent species are present in the mixture: Fluorescent molecules bound and unbound to the AuNP. The dependence of fluorescence intensity on time is described by a double exponential (figure 5.8)

$$I(t) = n_f \Gamma_r e^{-t/\tau} + n_b \Gamma_r' e^{-t/\tau'}, \tag{5.3}$$

where n_f and n_b are the numbers of free and bound dye molecules, Γ_r and Γ_r' are the radiative rates of the free and bound dye molecule, τ and τ' are the lifetimes of the free and bound fluorophores. The lifetime for the decay of free dye is unchanged in the presence of AuNPs. The fluorescence decay curve of the unbound can be subtracted from the total decay in order to obtain the values for the fluorescence intensity $I'(0)_q$ at time 0 of the dye near the AuNP [43].

The radiative and non-radiative rates Γ_r and Γ_{nr} can be calculated if the quantum efficiency Φ and lifetime τ of free dye are known

$$\Gamma_r = \frac{\Phi}{\tau}, \tag{5.4}$$

$$\Gamma_{nr} = \frac{1 - \Phi}{\tau}. \tag{5.5}$$

The fluorescence intensity of free dye immediately after the laser pulse is proportional to the product of the number of dye molecules and the radiative rate $I(0) = n\Gamma_r$. To

Figure 5.8: Scheme of the time resolved data analysis. Intensity is plotted on a logarithmic scale. Free dye decays mono-exponentially (triangles). Dyes connected to AuNPs decay double exponentially (squares) because there are not bound dyes with the same decay time as free dye (blue) and bound dyes with shortened life-time (red). The intensity at time 0 is decreased if the radiative rate suppression takes place.
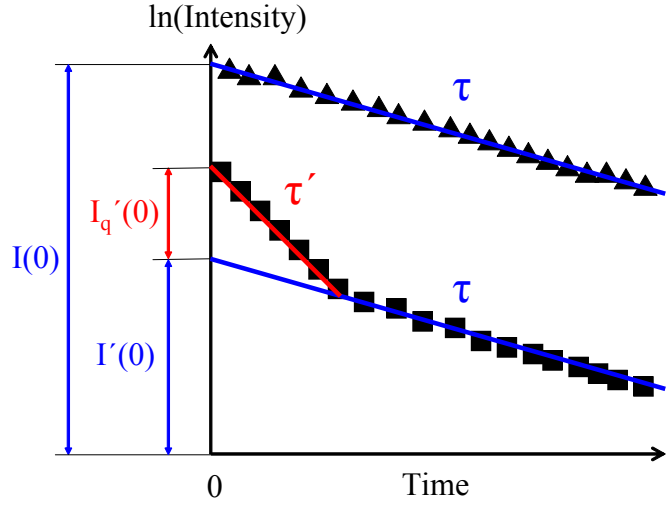
determine the change in the radiative rate, the intensities at time 0 of the same number of free and bound fluorophores must be compared. $I'(0)$ is the initial intensity of unbound dye molecules in the quenched system (figure 5.8). The same number of fluorophores in the quenched and the reference sample can be obtained by subtracting $I'(0)e^{-t/\tau}$ from the experimental fluorescence decay curves for the bound and unbound systems. Thus, one can determine the changed radiative rate by comparing the initial fluorescence intensities

$$\Gamma'_r = \frac{I'_q(0)}{I(0) - I'(0)}\Gamma_r. \tag{5.6}$$

Consequently the non-radiative rate of the dye-AuNP system can be determined as

$$\Gamma'_{nr} = \frac{1}{\tau'} - \Gamma'_r, \tag{5.7}$$

where the lifetime τ' of the dye-AuNP system can be measured. Finally, the contribution of energy transfer to the changed non-radiative rate can be calculated as

$$\Gamma_{ET} = \Gamma'_{nr} - \Gamma_{nr}. \tag{5.8}$$

Knowledge of the rates of the hybrid system leads to the quantum efficiency

$$\Phi' = \frac{\Gamma'_r}{\Gamma'_r + \Gamma'_{nr}}, \tag{5.9}$$

and the PL quenching efficiency

$$\eta_q = 1 - \frac{\Phi'}{\Phi}. \tag{5.10}$$

5.5.2 Non-radiative rate and energy transfer

The results of time resolved measurements are shown in figures 5.9(a) and 5.9(b). The graphs show the fluorescence decays of all studied systems. The component with the long lifetime corresponding to free dye was subtracted on all graphs, as shown on figure 5.8. The number of fluorescent molecules in the sample and in the reference is thus the same in the plotted curves (black vs. green and black vs. blue lines). A common feature of all decays is the significant decrease of fluorescence lifetime in the vicinity of an AuNP (black lines) compared to the references, for which a dye is not bound to the AuNP (blue and green lines).

Lifetime reduction is an indication of an additional non-radiative decay channel in all systems. So, the non-radiative rate is increased in all systems (figure 5.10). This effect can be caused either by charge transfer or by energy transfer from the dye to the AuNP. A dye can be situated no closer than 3.2 nm to the AuNP. This is the size of BSA, which is used to cover the surface of the AuNP on the places where antibodies did not adsorb. Charge transfer does not take place at such long distances, so energy transfer must be responsible

(a)

(b)
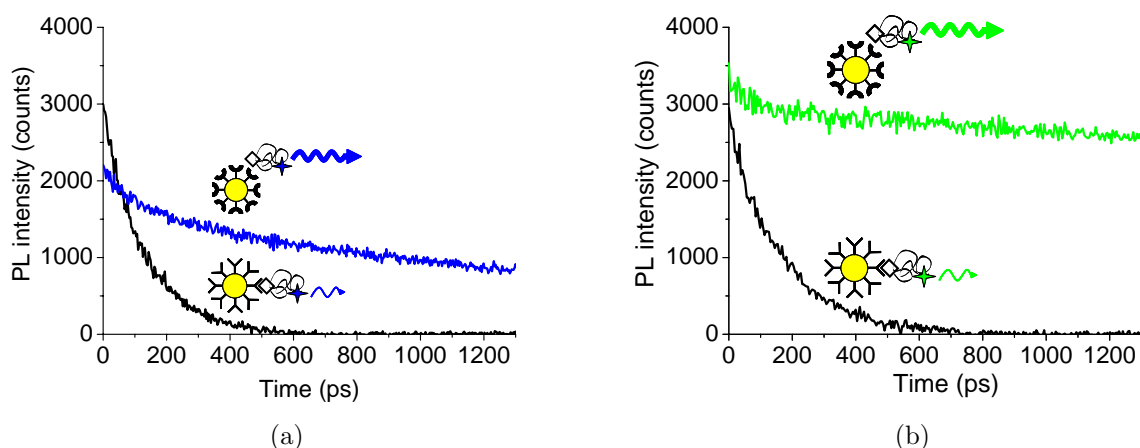
Figure 5.9: Time resolved fluorescence decays of the BSA-Cy3-Dig (a) and BSA-Cy3B-Dig (b) systems. The fluorescence lifetime in the quenched samples (black lines) for both markers (a, b) is reduced. This is an indication of energy transfer.

for the shortening of fluorescence lifetime.

Figure 5.10: Non-radiative rates of free dye and dye with AuNPs for BSA-Cy3-Dig and BSA-Cy3B-Dig systems. In both systems a significant increase in the non-radiative rate of the dye is observed in comparison to the reference, for which the dye was not bound to the AuNP.
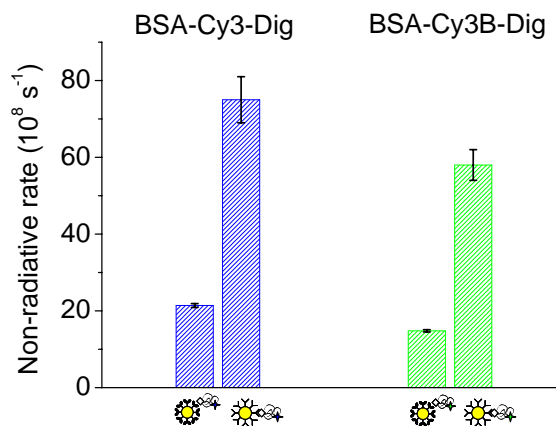
Energy transfer efficiency is calculated as

$$\Phi_{ET} = 1 - \frac{\tau'}{\tau}, \tag{5.11}$$

where τ is the lifetime of the free dye, τ' is the lifetime of the dye in the presence of the AuNP. The results are shown in figure 5.11. Energy transfer efficiencies for both markers were 70 %.
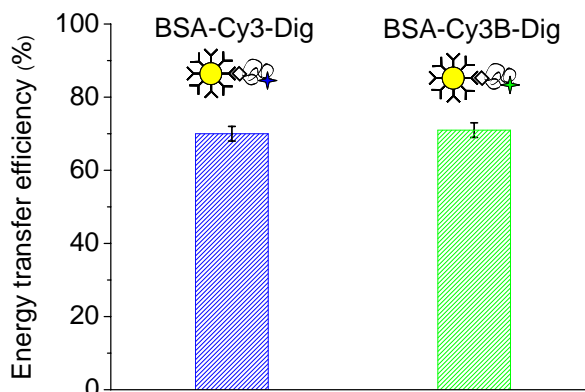
Figure 5.11: Energy transfer efficiencies for BSA-Cy3-Dig and BSA-Cy3B-Dig systems. The efficiency is 70 % for both markers.

5.5.3 Radiative rate suppression and enhancement

Another possible mechanism of fluorescence quenching by AuNPs is the radiative rate suppression. Since the fluorescence decays of free markers are mono-exponential, radiative rate is proportional to the fluorescence intensity at time 0 [30]. Radiative rates for both the free marker and dye with AuNP are shown in figure 5.12. The radiative rate increased 1.4 times in BSA-Cy3-Dig system and in BSA-Cy3B-Dig it decreased 1.2 times. In BSA-Cy3B-Dig system radiative rate suppression contributed to fluorescence quenching. The observation of the radiative rate suppression speaks for the preferentially tangential orientation of the dye transition dipole moments to the AuNP surface. In the BSA-Cy3-Dig system the radiative rate is increased. This fact can be a result of the predominantly perpendicular orientation of the dye transition dipole to the AuNP surface. Although it is expected that the orientation of the dye to AuNP surface is random, it is still possible that in the present labeled batch most of dye transition moments have a preferred orientation.

The amount of bound dyes can be calculated from the intensities at time 0 as $Bound = \left(1 - \frac{I'(0)}{I(0)}\right) \cdot 100\%$, as can be seen from figure 5.8. According to this formala, the percentage of bound dyes is 47 % for BSA-Cy3-Dig and BSA-Cy3B-Dig. Background fluorescence results from the emission of the remaining 53 % of unbound dyes in the solution.
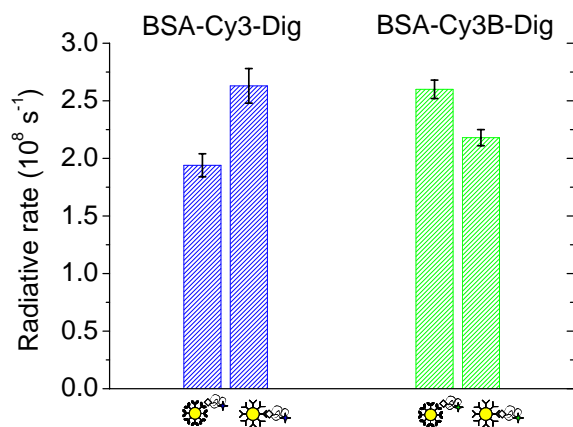
Figure 5.12: Radiative rates of free dye and dye with AuNPs for BSA-Cy3-Dig and BSA-Cy3B-Dig systems. The presence of the AuNP leads to the enhancement of the radiative rate in the BSA-Cy3-Dig system and suppression of the radiative rate in the BSA-Cy3B-Dig system.

5.5.4 Fluorescence quenching efficiency

PL quenching efficiency can be calculated from time-resolved measurements using the equation 5.10. The resulting number was 59 % for BSA-Cy3-Dig and 76 % for the BSA-Cy3B-Dig marker. The maximal quenching efficiencies that were obtained from the steady state measurements (section 5.2) 58 % and 76 % for BSA-Cy3-Dig and BSA-Cy3B-Dig respectively. The values for both markers are in excellent agreement.

The highest quenching efficiency was obtained in the BSA-Cy3B-Dig system because here the radiative rate suppression also contributed to fluorescence quenching. Additionally, the higher quantum efficiency and longer fluorescence lifetime of the Cy3B marker are important. The difference in fluorescence quenching of two dyes becomes clear from the Gersten-Nitzan model simulations as can be seen in figure 5.13. According to the calculation, Cy3B dye is expected to be quenched stronger than Cy3.

5.5.5 Comparison with the Gersten-Nitzan model

The results of the time-resolved measurements can be compared with the Gersten-Nitzan model (section 2.2.4). The model allows calculation of the radiative and non-radiative rates and quantum efficiencies for tangential and radial orientations of the fluorophore's transition dipole to the AuNP surface. In the systems under consideration the orientation is not exactly known and it is expected that the dye molecule, which is connected by a single covalent bond, is highly mobile and can rotate in its position. This results effectively in a random orientation

Figure 5.13: Gersten-Nitzan model calculations of the quantum efficiency for BSA-Cy3-Dig (blue curve) and BSA-Cy3B-Dig (green curve) systems. The orientation of the dye to AuNP surface is random. The increase of the quantum yield for the BSA-Cy3B-Dig marker is steeper. Therefore, stronger fluorescence quenching is expected for Cy3B than for Cy3.
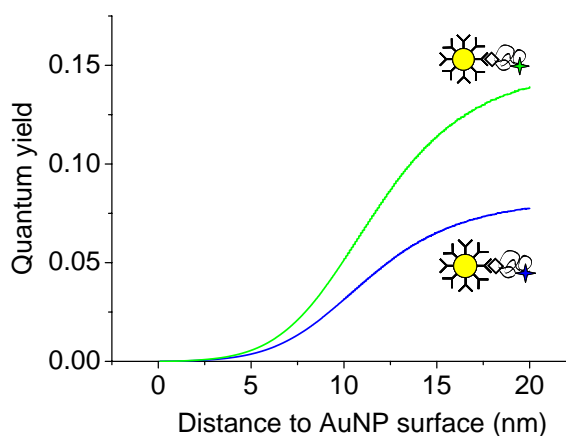
of the dye to AuNP surface.

Another important parameter in the model is the distance of the dye to the AuNP surface. This is also not exactly known in this system. This is because antibodies undergo adsorption on the gold surface in random orientations. This means that the binding sites are also situated at a range of different distances to the surface (figure 5.14).
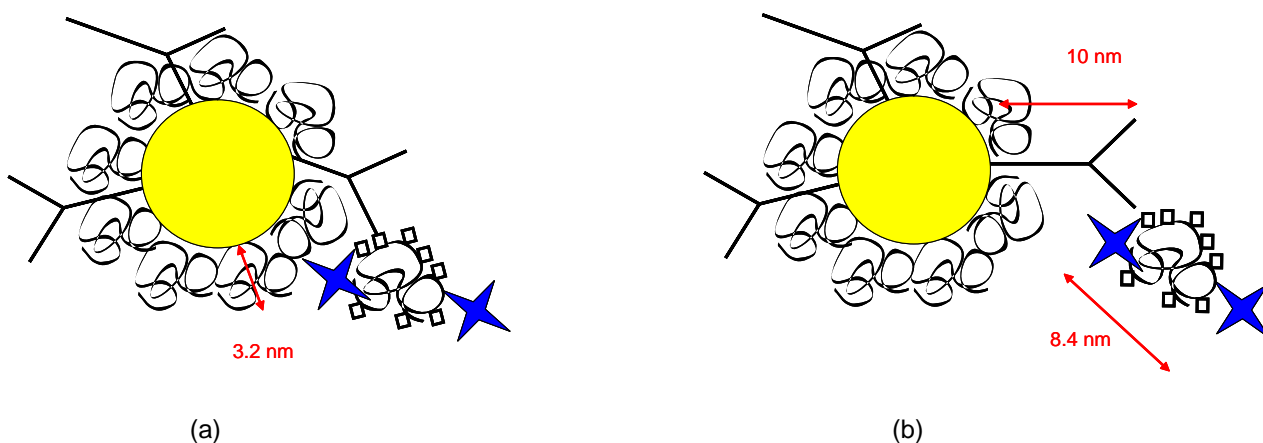
Figure 5.14: Shortest (a) and longest (b) possible distances between the dye and AuNP surface.

The length of a complete antibody is about 10 nm [109, 110]. BSA in aqueous solutions is prism-like, with an equilateral triangle with 8.4 nm side length as a base and height of 3.2 nm [81]. Dye and Dig molecules can bind to BSA in many locations (section 3.1.2), the most remote being 8.4 nm. Together with the maximal antibody extension of 10 nm this would result in 18.4 nm as the furthest dye-AuNP distance. The surface of AuNPs is passivated by BSA in the places where antibodies are absent. Therefore, the closest dye-AuNP distance is 3.2 nm, which is the height of the BSA molecule.

The values of the radiative and non-radiative rates as well as the quantum efficiency according to the Gersten-Nitzan model were calculated for the closest and most remote distances to AuNP surface (table 5.1). Theoretical calculations deliver values, which are of the same order of magnitude as the rates and quantum efficiency of the experimentally considered systems. For both markers the non-radiative rate and quantum efficiencies lie within the range of values calculated by the Gersten-Nitzan model. The deviations of the calculated values from experimental data are more significant for the radiative rate. Since the value of the radiative rate is extremely dependent on the orientation of the dye to AuNP

Table 5.1: De-excitation rates for BSA-Cy3-Dig and BSA-Cy3B-Dig systems with and without AuNPs compared to the calculations using the Gersten-Nitzan model. Calculations were performed for the minimally and maximally possible distances of 3.2 nm and 18.4 nm from dye to the AuNP. All values refer to the marker in the vicinity of an AuNP.

		BSA-Cy3-Dig	BSA-Cy3B-Dig
Maximal calculated radiative rate ($\times 10^8$ s^{-1})	$\Gamma_{r,max}$	3.03	3.81
Minimal calculated radiative rate ($\times 10^8$ s^{-1})	$\Gamma_{r,min}$	1.94	2.60
Measured rad. rate ($\times 10^8$ s^{-1})	Γ'_r	2.63 ± 0.15	2.18 ± 0.07
Maximal calculated non-radiative rate ($\times 10^8$ s^{-1})	$\Gamma_{nr,max}$	2690	2363
Minimal calculated non-radiative rate ($\times 10^8$ s^{-1})	$\Gamma_{nr,min}$	24	17
Measured non-rad. rate ($\times 10^8$ s^{-1})	Γ'_{nr}	75 ± 6	58 ± 4
Maximal calculated quantum yield	Φ_{max}	0.001	0.001
Minimal calculated quantum yield	Φ_{min}	0.075	0.134
Measured quantum yield	Φ'	0.034 ± 0.003	0.036 ± 0.003
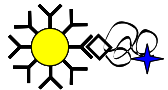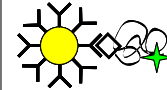
surface, it is the most difficult value to match to the experiments. As it could be seen in the previous section, it is possible that sometimes a dye might have more of a normal orientation in the BSA-Cy3-Dig systems. This can be also seen from the calculations, which overestimate the radiative rate for BSA-Cy3B-Dig.

5.6 Conclusion

It was shown that fluorescence quenching through AuNPs is caused by radiative rate suppression and energy transfer, whereby the latter is the main responsible process. Two fluorescent labels Cy3 and Cy3B were compared regarding their interactions with AuNPs. It was found that Cy3B undergoes stronger quenching when situated at the same distance as Cy3. Model calculations also support this effect. This is due to the higher quantum efficiency and longer fluorescence lifetime of Cy3B compared to Cy3.

A fluorescence quenching immunoassay for digoxigenin was developed. This is the first competitive test for a therapeutically relevant small molecule based on fluorescence quenching by AuNPs. The test provides reliable detection of the analyte in buffer with a limit of detection of 0.49 nM (corresponding to 0.19 ng/mL). The dynamic range of the assay ranges from 1 to 8 nM (0.39 - 3.12 ng/ml). This covers the therapeutically relevant range for digoxin, for which the test can be also applied. Laser excitation and front-face detection was

necessary to detect Dig in a solution with 90 % serum content. Dig concentration of 50 nM (corresponding to 19.39 ng/mL) could be detected in serum.

6. Fluorescence quenching for protein biosensing

In the previous chapter, fluorescence quenching by gold nanoparticles (AuNPs) were used to detect small molecules. Detection of proteins by this method is a significantly more challenging task. Sizes of proteins can reach several nm and together with antibodies this would significantly increase the distance between the fluorophore and the AuNP. Therefore, a sandwich type assay for proteins is the testbed for the whole method of long-range fluorescence quenching by AuNPs. Immunoassays using energy transfer have mostly been performed in the competitive format. There are only a few publications on sandwich immunoassays using two dyes or a dye and a nanocrystal as a donor and an acceptor [111–113]. This is due to the large separation between the donor and acceptor in this format, which makes FRET inefficient. The use of AuNPs enables the use of long-distance fluorescence quenching for these immunoassays. Two variants of antibodies attached to AuNPs are investigated: intact antibodies and shorter F(ab')2 fragments. This is done in order to find the upper limiting distance of fluorescence quenching.

6.1   Principle of the sandwich immunoassay

A marker of myocardial infarction, cardiac troponin T (TnT), is used as an analyte. Two epitopes on TnT are known, to which two different antibodies can bind specifically. This fact allows the development of a sandwich-type immunoassay (figure 6.1).
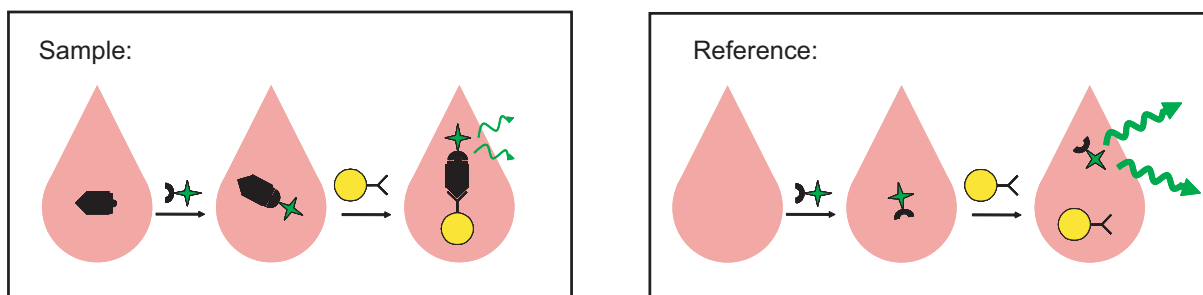
Figure 6.1: Schematic of the sandwich test for TnT. AuNPs are functionalized with anti-TnT antibodies. An antibody to a second epitope of TnT is labeled with a fluorophore. The system is bound together by the TnT molecule in the middle. As a result, the fluorescence of the dye is quenched by the AuNP.

One antibody is functionalized with a dye and the other is attached to an AuNP. When the analyte is added, a sandwich is formed consisting of a protein and two antibodies attached to it. The dye is brought in the vicinity of the AuNP and its fluorescence is quenched. The sandwich approach is different from the competitive test in that the analyte molecules need not be labeled by a fluorophore. Only the antibodies need to be labeled.

Fluorescence with analyte (sample) and without analyte (reference) were compared (figure 6.2). The figure shows that with analyte the fluorescence intensity of the marker decreased. Not complete quenching is due to the presence of free dye-antibody conjugates in the solution.
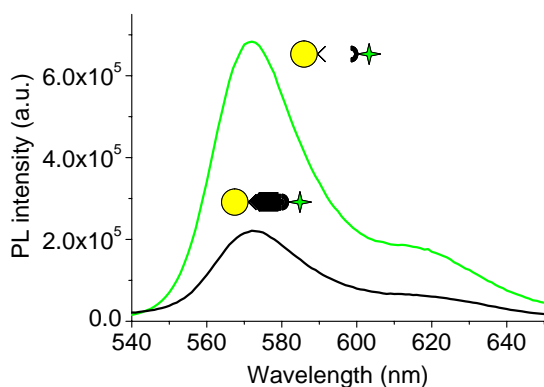
Figure 6.2: Example of quenching of fluorescence in a sandwich test. The sample contains the analyte and the reference does not. In this experiment concentrations of AuNPs, dye-labeled antibodies and TnT were 0.25 nM, 2.5 nM and 2 nM respectively.

6.2   Quantification of fluorescence quenching

Under real-life conditions TnT detection is performed with full blood or in serum of patients. TnT used in the experiment was obtained from Roche Diagnostics in lyophilized form together with serum. The serum content, which includes many different proteins, was present when the originally dry material was dissolved in water.

Figure 6.3: Photoluminescence of human serum depending on the concentration of TnT dissolved in serum. Increasing the concentration of TnT and thus of serum in the cuvette leads to higher luminescence intensity at the emission wavelength of fluorophores.
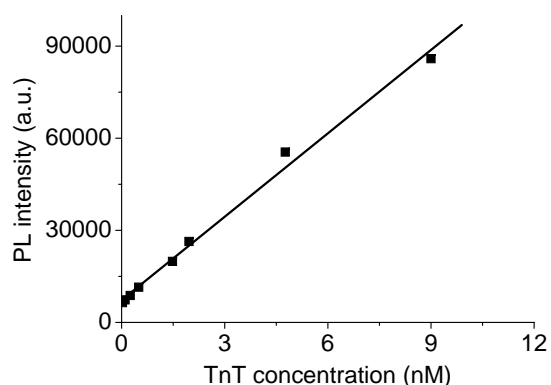
In figure 6.3 the luminescence of solution is plotted against the TnT concentrations. A fluorescent marker is not present in this sample. Serum and TnT have a background fluorescence signal of considerable intensity at the emission wavelength of the fluorophores. Considering this difficulty, a time dependent fluorescence intensity measurement procedure was applied. Continuous recording of fluorescence intensity before and after the addition of a defined TnT amount results in a detectable decrease of intensity (figure 6.4). This is caused by the formation of sandwiches and fluorescence quenching by AuNPs. Moreover, this method allows the observation of the binding kinetics of the system in real time. Small

Figure 6.4: Photoluminescence quenching in the TnT sandwich assay with stepwise addition of the analyte. Small peaks after the addition are caused by the fact that serum, in which TnT is diluted, is also fluorescent.

79
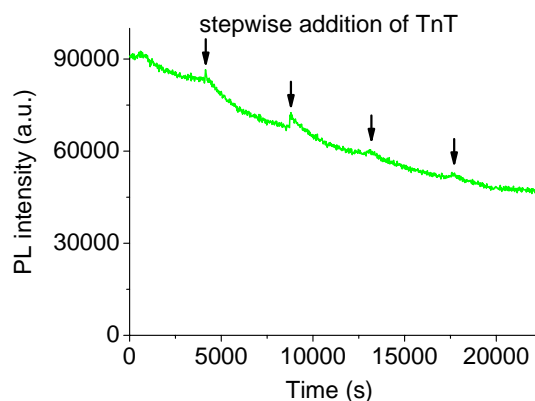
peaks appearing after the addition of TnT can be observed in the presented curve. These are caused by the fluorescence of serum, which at this marker concentration, is comparable to the fluorescence intensity of the dye.

6.3   Systems under consideration

In all sandwich biosensors AuNPs of 20 nm diameter were used. AuNPs and dyes were attached to complete intact antibodies (about 10 nm long) and to F(ab')2 antibody fragments (about 5 nm long). This allowed the design of long and short sandwich structures and to influence the dye-AuNP separation distance (figure 6.5). As in the previous chapter, fluorescence quenching of two dyes, Cy3 and Cy3B, was studied.

In the sandwich systems the distance between the dye and AuNP is not exactly known. However, it can be estimated from the sizes of single components. One complete intact antibody is 10 nm long [109, 110], and TnT is about 2.5 nm large [85]. F(ab')2 fragment consists of two 5 nm long Fab fragments, which are connected flexibly, so that they can produce an extension up to 10 nm. Fluorescent markers were attached to 5 nm long F(ab')2 fragments. AuNPs have not only antibodies, but also BSA molecules on their surface. BSA has 8.4 nm × 3.2 nm dimensions [81]. Possible distances from dye to AuNP surface for the short and long sandwiches are illustrated in figures 6.6 and 6.7. It follows that for the short and for the long sandwich the shortest distance, to which the dye molecule can approach the gold surface is 3.2 nm, the size of BSA. To estimate the maximal distance between the dye and AuNP surface, a situation must be considered, where the full maximal extensions of

(a)	(b)	(c)	(d)
AuNP with anti-TnT + F(ab')2-Cy3	AuNP with F(ab')2 + F(ab')2-Cy3	AuNP with anti-TnT + F(ab')2-Cy3B	AuNP with anti- F(ab')2 + F(ab')2-Cy3B
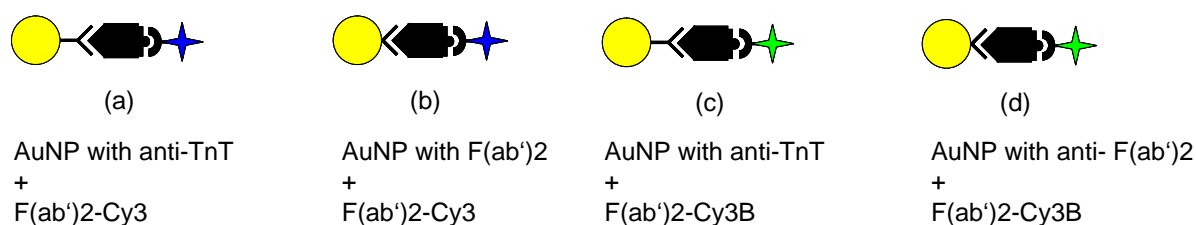
Figure 6.5: Schematic representation of TnT systems under investigation. Single components are not to scale. In all cases 20 nm AuNPs were used. AuNPs were functionalized with intact anti-TnT antibodies (a, c) and F(ab')2 antibody fragments (b, d). Cy3 dye (a, b) and Cy3B dye (c, d) were used as fluorophores.

antibodies and F(ab')2 fragments are taken into account. This leads to a maximal distance of 22.5 nm for the short and for the long sandwich.
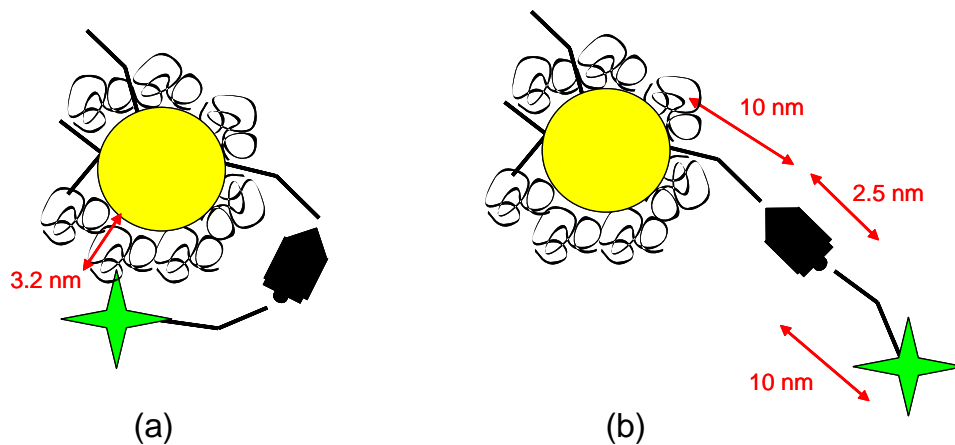
Figure 6.6: Minimal (a) and maximal (b) possible distances between the dye and AuNP surface in the short sandwich. Sizes of components are not to scale.
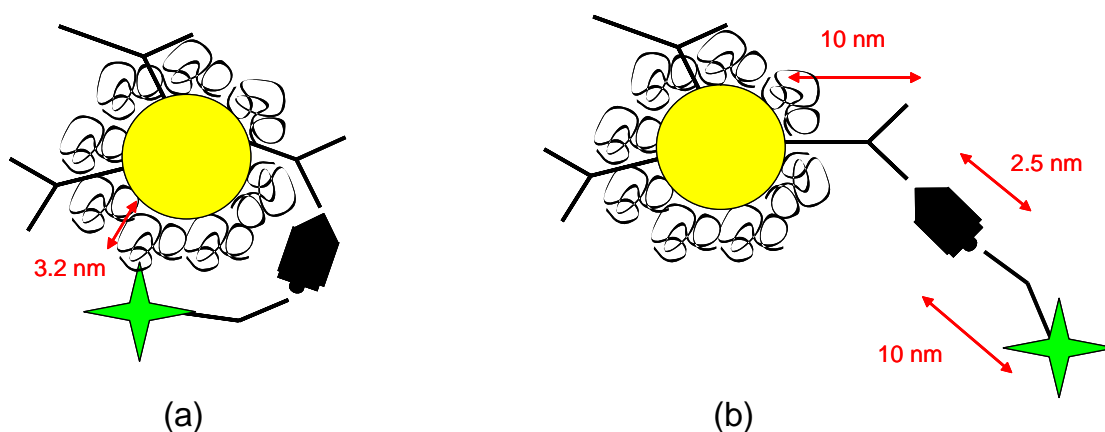
Figure 6.7: Minimal (a) and maximal (b) possible distances between the dye and AuNP surface in the long sandwich. Sizes of components are not to scale.

6.4 Binding kinetics

Compared to immunoassays of the competitive type (chapter 5), a sandwich immunoassay is more complex because it involves two binding reactions. Two antibodies need to bind to TnT so that dye fluorescence can be quenched by the AuNP (figure 6.8).
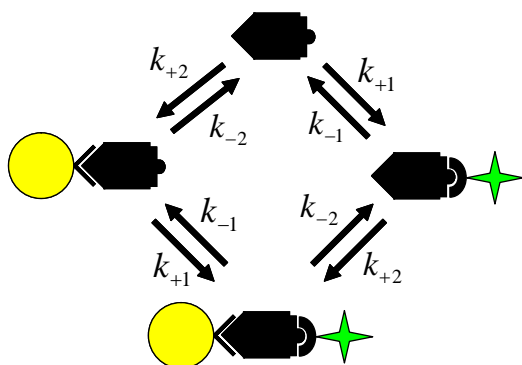
Figure 6.8: Different binding pathways in the sandwich immunoassay. Two antibody-antigen reactions must take place for the sandwich to form.

Continuous addition of analyte to the solution with fixed concentrations of AuNP and dye leads to decreasing fluorescence (figure 6.9). This corresponds to the concentration range, where the quenching effect is linear with the analyte concentration. As more sandwiches can be built, the fluorescence of bound dye decreases. At a certain point quenching reaches a minimum. This happens when the analyte concentration is optimal and the number of sandwiches formed in the solution reaches maximum. Further addition of the analyte leads to a decrease in the sandwich concentration and consequently to the increase of total fluorescence. This occurs because there are so many analyte molecules that most of the antibodies with dye or AuNPs are passivated by them. The possibility of sandwich assembly is significantly
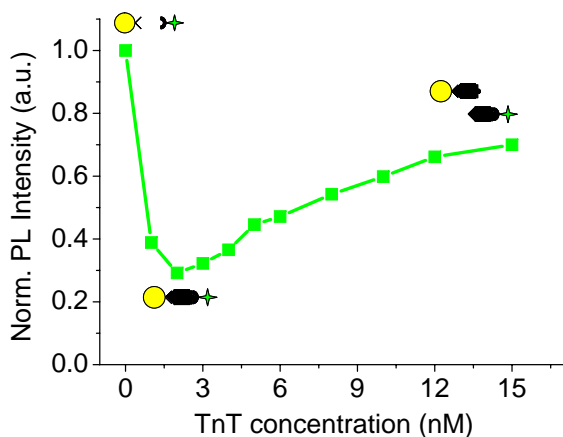
Figure 6.9: High dose Hook effect in the TnT sandwich assay. Only the region from 0 to the minimum is relevant for unambiguous analyte detection and quantitation, because after this point the assay becomes saturated by the analyte. Concentrations of AuNPs and dye-labeled antibodies were 0.25 nM and 2.5 nM respectively.

decreased. This effect is known in biosensing literature as the high dose effect or the Hook effect [114]. Therefore, it is important to choose proper dye and AuNPs concentrations to be able to operate the biosensor in the linear regime.

One experiment, such as the one presented in figure 6.9, is very time consuming. Therefore, computer simulations of binding kinetics were employed to understand the binding dynamics in the system and to optimize it. Modeling can help to find the optimal conditions in the experiments and to understand the trends in improving sandwich formation when the concentrations of components are varied. Within this work, a Mathematica program was developed to carry out the simulations based on the model by Zuber et al. [114]. Equations used for the modeling can be found in the appendix. In the model, the number of assembled sandwiches is calculated from the known concentrations of components.

Figures 6.10(a) and 6.10(b) show the results of the simulations for the varied AuNP and dye concentrations. When the concentration of AuNPs is increased, the dynamic range of the assay broadens and at some point the sharp minimum turns into a plateau (figure 6.10(a)). The fluorescence quenching effect also becomes more pronounced within this trend. The increase of dye concentration with fixed AuNP concentration also leads to a broadening of the dynamic range, but the depth of the minimum in fluorescence quenching decreases. These calculations show the direction to achieve maximal fluorescence quenching and a broad

(a)   (b)
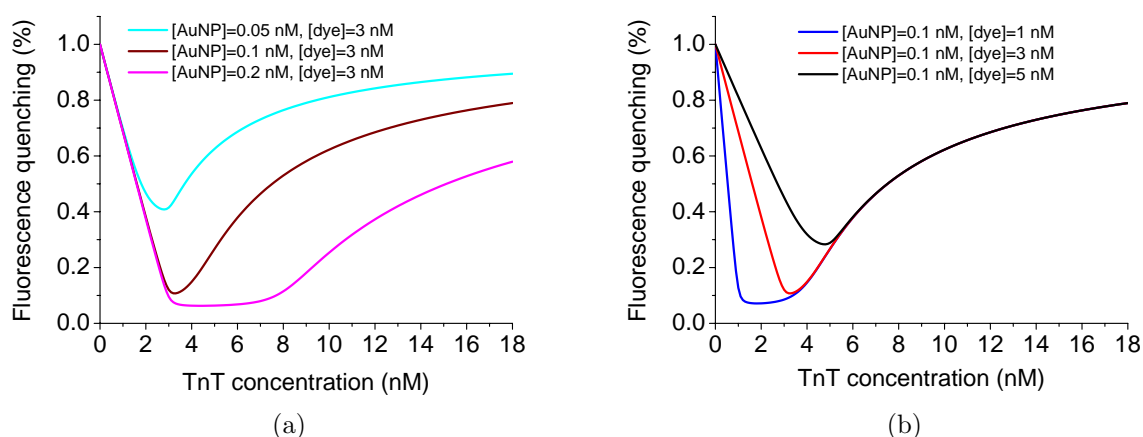
Figure 6.10: Fluorescence quenching simulations of the sandwich immunoassay with varied AuNP (a) and dye (b) concentrations.
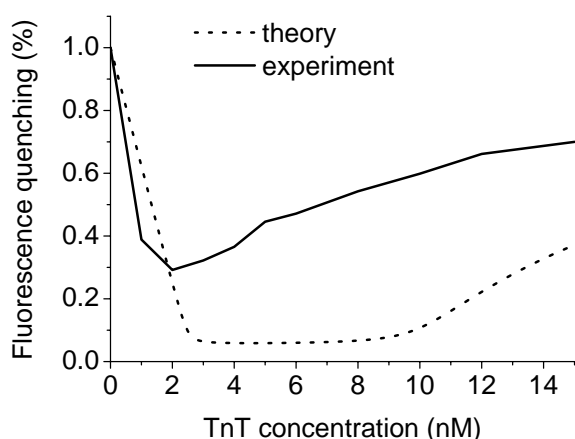
Figure 6.11: High dose Hook effect in the TnT sandwich assay obtained experimentally (solid line) and theoretically (dotted line). Concentration of AuNPs is 0.25 nM and dye is 2.5 nM.

dynamic range of the biosensor.

Another insight won from the simulations is that upon the increase of AuNP and dye concentrations the minimum shifts to larger analyte concentrations. This means that a larger sensitivity, corresponding to a larger quenching upon small change of the analyte concentration, requires both low dye and AuNP concentrations. On the one hand, this is beneficial because then fluorescence reabsorption by AuNPs is reduced. On the other hand, a too low dye concentration cannot be detected by the photomultiplier. Therefore that a compromise must be made in choosing the AuNP and dye concentrations for optimal detection sensitivity.

The comparison of the experimental data with the theoretical model is shown in figure 6.11. The fit of the simulation data to the experimental results is not perfect for a number of reasons. One is that the concentration of free dye in the solution might not exactly be described by the model because a certain amount of labeled antibodies could be adsorbed on the cuvette walls. Additionally, a dye in the vicinity of an AuNP experiences excitation enhancement due to the AuNP, which is not included in the model. This effect is difficult to account for because the orientations and distances of dye to the AuNP surface are not precisely known for the investigated system. Although the model does not exactly describe the data quantitatively, the qualitative predictions are important in preparing and understanding the experiments.

6.5   Sandwich assay sensitivity

Different measured dependencies of fluorescence quenching on the analyte concentration are shown in figure 6.12. In this graph the quenching effect is plotted against the analyte concentration for two different concentrations of dye-antibody conjugates and AuNPs. For smaller dye-antibody concentrations, the increase of the quenching effect is steeper. This happens because the fluorophores, being only few in the solution, react to small changes in the analyte concentrations by finding the partners to form a sandwich and being quenched by AuNPs.

The limit of detection and limit of quantitation of the developed assay in buffer were 0.02 nM and 0.03 nM (corresponding to 0.7 ng/mL and 1.1 ng/mL) respectively. These values are obtained from a number of measurements with a blank assay, i.e. without the addition of analyte. It is important to note that these numbers strongly depend on the choice of the AuNP and marker concentrations used in the test. As discussed above, the combination of these concentrations is responsible for the dynamic range and the ultimate sensitivity of this immunoassay.

The sandwich immunoassay was also tested with standardized samples from Roche Diagnostics in serum. The samples had a known concentration of TnT. The results of the measurements are shown in figure 6.13. Because of large signal fluctuations one can detect concentrations starting from 0.11 nM (corresponding to 4.0 ng/mL). Signal fluctuations here might be caused by the adsorption of TnT on the walls of test tubes, cuvettes and pipette tips or on other proteins contained in serum, which does not happen in buffer.

There are a number of existing immunoassays for TnT, some of which are commercially available. It is interesting to compare the currently achieved detection limits for the assay

Figure 6.12: Quenching effect for two different dye and Cy3B-antibody concentrations. For the red curve the sample contained 0.63 nM of labeled antibodies and 0.12 nM of AuNPs. For the black curve there were 0.02 nM of labeled antibodies and 0.06 nM of AuNPs. The smaller the dye concentration, the steeper is the dependence of PL intensity on analyte concentration and the more sensitive the assay for small concentrations.
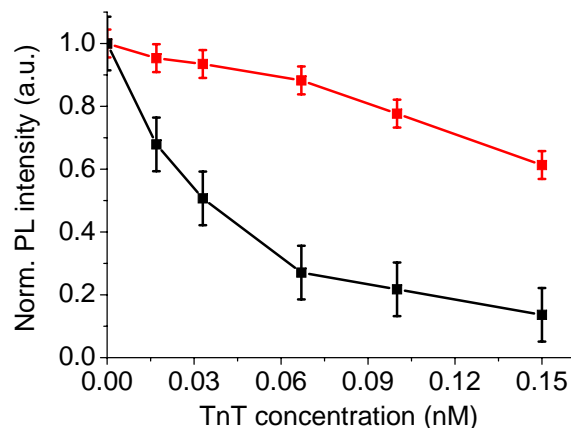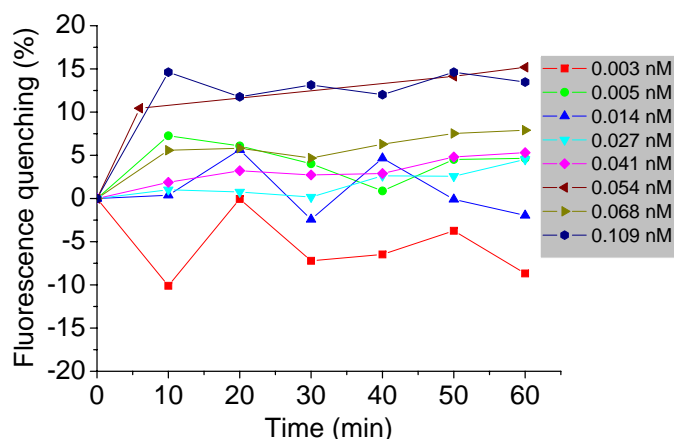
Figure 6.13: Time dependent fluorescence quenching. Measurements were performed in serum for different known concentrations of TnT in solution.

developed within this work with the existing tests. Recently, a surface plasmon resonance immunosensor was reported for TnT [115]. This assay has a detection limit of 0.01 ng/ml and a linear range from 0.03 to 6.5 ng/ml. An enzyme linked immunoassay for TnT has the limit of detection of 0.5 ng/mL [116]. The commercial point-of-care CardiacT test (Roche Diagnostics) has the limit of detection of 0.1 ng/mL [117]. The Enzymun assay from Roche Diagnostics has the limit of detection reaching 0.02 ng/mL [118]. The Elecsys test (Roche Diagnostics) has currently the highest sensitivity of 0.01 ng/mL [119]. The assay developed in this work with the limit of detection of 0.7 ng/mL in buffer and 4.0 ng/ml in serum is less sensitive than the existing tests, but reaches the therapeutically relevant range.

6.6 Investigation of fluorescence quenching mechanisms

The mechanisms of long-range fluorescence quenching by AuNPs can be determined with the help of time resolved measurements. Figures 6.14(a), 6.14(b), 6.15(a) and 6.15(b) show the fluorescence decay curves of all investigated systems with and without analyte. A mixture of AuNPs and fluorophores without TnT was used as a reference.
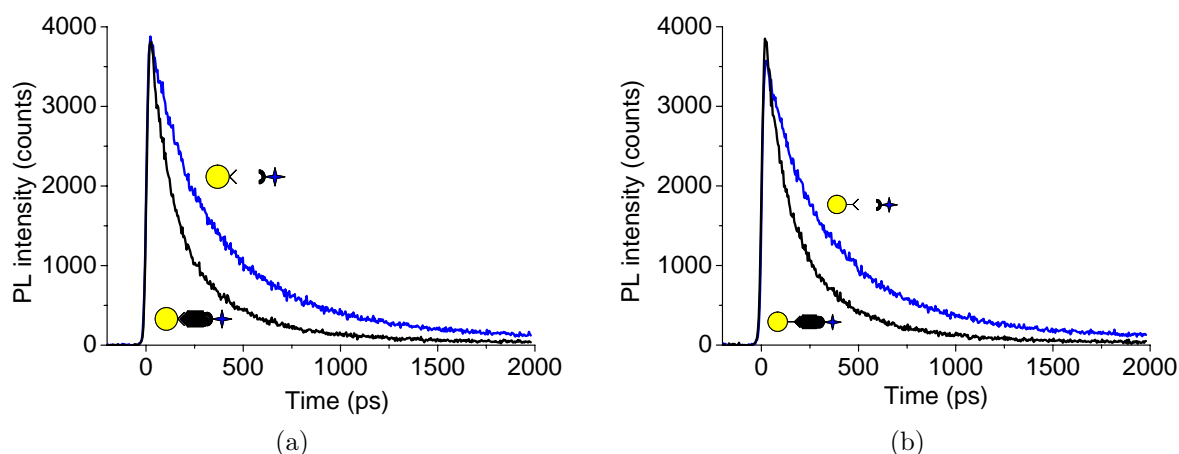
Figure 6.14: Fluorescence decays of the short (a) and long (b) sandwich immunoassays labeled by Cy3. The fluorescence lifetime is decreased in the sandwich system (black curve) due to energy transfer to the AuNP.
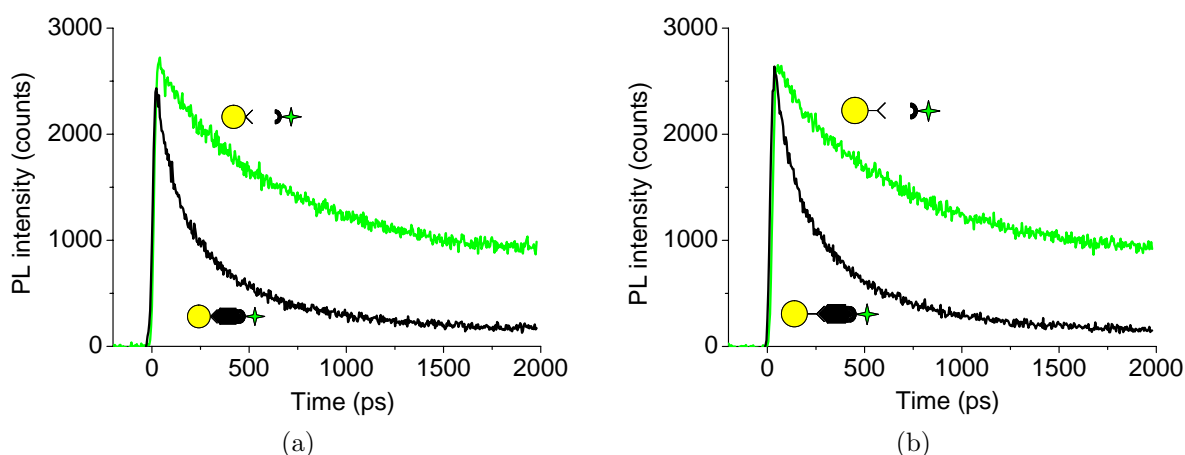
Figure 6.15: Fluorescence decays of the short (a) and long (b) sandwich immunoassays labeled by Cy3B. Energy transfer to the AuNP leads to the shortening of the excited state lifetime in the sandwich system (black curve).

6.6.1 Determination of radiative and non-radiative rates

In contrast to the dye-Dig conjugates discussed in the previous chapter, the fluorescence decay of the marker attached to the antibody is a double exponential $I(t) = A_1 e^{-t/\tau_1} + A_2 e^{-t/\tau_2}$ for both Cy3 and Cy3B dye labels and for the short and long antibodies. The reason for this is the influence of the conjugation of the dye molecule to the antibody on the properties of the dye. The antibody is a protein containing tryptophan, which is known to quench fluorescence

[80]. Since the dye can be attached at different positions on the antibody, there can be places where the fluorophore is close to the tryptophan and positions, where it is far away (figure 6.16). Therefore the decay time of some dye molecules can become shorter than the decay time of others due to tryptophan quenching. Additionally, it was reported that the lifetime of the Cy3 dye can change significantly when the dye molecules are chemically conjugated to other molecules because the conjugation changes the conditions for the isomerization of the dye [79, 120]. Therefore, an increase of the lifetime of the dye on the protein surface is also possible.

Based on these arguments, data analysis for the sandwich assays was performed as described in section 5.5.1 separately for both time constants in the fluorescence decay of the free dye. This means that each system consisted of two subpopulations of fluorescent markers with different fluorescence lifetimes. Every marker has a fast and a slow component $I(t) = A_f e^{-t/\tau_f} + A_s e^{-t/\tau_s}$. The percentage of the fast subpopulation can be calculated from the amplitudes of the decays A_f and A_s as $P_f = \frac{A_f}{A_f + A_s}$.

The fluorescence decays of quenched dye molecules is fitted with a fourfold exponential

$$I(t) = A'_f e^{-t/\tau_f} + A'_s e^{-t/\tau_s} + A'_{fq} e^{-t/\tau'_f} + A'_{sq} e^{-t/\tau'_s}, \qquad (6.1)$$

where A'_f, A'_s, τ_f and τ_s describe the parameters of the dyes, which stay free in the solution; A'_{fq}, A'_{sq}, τ'_f and τ'_s refer to the molecules influenced by AuNPs. Such a complex fitting
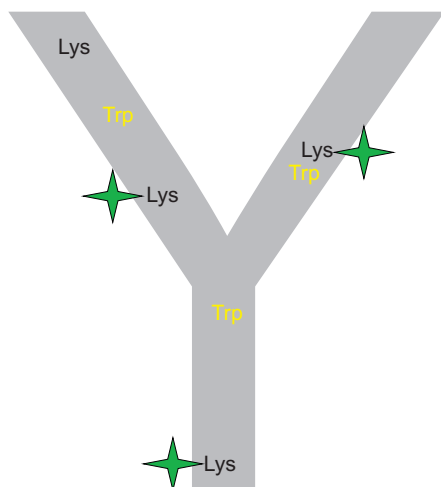
Figure 6.16: Explanation for the double exponential decay of dyes. Dye molecules are conjugated to lysine (Lys) amino-acids. Some of the Lys can be located near tryptophan (Trp) amino-acids, which quench fluorescence. Certain dye moelcules conjugated to the antibody can be quenched by tryptophan and others not.

function was chosen because of the following considerations. Since each sample with AuNPs has two subpopulations, each of them is expected to be quenched by AuNPs in its own way. Dye molecules from both subpopulations can be attached to the same antibody. The intensities A_f, A'_f, A_s and A'_s at time 0 are proportional to the concentrations of molecules in each subpopulation in the free and bound systems. Therefore these parameters should not be independent. The dependence between them can be expressed as $A'_s = P_f A'_f$ and $A'_{sq} = P_f A'_{fq}$. Moreover the sum of all amplitudes $A'_f + A'_s + A'_{fq} + A'_{sq} = I'(0)$ is equal to the fluorescence intensity of the quenched sample at time 0. This allows to use another dependency between the parameters $A'_{fq} = \frac{I'(0)}{1+P_f} - A'_f$. Keeping in mind that in the fitting of the hybrid system τ_f and τ_s stay fixed, the number of fitting parameters in formula 6.1 is reduced from eight to three. The decays for the hybrid system can be fitted with

$$I(t) = A'_f e^{-t/\tau_f} + P_f A'_f e^{-t/\tau_s} + \left[\frac{I'(0)}{1+P_f} - A'_f \right] e^{-t/\tau'_f} + P_f \left[\frac{I'(0)}{1+P_f} - A'_f \right] e^{-t/\tau'_s}, \quad (6.2)$$

where the fit parameters are A'_f, τ'_f and τ'_s; values of $I'(0)$, P_f, τ_f and τ_s are known.

6.6.2 Non-radiative rate and energy transfer

In all systems it can clearly be seen that the lifetime of the dye is significantly decreased when the analyte is present (figures 6.14(a), 6.14(b), 6.15(a) and 6.15(b)). Similarly to the digoxigenin assay from the previous chapter, charge transfer to the AuNP can be excluded here as the dye-AuNP distance is too large. Therefore the energy transfer must be responsible for the lifetime reduction. Energy transfer times and efficiencies can be calculated for fast and slow components of the systems. The energy transfer rate was calculated as $\frac{1}{\tau_{ET}} = \frac{1}{\tau'} - \frac{1}{\tau}$. The results are presented in figures 6.17(a) and 6.17(b). The energy transfer rate is larger for dyes with shorter lifetime within Cy3 and Cy3B subpopulations and between Cy3 and Cy3B.

Energy transfer efficiency for the fast and slow components is calculated as

$$\Phi_{ET} = 1 - \frac{\tau'}{\tau}. \quad (6.3)$$
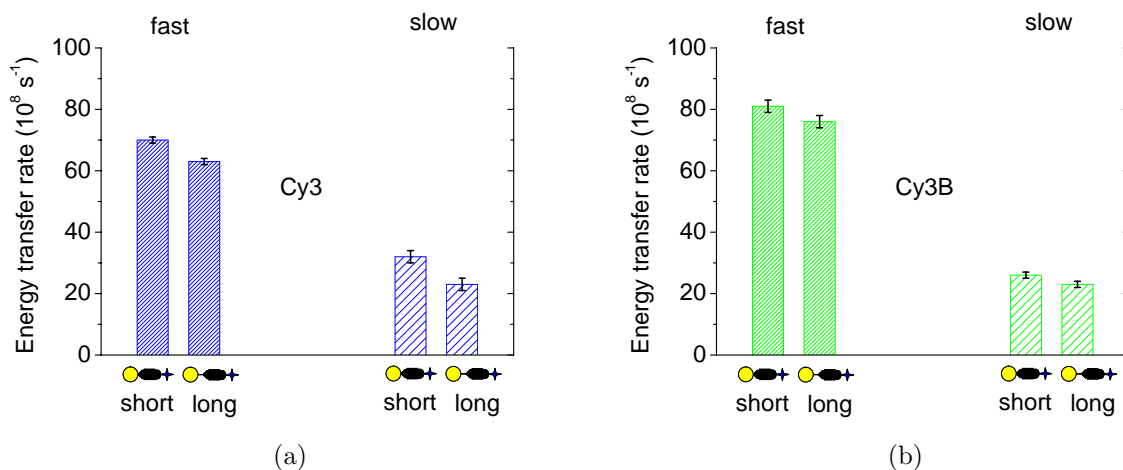
Figure 6.17: Energy transfer rates for the short and long sandwich systems with Cy3 (a) and Cy3B (b) markers. Energy transfer is faster for dyes with shorter lifetimes.

Calculation results are shown in figures 6.18(a) and 6.18(b). Energy transfer is more efficient for dyes with a longer fluorescence lifetime. The efficiencies for the short and long sandwich are practically the same. This means that the average distance from the dye to the AuNP is similar for the short and long sandwiches.
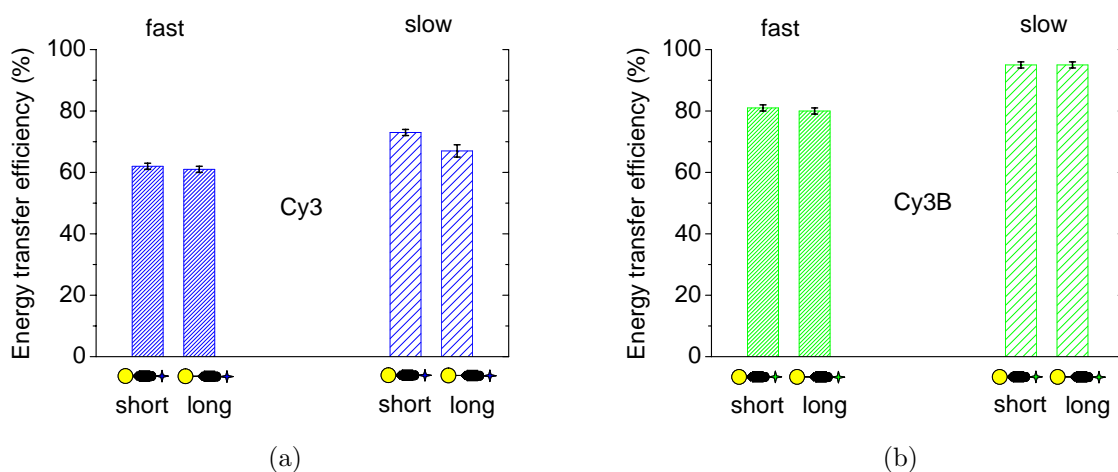
Figure 6.18: Energy transfer efficiencies for the short and long sandwich systems with Cy3 (a) and Cy3B (b) markers. Energy transfer is more efficient for dyes with longer lifetimes.

6.6.3 Radiative rate suppression and enhancement

The intensities of the fluorescence at time 0 have very similar values in the sample and reference for both dyes and for the short and long test formats. For the short and long sandwiches with the Cy3 marker, a slight increase in the fluorescence intensity at time 0 and consequently the radiative rate is observed (figures 6.19(a) and 6.19(b)). The only exception from this trend is the slow component in the short sandwich. The effect is very small, though.

For the Cy3B marker the behavior of the radiative rate in the short and long sandwiches is different (figures 6.20(a) and 6.20(b)). In the short sandwich there is a decrease in the radiative rate for both the fast and slow components. In the long sandwich no change in the radiative rate is observed.

The different trends in the influence of the AuNP on the radiative rate of the dyes can be attributed to several possible factors. First, the difference in the short and long components is related to different positions of these subpopulations on the antibody (figure 6.16). One subpopulation might be oriented in a way that would lead to an enhancement of the radiative rate and the other can have an orientation that leads to a decrease of the radiative rate. Second, the short and long sandwiches are different in the way intact antibodies and F(ab')2

(a)   (b)
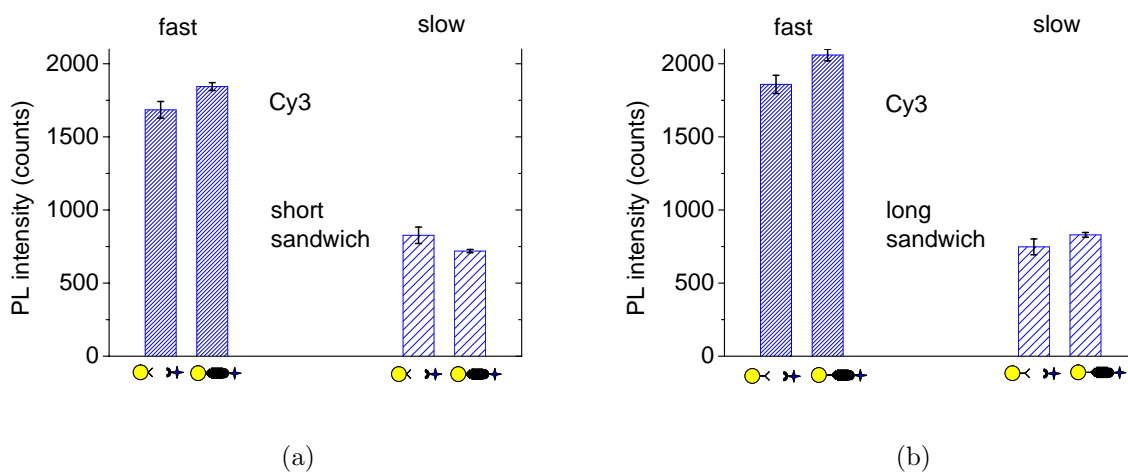
Figure 6.19: Intensities at time 0 for the short (a) and long (b) sandwich. Cy3 is the fluorescent marker. There is an opposite trend in the fast and slow components in the short sandwich. The fast component is enhanced by AuNPs and the slow component is suppressed. A slight increase of the radiative rate in the long sandwich for both fast and slow dye subpopulations is observed.
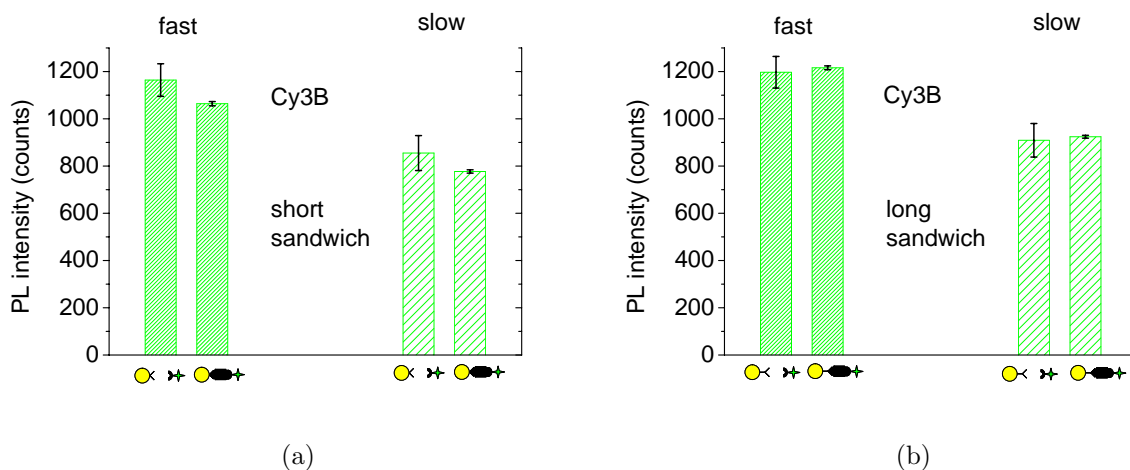
Figure 6.20: Intensities at time 0 for the short (a) and long (b) sandwich. Cy3B is the fluorescent marker. There is a slight decrease of the radiative rate in the short sandwich for both fast and slow dye subpopulations. In the long sandwich the radiative rate stays unchanged.

fragments are oriented on the gold surface. This also influences the orientation of the dye to the AuNP surface.

6.6.4 Percentage of bound dyes

The amount of dye bound to AuNPs can be calculated knowing the initial intensities at time 0 in the reference and in the quenched systems. The amount of bound dye from slow and fast subpopulations is equal to $Bound = \left(1 - \frac{A'}{A}\right)$. Figures 6.21(a) and 6.21(b) show the results of the calculation. There is slightly more bound dye in the long sandwich systems. A possible reason for this is that the number of active paratopes is higher when complete intact antibodies and fragments are used. The percentage of bound dye in most cases is more than 70 % since the measurement is made for a concentration ratio, for which the highest binding is expected. Thus, time resolved spectroscopy is a useful tool to estimate the number of bound sandwiches in FRET-based immunoassays.
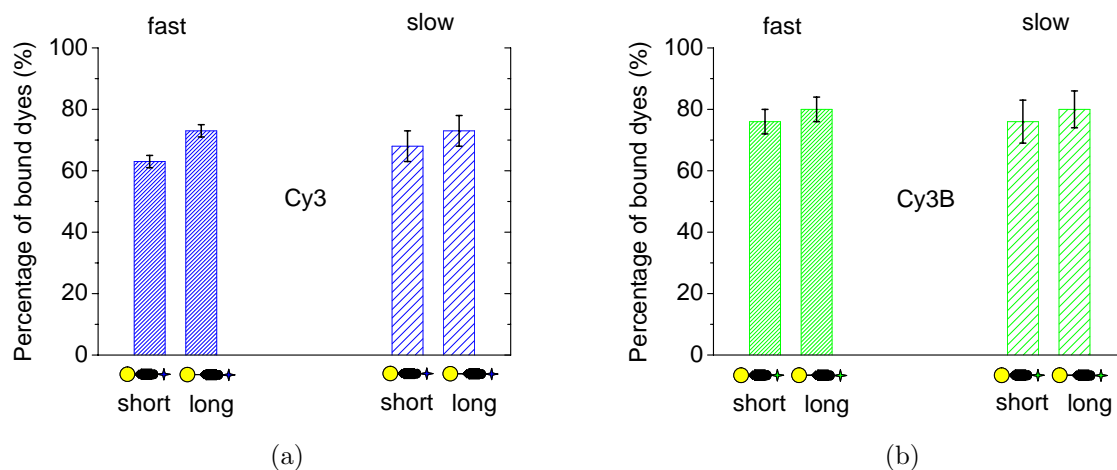
Figure 6.21: Percentage of bound sandwiches with Cy3 (a) and Cy3B (b) markers.

6.7 Conclusion

In this chapter, it was demonstrated that long-range fluorescence quenching by AuNPs can be used to develop a sandwich-type biosensor for cardiac troponin T. This is the first immunoassay of this type. The limit of detection of this immunoassay in buffer is 0.02 nM (corresponding to 0.7 ng/mL) and 0.11 nM (corresponding to 4.0 ng/mL) in serum. The detection limit of the assay in buffer lies within the medically relevant range. The quantification of fluorescence quenching for the sandwich assay does not need a reference sample as in the competitive assay described in the previous chapter.

Computer simulations of the binding of the sandwich were performed and compared with experiments. It was found that an increase of dye concentration with fixed AuNP concentration leads to a broader dynamic range of the assay. Using the experiments and simulations, it was shown that the limit of detection and the dynamic range of the test depend on the concentrations of both the dye and the AuNPs.

Through time resolved measurements, it was shown that a highly efficient energy transfer process is responsible for the quenching. The radiative rate of the dye remains practically unchanged by the AuNP. No significant differences in the quenching mechanism were found with the use of complete intact antibodies or F(ab')2 fragments on AuNPs. This is due to the flexibility of the F(ab')2 fragment, which can extend to the length of the full antibody. Two

fluorescent markers Cy3 and Cy3B were compared. Cy3B with a higher quantum efficiency and longer fluorescence lifetime is quenched stronger than Cy3.

The number of bound and free dye molecules could also be found by conducting time resolved measurements. This is a critical parameter for all homogeneous assays and is normally not accessible through standard steady state experiments. Knowing the number of free molecules can allow an improvement of the assay sensitivity. This is done by tuning the concentrations of the sandwich components in such a way, that a maximal number of fluorescent markers is bound to AuNPs and their fluorescence is quenched. Additionally, the signal-to-noise ratio in the assay can be improved due to the separation of unbound dyes in the data analysis.

7. Energy transfer in clusters of CdTe nanocrystals

Energy transfer can take place from smaller to larger CdTe nanocrystals (NCs) due to the differences in their band gaps and optical properties. Since the synthesis procedures allow NCs with controlled sizes to be made, they offer an advantage of creating structures, where a cascaded energy transfer can be realized. Thus, the excitation energy can be transferred from the smallest to the larger and finally to the largest NCs. Such a structure is an artificial energy harvesting complex, where all energy can be channeled to one part of the system. Controlled clustering of colloidal NCs offers a possibility to design systems with a cascaded energy transfer. Different methods can be used in order to bring donor and acceptor NCs in the vicinity of each other in clusters. This chapter describes three approaches to create artificial energy harvesting complexes from CdTe nanocrystals. First, Ca^{2+} ions can be used to couple negatively charged NCs. Second, covalent binding of donor and acceptor NCs through short dithiol linkers is feasible. Third, covalent binding of NCs by thiolated DNA is an option.

7.1 Cluster formation through Ca^{2+} ions

The surface of CdTe NCs is capped with molecules of thioglycolic acid (TGA). This creates a negative charge on the outer surfaces of the NCs because of the $-COO^-$ groups. This fact allows electrostatic coupling of NCs. A coupling agent with a multiple positive charge could be used for this purpose. Metal ions are good candidates for this. Their small size enables the NCs to be brought very close to each other, to a distance where energy transfer can occur. An investigation of the influence of different metal ions on the optical properties of CdTe NCs was published by Susha et al. [121]. In this publication the authors demonstrated that ions such as Ag^+, Fe^{3+}, Hg^{2+} lead to a strong quenching of CdTe fluorescence. The effect of Ca^{2+} ions on the PL of the NCs was less dramatic. Therefore, Ca^{2+} was chosen as a cross-linking agent for this work (figure 7.1).

In the absence of Ca^{2+}, the zeta potential of CdTe NCs in solution was -37 mV. With a Ca^{2+} concentration of $2 \cdot 10^{-4}$ M it was -15 mV. This means that Ca^{2+} ions neutralize the particles, which would have a higher charge and repel each other without Ca^{2+}.
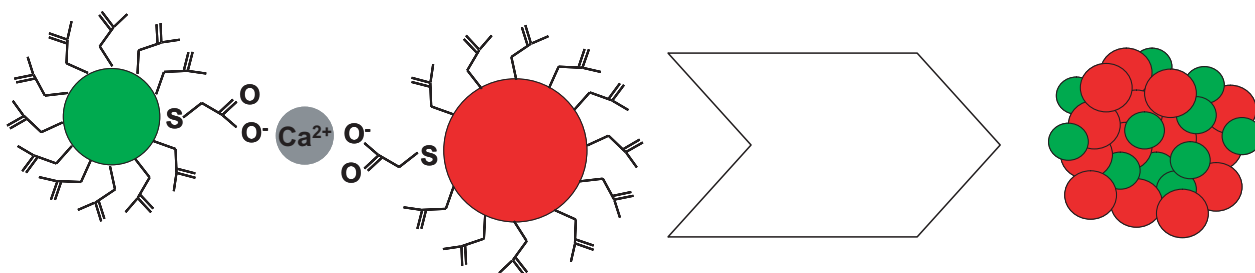
Figure 7.1: Scheme of cluster formation of TGA-capped CdTe NCs by Ca^{2+} ions. Positively charged ions bind together the NCs having negative charge on the surface.

In order to study the effect of Ca^{2+} ions on the fluorescence of NCs of one size, $CaCl_2$ was added to a solution of purely green emitting NCs (figure 7.2(a)).[1] For simplicity, solutions with green, red and mixed green and red NCs will be denoted as G, R and GR. Two peculiar effects upon Ca^{2+} addition can be seen (fig. 7.2(a)).

First, there is a clear red shift of the PL peak with an increase of Ca^{2+} ion concentration. Since nanocrystals in the green fraction are not all of the same size and therefore have

---

[1]Data presented in this chapter were produced by the author and are attributed to the American Chemical Society since the copyright on several published graphs belongs to the journal.
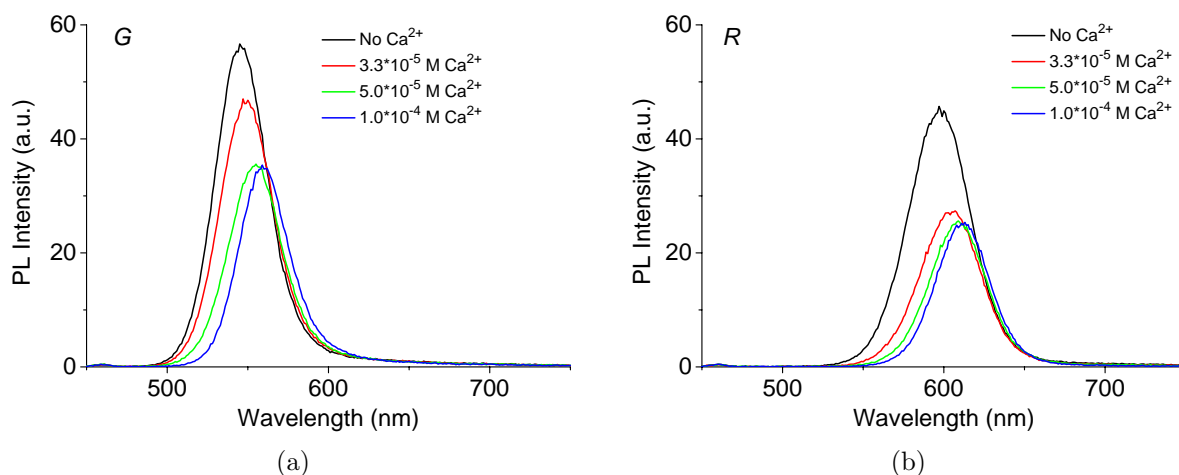
Figure 7.2: Effect of increasing Ca^{2+} ion concentration on the photoluminescence of green (a) and red (b) NCs. A red shift of the emission peak can be seen for green and red NCs as the Ca^{2+} concentration is increased. This is due to the energy transfer from the smallest to the largest NCs within the fraction. Reprinted with permission from [123]. Copyright 2008 American Chemical Society.

somewhat different absorption and emission spectra, the smaller ones can act as donors and larger ones as acceptors. The energy transfer will result in quenching of the fluorescence of the greener and smaller donors and enhancement of the fluorescence of the redder and larger acceptors. The red shift can be seen in the emission spectrum upon Ca^{2+} addition because the fluorescence intensity of greener NCs is decreased and of red NCs increased. This effect was also observed in other publications [27, 122].

Second, a general decrease in the PL intensity is observed. In an ensemble, a certain fraction of NCs does not emit light [124], but is able to absorb it. If energy is transferred to these "dark" NCs, then the total luminescence of the sample decreases. The existence of "dark" NCs is explained by the presence of surface defects in them, which is inherent to the growth process of NCs during the synthesis [125]. Additionally, it was observed for CdSe and CdTe NCs that their total PL intensity is significantly decreased when clustering or formation of solid films takes place [126, 127]. This should happen in the discussed system as well. Similar effects can be observed when Ca^{2+} ions are added to purely red NCs (figure 7.2(b)).

When Ca^{2+} ions are added to the mixture of the green and red NCs, the PL intensity of green NCs decreases and of red NCs increases (figure 7.3). This is an indication of energy
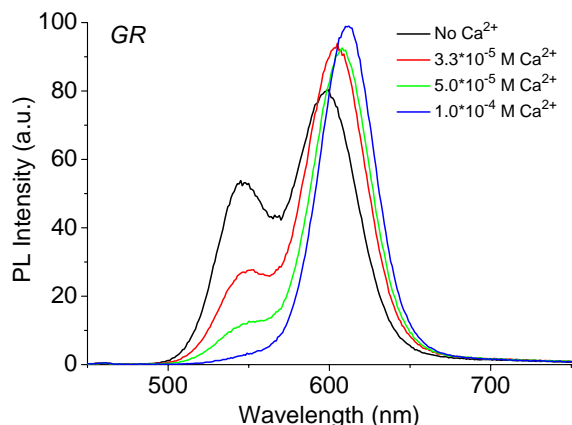
Figure 7.3: The PL intensity of green NCs decreases and the PL intensity of red NCs increases when Ca^{2+} is higher. Reprinted with permission from [123]. Copyright 2008 American Chemical Society.

transfer from green NCs to the red ones. In the figures 7.2(a) and 7.2(b) it is clear that the addition of Ca^{2+} ions leads to the decrease of the fluorescence intensities of both green and red NCs. It is expected, that such a decrease would also take place in the mixture of the green and red NCs. However, one can see a clear increase in the fluorescence intensity of red NCs (figure 7.3). This means that energy transfer overrides the quenching of fluorescence caused by the mere presence of Ca^{2+} ions. This fact makes the observed enhancement of the red NC emission more dramatic than it can be assumed from the spectrum. The efficiency of energy transfer cannot be calculated reliably because the two effects seen in figure 7.3, quenching by Ca^{2+} ions and enhancement of red NCs due to energy transfer from the green NCs, cannot be clearly separated from each other.

A common feature accompanying NC cluster formation is enhanced scattering seen in the extinction spectra [27]. Measurements show that such an increase takes place only at rather high Ca^{2+} concentrations of $5 \cdot 10^{-4}$ M (magenta curve in figure 7.4). From dynamic light scattering experiments, it was determined that cluster size was 60 - 130 nm in diameter. The clusters that formed were stable in terms of their size within the time needed to perform
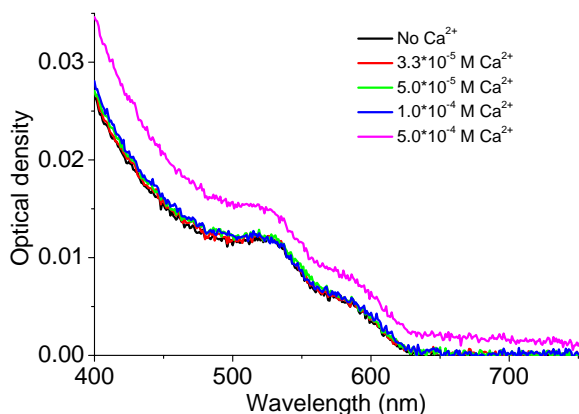
Figure 7.4: Effect of increasing Ca^{2+} ion concentration on the extinction spectrum of the mixture of green and red NCs. Only when the Ca^{2+} ion concentration reaches $5 \cdot 10^{-4}$ M, the solution shows stronger scattering, which indicates that large clusters are formed.

a measurement. However, if a Ca^{2+} ion concentration over $5 \cdot 10^{-4}$ M was taken, light scattering measurements showed the formation of aggregates of several hundred nanometers, which became micrometer-sized within 30 min. This explains the change in the absorption in figure 7.4 (magenta curve). It has to be noted that the processes of cluster formation described above are highly dynamic and large aggregate formation can happen also at low Ca^{2+} ion concentration if enough time is allowed.

7.1.1 Control experiments

In order to investigate the role of Ca^{2+} in cluster formation, Ca^{2+} replacement experiments were performed. When Na$_2$CO$_3$ is added to the system containing $5.0 \cdot 10^{-4}$ nM Ca^{2+} ions, CO$_3^{2-}$ ions bound the Ca^{2+} ions holding the clusters together into calcium carbonate

$$Ca^{2+} + Na_2CO_3 \rightarrow 2Na^+ + CaCO_3 \downarrow .$$
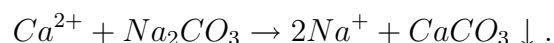
Since Na$^+$ has only a single charge it fails to bind two NCs simultaneously. The result is that the donor luminescence previously quenched by the acceptor partially recovers, and the acceptor PL intensity decreases because the donors, which transferred energy to the acceptors are not in the vicinity anymore (figure 7.5). When the aggregates of CdTe NCs achieved a critically large size, the addition of sodium carbonate did not affect them anymore. This is because Ca^{2+} ions deep in the cluster were not accessible and thus replaceable.

CdTe NCs with positively charged cysteamine ligands were exposed to Ca^{2+} ions. The PL of the green NCs stayed unaffected (figure 7.6(a)). A slight increase in fluorescence intensity
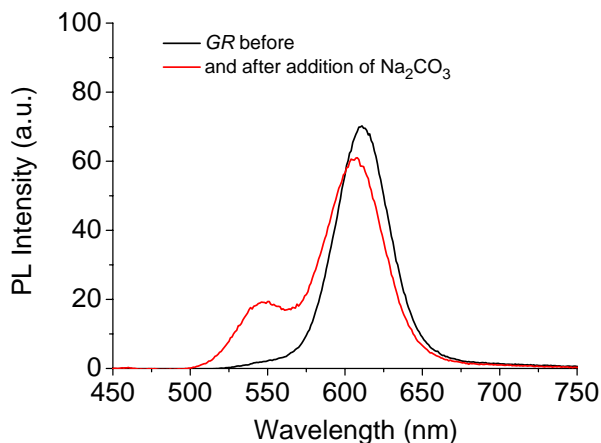
Figure 7.5: When Na$_2$CO$_3$ is added to the clustered solution, the green NCs' fluorescence recovers and the PL intensity of the red NCs decreases. Single valent Na$^+$ ions replace the double valent Ca^{2+}, so the clusters are destroyed and no energy transfer is taking place. Reprinted with permission from [123]. Copyright 2008 American Chemical Society.
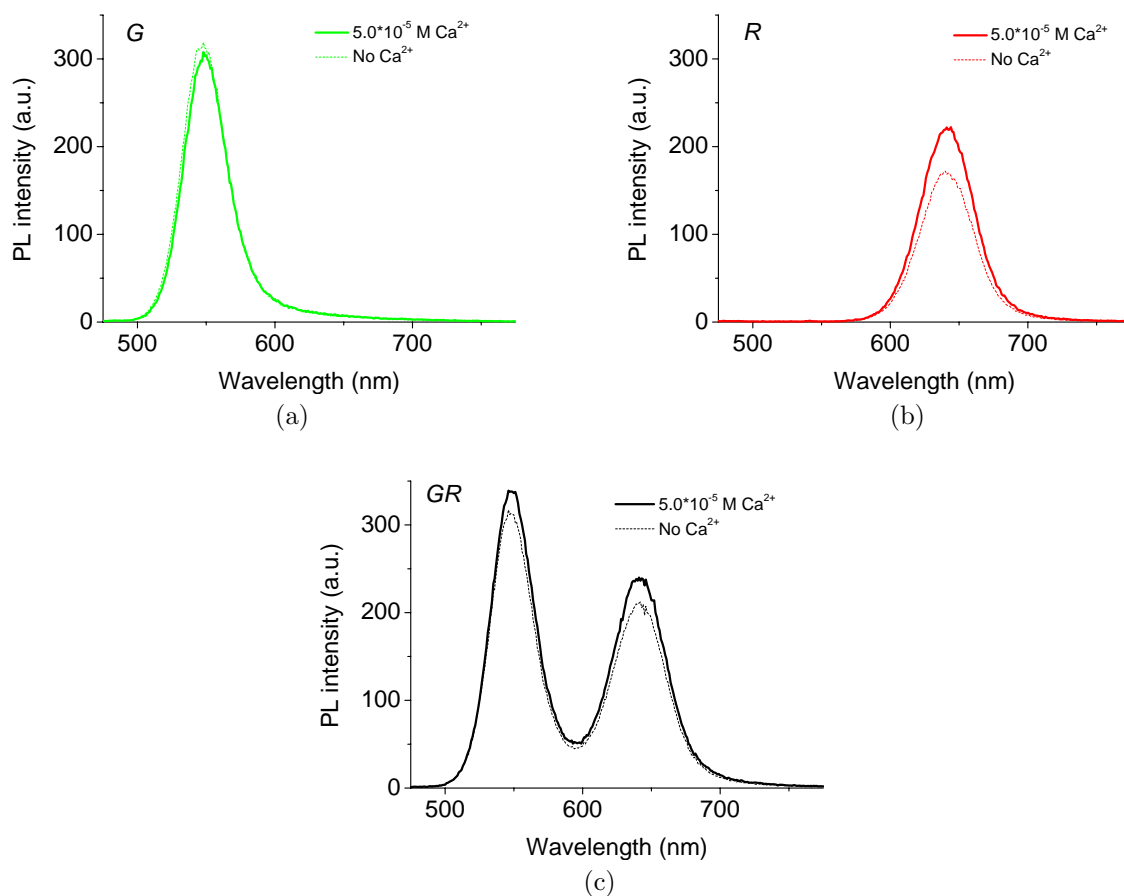
Figure 7.6: Effect of Ca^{2+} ions on the photoluminescence of cysteamine-stabilized green (a), red (b) and mixed green and red (c) NCs.

could be observed for the red NCs and for the green-red mixture upon the addition of Ca^{2+} ions (figures 7.6(b) and 7.6(c)). This means that in the applied concentration range Ca^{2+} ions as such do not significantly quench the fluorescence.

7.1.2 Fluorescence decay of energy donors and acceptors

Time-resolved measurements were performed in order to clarify the processes taking place in the system under investigation. When the PL decay of pure green and pure red NCs at their PL peaks (550 and 600 nm) are considered (figures 7.7(a) and 7.7(c)), it can be seen that in both cases a shortening of the lifetime upon increasing Ca^{2+} concentration is observed. This is consistent with the red shift observed in figures 7.2(a) and 7.2(b) and indicates that

NCs emitting at the wavelength of the peak transfer their energy to those in the red wing of the spectrum, which is accompanied by the donor fluorescence lifetime decrease typical for FRET.

In the green-red NC mixture measured at 550 nm (figure 7.7(b)) one can see a faster fluorescence decay upon increasing Ca^{2+} concentration than in the case of purely green NCs (figure 7.7(a)). This is due to the fact that for the green donors there are more available donors in the green-red mixture because not only the largest green NCs, but also all red NCs can be energy acceptors in this system.

Comparing the fluorescence decay of pure red NCs and of the green-red mixture measured at 600 nm (the peak of red emission), one can see that the mixture has a longer fluorescence lifetime (figure 7.7(d)). In the mixture the NCs emitting at 600 nm play a role not only of donors to the further red NCs as in the pure red NC case (green curve), but also are acceptors for all green NCs. Therefore, they are energetically fed by the green NCs during their fluorescence lifetime.

The effect of energetic feeding can be seen even more clearly when the PL lifetimes are recorded in the red wing of the acceptor fluorescence at 635 nm. This spectral position corresponds to the largest red NCs, which can only play a role of energy acceptors. When Ca^{2+} is added to purely red NCs (figure 7.7(e)) the rise time of fluorescence becomes slower for increasing Ca^{2+} concentration. In the green-red mixture the feeding of the largest NCs is even stronger because in this case all NCs in the cluster are donors for the largest NCs (figure 7.7(f)).

An additional interesting effect can be observed from these measurements. The drop of fluorescence of donors takes place within just one or two ns (figures 7.7(a) and 7.7(b)), but the energetic feeding extends over several ns (figures 7.7(d) and 7.7(f)). As mentioned before, there can be some "dark" NCs in the cluster, which do not emit light upon laser excitation. This effect is attributed to trapped excitons, which reside in long-living states. It was reported that energy transfer is possible from these trap states to the neighboring NCs [127]. This is displayed in the enhanced emission of the acceptor. This effect came to be known as trapped exciton recycling. This process can explain the inconsistency in the time constants of the donor lifetime shortening and the acceptor feeding.
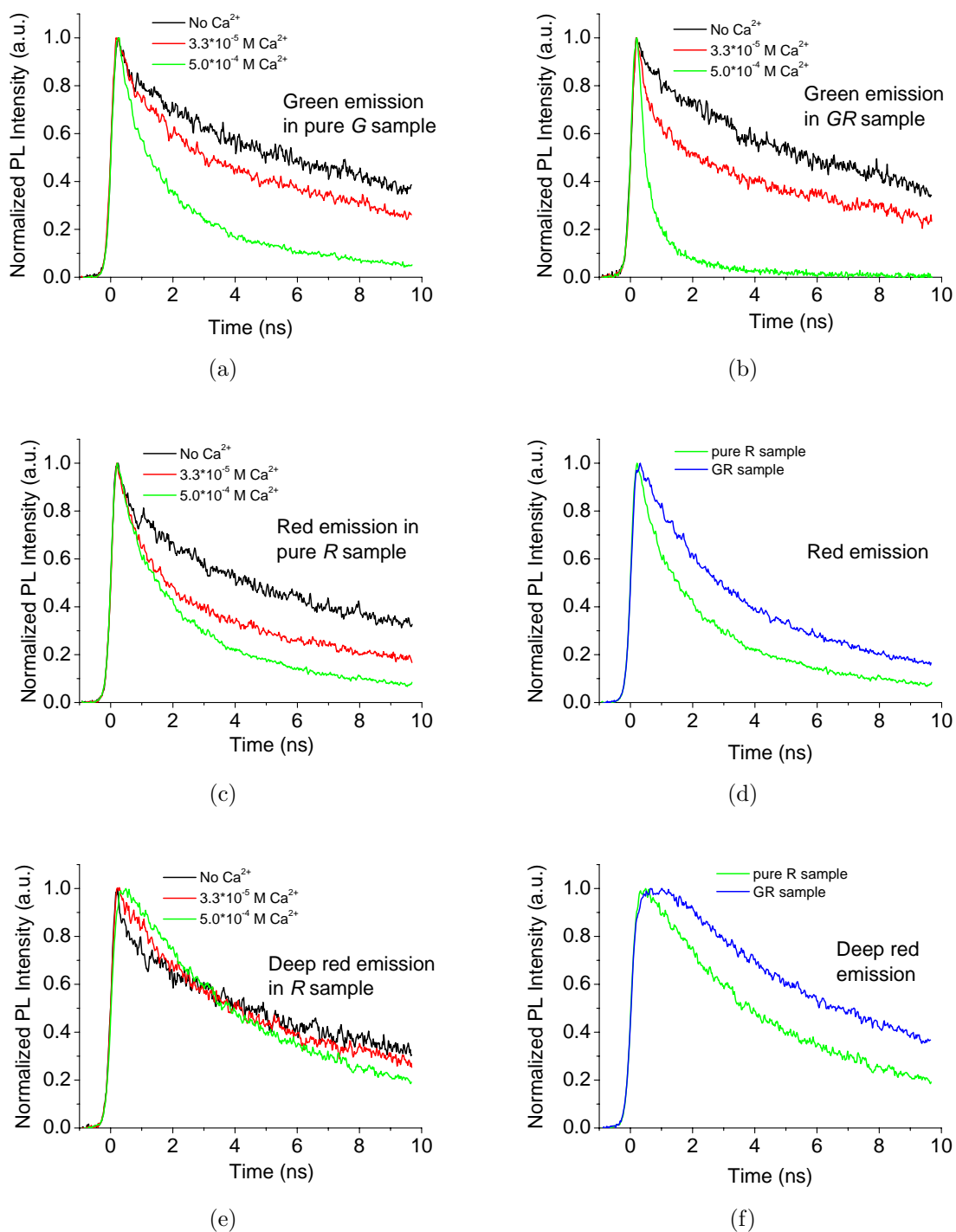
Figure 7.7: Time resolved measurements of G, R and GR systems measured at 550 nm (a, b), 600 nm (c, d) and 635 nm (e, f). Ca^{2+} ion concentration in figures d and f was $5 \cdot 10^{-4}$ M. Reprinted with permission from [123]. Copyright 2008 American Chemical Society.

The fluorescence decay of colloidal NCs is typically non-monoexponential [68]. This makes the exact fitting and calculation of energy transfer rates in this system difficult.

7.1.3   Variation of the donor-acceptor ratio

Table 7.1: Relative PL intensities of the red and green emission peaks with different G/R ratios.

	relative PL (%)	
G/R ratio	green	red
unmixed	100.0	100.0
1.7:1	6.5	108.5
3.4:1	9.0	129.6
6.8:1	13.0	176.9

The donor-acceptor ratio in the aggregate is important for optimizing the energetic feeding of the acceptor NCs. Ratios of green to red NC concentrations of 1.7:1, 3.4:1 and 6.8:1 were studied (figure 7.8 and table 7.1). An increase in green NC PL intensity and constancy of red NC PL emission can be observed when more donors per acceptor are taken and no Ca^{2+} is present in the solution. As soon as $1.0 \cdot 10^{-4}$ M of Ca^{2+} is added to these solutions the dramatic reverse of the previous situation is observed. In the case of the largest donor-acceptor ratio of 6.8:1 the PL intensity of green NCs dropped by 87 %, whereas the PL intensity of the red NCs increased by 77 % (table 7.1). Time-resolved data also support these findings. When there are more donors per acceptor, the fluorescence decay of the donor
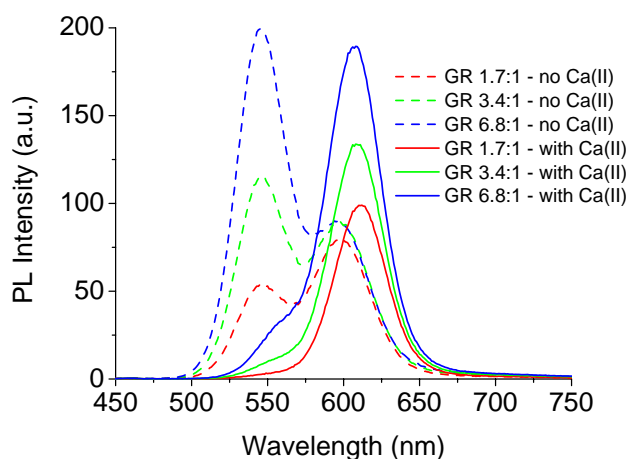
Figure 7.8: GR mixtures with different donor-acceptor ratios. Upon increasing the number of donors per acceptor, the acceptor luminescence increases and the donor fluorescence becomes quenched. The concentration of Ca^{2+} ions was $1.0 \cdot 10^{-4}$ nM. Reprinted with permission from [123]. Copyright 2008 American Chemical Society.
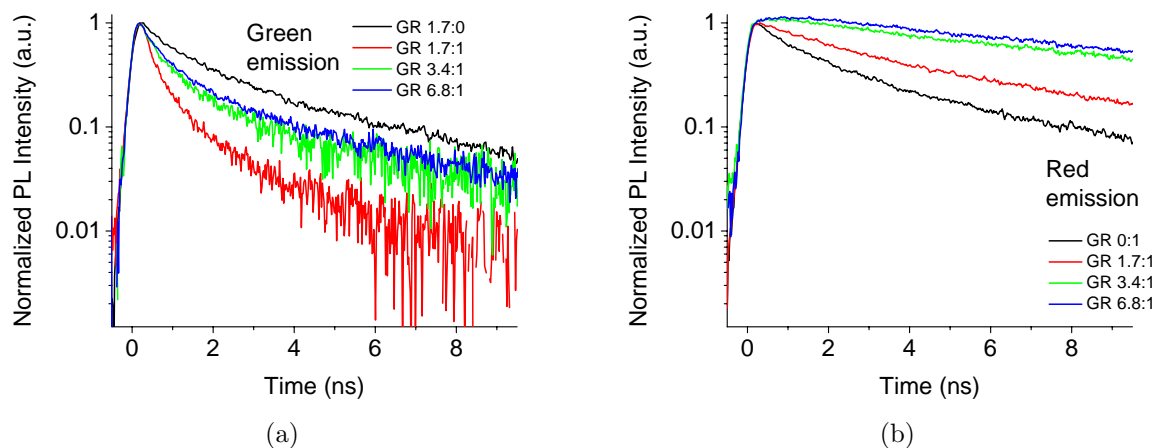
Figure 7.9: Fluorescence decay of the GR mixture with different donor-acceptor ratios. (a) When there are more donors per acceptor, the fluorescence decay of the donor becomes slower and thus closer to the case of free donors. (b) Energetic feeding of the acceptor with increasing number of donors can be seen from the slower acceptor decays with increasing donor-acceptor ratio. The concentration of Ca^{2+} ions was $1.0 \cdot 10^{-4}$ nM. Reprinted with permission from [123]. Copyright 2008 American Chemical Society.

becomes slower and thus closer to the case of free donors (figures 7.9(a)). Energetic feeding of the acceptor upon increasing number of donors can be seen from the slower acceptor decays (figure 7.9(b)).

7.1.4 Stepwise FRET with three different sizes of nanocrystals

Finally, a mixture of nanocrystals of three different sizes was prepared. It consisted of red, green and near infrared (NIR) emitting NCs. Small concentrations of Ca^{2+} ions did not affect the PL spectra of the mixture within about 20 min after the addition of Ca^{2+}. When the Ca^{2+} ion concentration was $6.7 \cdot 10^{-5}$ M, the intensities of G and R NCs started to decrease and the PL intensity of NIR NCs rose (figure 7.10(a)). Gaussian fits of separate emission peaks and their integration clarifies the effect (figure 7.10(b)). At the highest added Ca^{2+} concentration of $5.0 \cdot 10^{-4}$ M the green emission fell to 4 % of its original value, red emission decreased to 22 % and NIR NC PL intensity went up 40 % from the value without Ca^{2+}.

In the case of the ternary system, additional pathways for energy transfer are opened. Here, the NIR NCs have their absorption and emission in the foremost red part of the
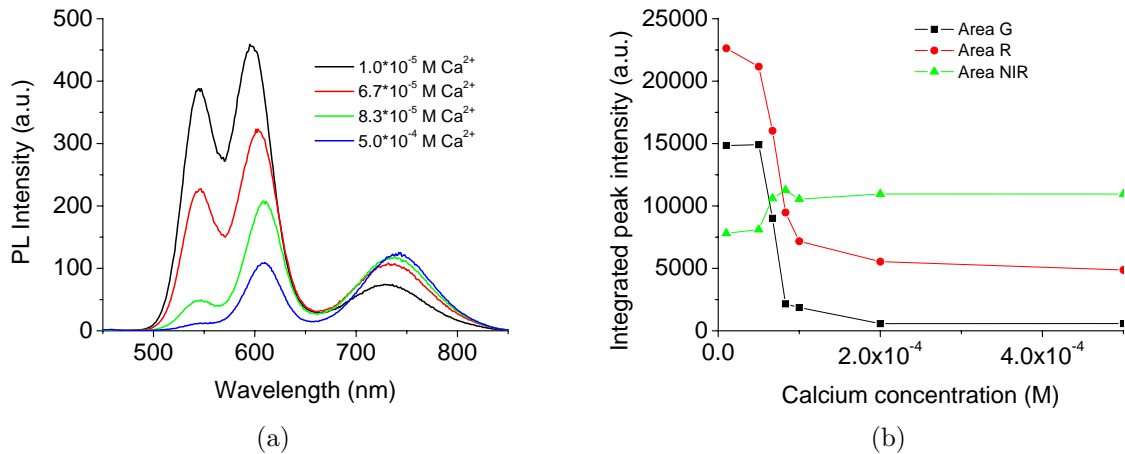
Figure 7.10: Mixture of three different sizes of NCs: green, red and near infrared. (a) When the Ca^{2+} ion concentration is increased, PL intensities of green and red NCs decrease because both can be donors for NIR NCs. The luminescence of NIR NCs increases because they are energy acceptors. (b) Integrated spectra of green, red and NIR NCs. Spectra of separate NCs were approximated with Gaussian functions. This plot clarifies the decrease of G and R PL intensities and the increase of NIR NCs with growing Ca^{2+} ion concentration. Reprinted with permission from [123]. Copyright 2008 American Chemical Society.

spectrum and can accept energy from both green and red NCs. Förster radii for three donor-acceptor pairs in this mixture can be estimated from the steady state PL $I_D(\lambda)$ and absorption $\varepsilon_A(\lambda)$ spectra of the corresponding NCs using the formula

$$R_0^6 = \frac{9000(\ln 10)\kappa^2 Q_D}{128\pi^5 N_A n^4} \int_0^\infty I_D(\lambda)\varepsilon_A(\lambda)\lambda^4 d\lambda. \tag{7.1}$$

knowing the quantum efficiency Q_D of the pure donor and considering the random orientation of the donor and acceptor transition dipole moments to each other.

The resulting values of 6.3 nm for the green-red, 7.6 nm for the green-NIR and 8.2 nm for the red-NIR NC pairs are consistent with numbers reported in literature [128].

7.2   Covalent binding of nanocrystals through dithiols
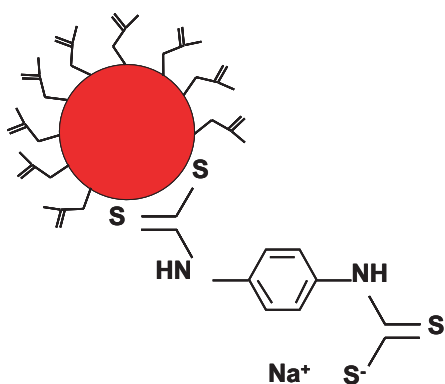
Figure 7.11: CdTe NC partially stabilized by PBDT.

A second approach to create clusters of CdTe NCs with more control over structures is the covalent binding of NCs through covalent thiol bonds. It has been previously demonstrated that dithiol molecules can be used to cross-link CdTe NCs into small aggregates composed of NCs of nominally the same size [129, 130].

CdTe NCs were taken, where part of the stabilizer molecules on the surface were disodium 1,4 - phenylene-bis (dithiocarbamate) (PBDT) instead of TGA (figure 7.11). PBDT molecules have two thiol groups on both ends. One end is connected to the NC surface. The other end can be utilized to chemically bind to another NC.

Large red emitting NCs, which are potential acceptors, had PBDT molecules on their surface. Smaller green NCs-donors were stabilized only by TGA without PBDT, whereas TGA is partially removed in order to make the NC surface available for covalent bonding (figure 7.12). In this approach it is desirable to have an excess of donors in the reaction so that they can connect to all available thiol groups on the surface of the acceptor NC.
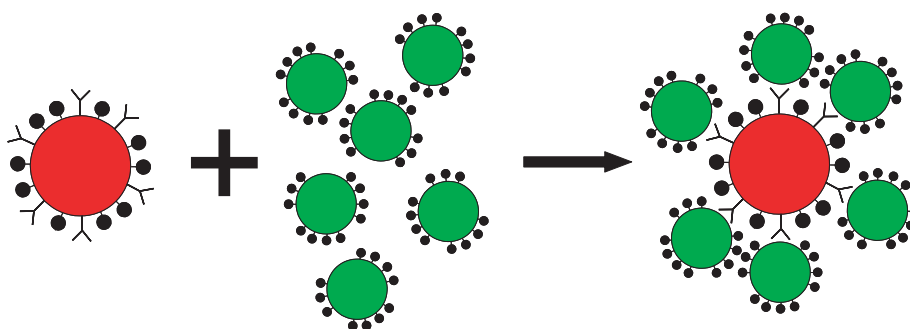
Figure 7.12: Scheme of cluster formation by covalent bonding of CdTe NCs through PBDT.

Figures 7.13(a) and 7.13(b) show how the fluorescence intensity of the donor, acceptor and their mixture develop with time. The emission of pure donor and pure acceptor in the same concentration as in the mixture was monitored in order to see the magnitude of the

(a)

(b)
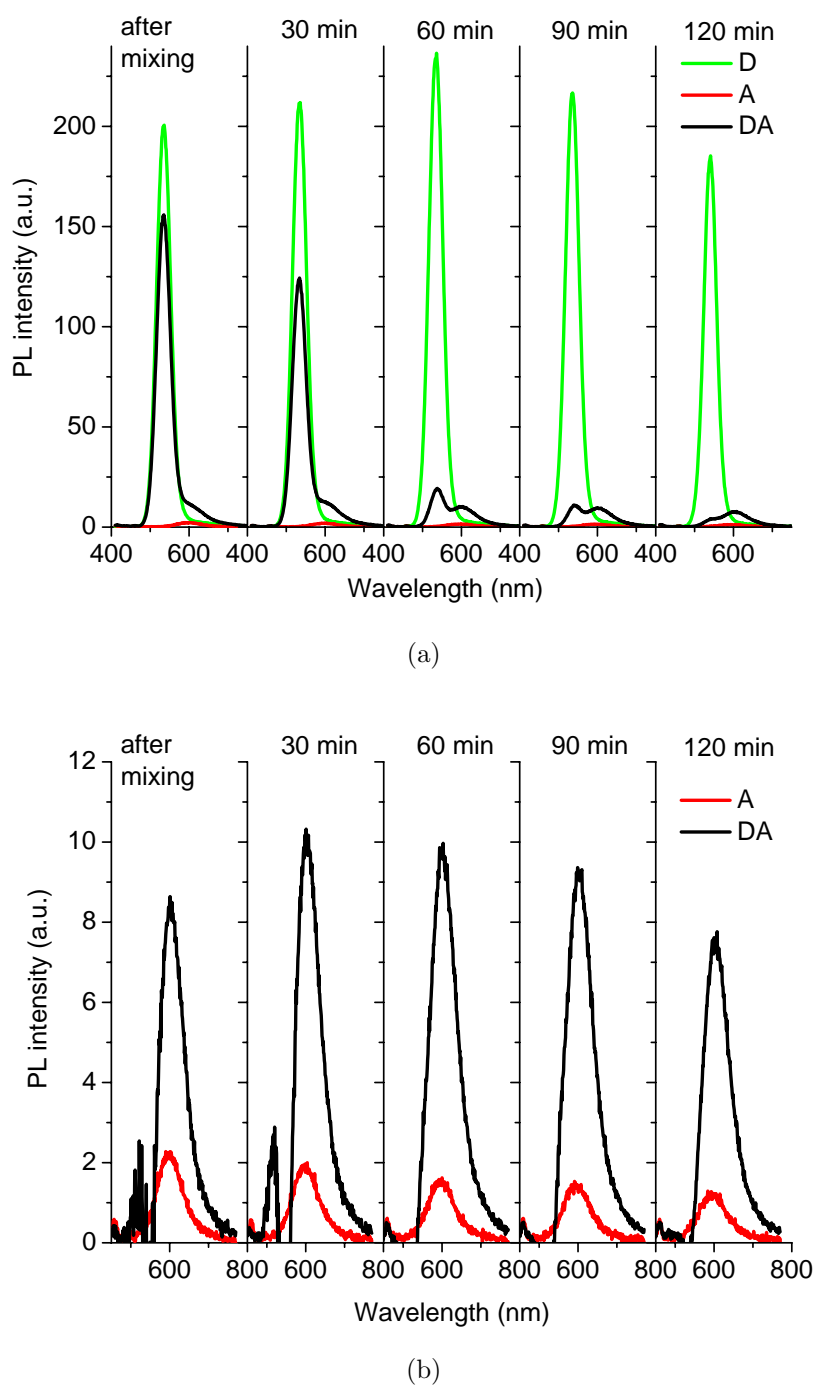
Figure 7.13: Steady state emission spectra of separate donors (green curves), acceptors (red curves) and their mixture (black curves) measured at different time periods after mixing. Donor fluorescence is subtracted from the graph of the donor-acceptor mixture (black curve) in the frame (b).

real effect.

Several observations can be made from these measurements. One notices small fluctuations in time in the pure donor intensity. The intensity of the pure acceptor slightly decreases after 120 min. In the donor-acceptor mixture the donor luminescence decreases 46 times, while the acceptor fluorescence intensity increases 6 times after 120 min. The unsymmetrical change in the donor and acceptor fluorescence intensities can be attributed to a low quantum yield of the acceptor, which is enhanced by the donor to the highest possible value. Further excitation results only in a non-radiative decay of the acceptor. These observations are consistent with the energy transfer picture.

(a)

(b)
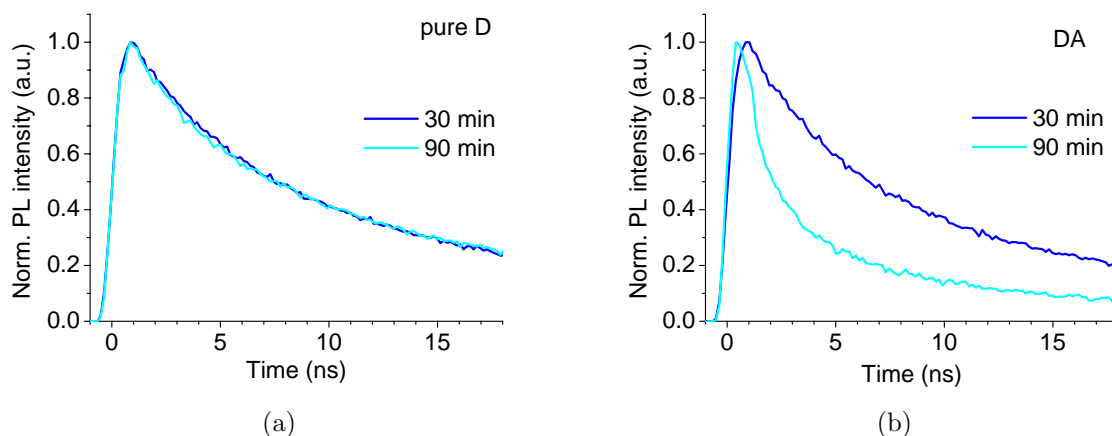
Figure 7.14: (a) Pure donor has very similar fluorescence decays within 90 min. (b) Lifetime of the donor in the donor-acceptor mixture is shortened after 90 min.

PBDT was reported in literature to have a high conductivity [131]. Therefore, a possible mechanism of strong donor quenching could be charge transfer. In order to clarify the photophysical processes in this system, time-resolved measurements were performed 30 and 90 min after donor and acceptor mixing. Figure 7.14(a) shows that the pure donor fluorescence decay does not change within 90 min. On the contrary, the lifetime of the donor fluorescence in the donor-acceptor mixture is shortened. This behavior in the donor fluorescence is typical for energy transfer, but also for charge transfer. Therefore, based on these measurement charge transfer from the donor cannot be ruled out. Charge transfer to PBDT might be responsible for the strong donor quenching seen in steady state measurements, but additionally energy

transfer to the acceptor NCs must be taking place since the increase in their PL intensity is significant. PBDT is chemically bound to the acceptor through a dithiol bond. One of the electrons on a sulphur atom can be delocalized and together with the aromatic ring of the PBDT molecule could transfer the electron from the excited donor NC. Final clarification of the relative importance of charge and energy transfer in this system needs further investigations.

7.3 Coupling nanocrystals by thiolated DNA
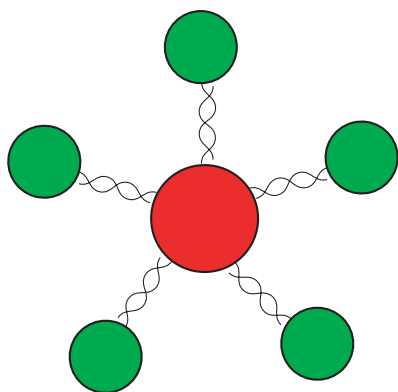
Figure 7.15: Artificial light harvesting complex composed of differently sized NCs connected by DNA.

DNA is a strong candidate to link NCs together because of its property of complimentarity and since the linker length between NCs can be controlled by changing the number of base pairs in the DNA. Such structures could allow the design of artificial photonic wires [132, 133] and transfer energy from one end of the wire to another by FRET from smaller to larger NCs.

The initial approach taken for NC-DNA conjugation was to partially remove the capping molecules from the surface of NCs and to attach thiolated DNA covalently to the free NC surface through the sulfur bond. The proposed advantage of such an approach in comparison to the existing methods of DNA conjugation to the capping molecules is that in case of successful implementation it would allow to make short distances between the NCs. Since FRET is a very distance sensitive process, short donor-acceptor distances are needed for efficient transfer of energy.

Many different formats and approaches to the realization of this idea were tested. Variations in DNA configuration and sequence, NC-DNA binding chemistry, solvent composition and reaction temperature were performed.

It was found that energy transfer happens between NCs connected by complementary and also by non-complementary DNA (figure 7.16(a) and 7.16(b)). This is an indication that nonspecific interactions between the DNA and CdTe NCs dominated over the expected
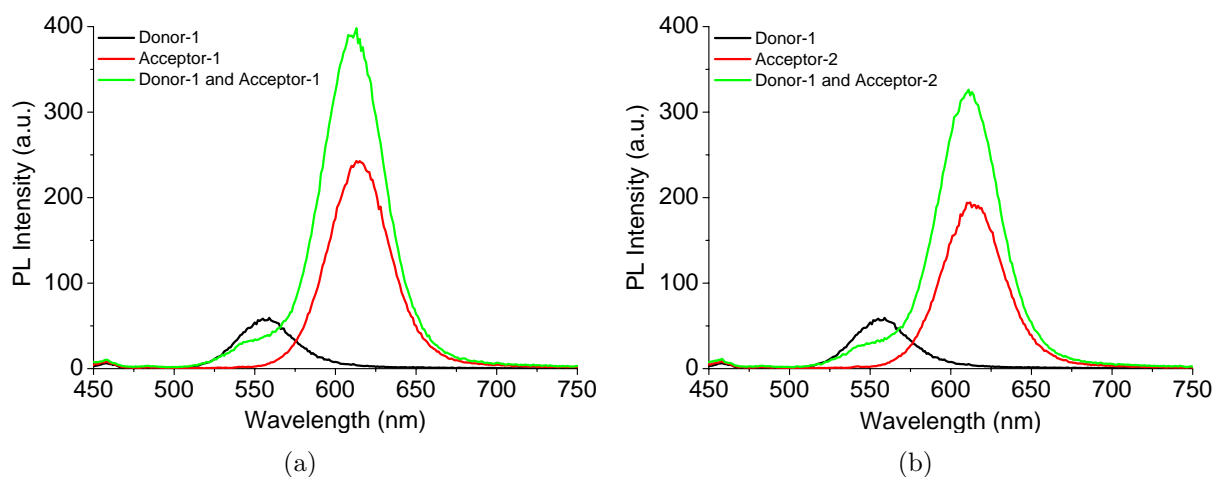
Figure 7.16: Energy transfer in CdTe clusters assembled through DNA can be observed both in the complimentary (a) and non-complimentary (b) case.

specific thiol bonding of DNA. It was described in the literature [134, 135] that nucleic acids can interact with Cd in several ways: through the anionic oxygen atoms present in the phosphate groups, through the hydroxyl groups of the ribose sugars, and through nitrogen atoms of purine and pyrimidine bases. This provides reasons for nonspecific interactions of DNA with the surface of CdTe. Furthermore, in recent electrochemical studies it was shown that DNA might bind to CdTe NCs with its major groove [136]. Non-specific adsorption of DNA was shown to take place also on mercaptoacetic acid-stabilized CdSe/ZnS NCs [95, 137]. One successful approach to functionalize CdTe with DNA was shown recently [138]. It involves a different strategy from that used in this thesis: simultaneous synthesis of CdTe and DNA functionalization.

There are reports on successful conjugation of DNA with CdSe NCs through thiol bonds. Mitchell et al. were the first to connect thiolated DNA to CdSe [139]. Zhou et al., Gill et al. and Wu et al. demonstrated that CdSe/ZnS NCs could be functionalized with DNA and that energy transfer from NCs to organic dye molecules could be observed [140–142]. Medintz et al. reported on a peptidic linker between thiolated DNA and CdSe/ZnS NCs [143]. In a recent publication by Zhou et al. it was shown that the use of a tri(ethylenglycol) linker on CdSe/ZnS NCs could reduce the nonspecific adsorption of DNA on the NC surface [144]. Therefore, CdSe/ZnS NCs are more promising than CdTe for covalent binding of DNA to

the NC surface.

7.4 Conclusion

Ca^{2+} ions were shown to induce CdTe NC clustering. It was demonstrated that multivalent ions lead to aggregation of oppositely charged CdTe NCs. The process of clustering by Ca^{2+} ions can be reversed by the addition of sodium carbonate. Energy transfer from smaller to larger NCs takes place. Through the variation of the donor-acceptor ratios, energetic feeding of acceptors in clusters was optimized. Cascaded energy transfer from the smallest particles to the largest NCs with two and three different sizes was demonstrated. With the help of time-resolved measurements, a shortening of the lifetime of donor NCs and energetic feeding of acceptor NCs was shown. This is the behavior characteristic of energy transfer. Exciton recycling is found to take place in the clusters.

Energy and charge transfer were demonstrated in CdTe NC clusters that are formed by covalent binding of nanoparticles through PBDT molecules. The process of cluster formation and changes in the PL intensities of the components are very dynamic in this system within 120 min after donor and acceptor mixing. These clusters offer a potential advantage of control over the structures. It would be interesting to make TEM measurements of the formed clusters in the future to check how donors arrange around the acceptors.

Finally, it was demonstrated that thiolated DNA can bind NCs together. Energy transfer between the NCs of different sizes took place for the case of complimentary and non-complimentary DNA linkers. The expected selectivity and control over the assembly could not be achieved because DNA appears to interact non-specifically with the surface of NCs.

8. Multi-shell CdSe/ZnS/CdSe/ZnS nanocrystals

In the previous chapter energy was shown to be transferred from small to large nanocrystals (NCs) in clusters. The ideal configuration for collecting energy would be to create onion-like structures, where one acceptor is surrounded by many donors. This situation can be realized within one NC consisting of several shells around the core. Multi-shell CdSe/ZnS/CdSe/ZnS offer such a possibility. Here, energy can be transfered from the outer CdSe shell to the CdSe core. For this to happen, the thicknesses of the CdSe and ZnS shells need to be designed properly. Changing the thicknesses of the shells can also allow to match core and shell emission wavelength in a way that NCs with unique spectral signatures can be created. These structures can have a number of practical applications.

8.1 Onion-like nanocrystals

Heterostructured nanocrystals have recently at-
tracted significant research interest [145]. It has be-
come possible to synthesize NCs composed of several
materials.

Onion-like nanocrystals are composed of two
materials (figure 8.1). Here, a spherical CdSe core is
covered by a ZnS shell. Another CdSe shell is grown
over the ZnS shell. Finally a ZnS layer covers the
whole NC. CdSe NCs can emit light in the visible
range, ZnS layers are used for surface passivation of
CdSe to improve its emission properties. The band
structure of multi-shell NCs shows that charge car-
riers can be localized both in the CdSe core and in
the CdSe shell of the particle [29] (figure 8.1).

Figure 8.1: Composition and band
structure of the onion-like NC. Adapted
from [28]. Band gaps of CdSe core and
CdSe shell are narrower than of the ZnS
shells. This leads to electron and hole lo-
calization in the CdSe regions.

NCs are produced in a stepwise procedure. The
growth process can be stopped at the intermediate steps to monitor the change in the NC
size. The process starts with CdSe cores (figure 8.2(a)). From electron microscopy images
it is clear that onion-like NCs in the stage of growth when the core is overgrown with one
ZnS and one CdSe shell (CdSe/ZnS/CdSe) are significantly larger than pure cores (figure
8.2(b)). Both cores and multi-shell NCs are monodisperse as seen from the TEM images.
Thus, onion-like NCs are not a mixture of two sizes of particles. Average diameters were
determined to be 3.5 nm for the CdSe cores and 5.8 nm for the onion-like CdSe/ZnS/CdSe
sample. This is consistent with the numbers obtained by estimating the diameter of multi-
shell NCs from the thickness of single atomic layers of composing materials. One layer of
ZnS has a thickness of 0.3 nm and of CdSe 0.35 nm. There are three monolayers of ZnS and
one monolayer of CdSe in the NCs displayed in figure 8.2(b). This would result in the final
diameter of 6 nm of the onion-like CdSe/ZnS/CdSe structure.

Onion-like NCs have different optical properties than pure core CdSe NCs. Their absorp-

(a)   CdSe core

(b)   CdSe/ZnS/CdSe

Figure 8.2: TEM images of CdSe cores (a) and the onion-like NCs at the stage of CdSe/ZnS/CdSe (b). Average diameters of the core and multi-shell NCs are 3.5 nm and 5.8 nm respectively.

tion in the blue region is much stronger than the absorption of the pure cores (figure 8.3(a)), which is caused by the presence of the additional CdSe shell. Two peaks are present in the photoluminescence (PL) of multi-shell NCs (figure 8.3(b)). Since the spectral emission of the peak at 612 nm coincides with the emission wavelength of the pure core, the second peak can

(a)

(b)
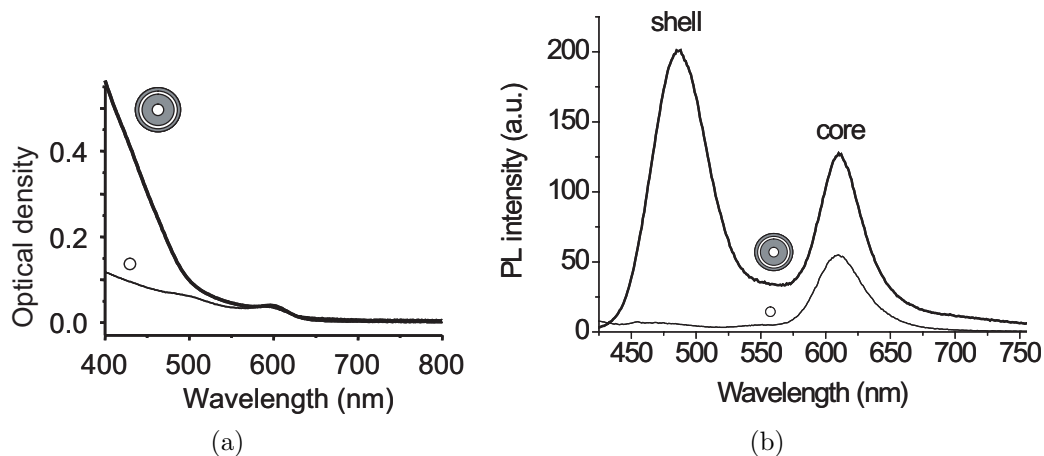
Figure 8.3: Absorption (a) and PL intensity (b) spectra of CdSe cores and CdSe/ZnS/CdSe/ZnS onion-like NCs. The presence of the CdSe shell leads to absorption and emission at shorter wavelengths than for the core.

be attributed to the CdSe shell emission. The reason for this is that ZnS does not to emit or absorb in the visible spectral range, since its bulk band gap is equal to 3.6 eV at 300 K [146], which corresponds to 344 nm.

8.2 Tuning of the nanocrystal emission spectrum

It has been shown that the emission of onion-like NCs can be tuned by changing the diameter of the CdSe core and thicknesses of the ZnS and CdSe shells [28].

The finding of this work is that the color of the core and shell emission can be matched in such a way, that the net color of the PL of the solution appears white (figure 8.4(b)). Furthermore, it was discovered that annealing of the prepared NCs leads to white light shade tuning. When NCs were prepared at 200° C they appeared orange in color (figure 8.4(a)). Further heating for 50 min at 200° C changed the color of NCs to bright white (figure 8.4(b)). When the temperature was increased to 210° C and the NCs were annealed for 15 min, the white color obtained a bluish tinge (figure 8.4(c)).

Figure 8.5 shows the spectra of onion-like NCs, which underwent a different thermal treatment. Analysis of the spectral changes upon annealing shows that it was predominantly the shell emission at 500 nm that changed. The intensity of the core emission at 612 nm stayed the same. Since the total color of the particles is determined by the ratio of the blue and orange components, the net color of the solution of NCs is perceived as changing. The International Commission on Illumination (CIE) coordinates of the emissions of thermally treated NCs illustrate this point clearly (figure 8.6). The diagram shows that the color of white NCs (green triangle) is very close to the point, which is defined as white light by the CIE (gray circle). NCs heated at 210° C for 38 min (blue star) and NCs heated at 210° C
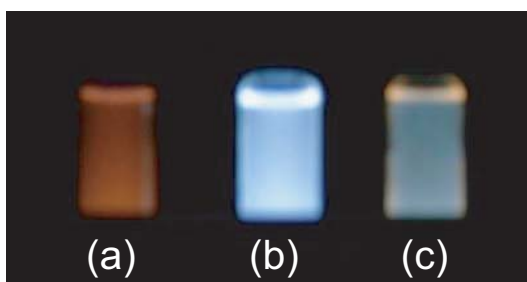
Figure 8.4: Cuvettes with NCs annealed for different periods of time. Heating at 200° C lead to an orange shade of the NC solutions (a). Further heating for 50 min at 200° C produced NCs of white color (b). Annealing at 210° C for 15 min changed the white light shade to bluish (c).

Figure 8.5: Spectra of the emission of NCs annealed at different temperatures. The core emission at 612 nm stayed unchanged upon thermal treatment, while the shell emission intensity at 500 nm varied.
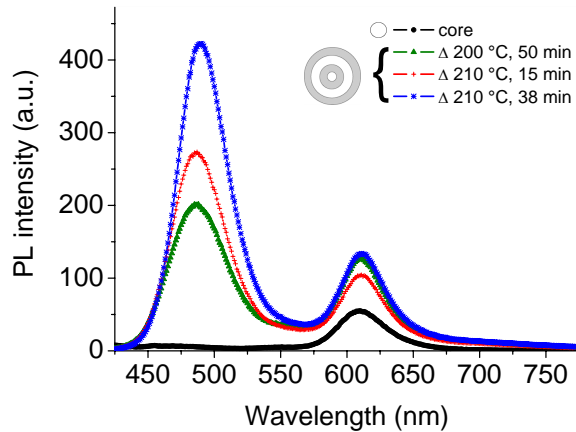
for 15 min (red cross) are close to the white light. The as-prepared (green squares) and core NCs (black circle) are significantly further from the white light point in the red region.

Since NCs do not change their size under the annealing conditions applied in this work, it can be only speculated on the reasons for the observed tuning. It has been reported that the growth of ZnS shells on CdSe is anisotropic and not uniform because these materials have
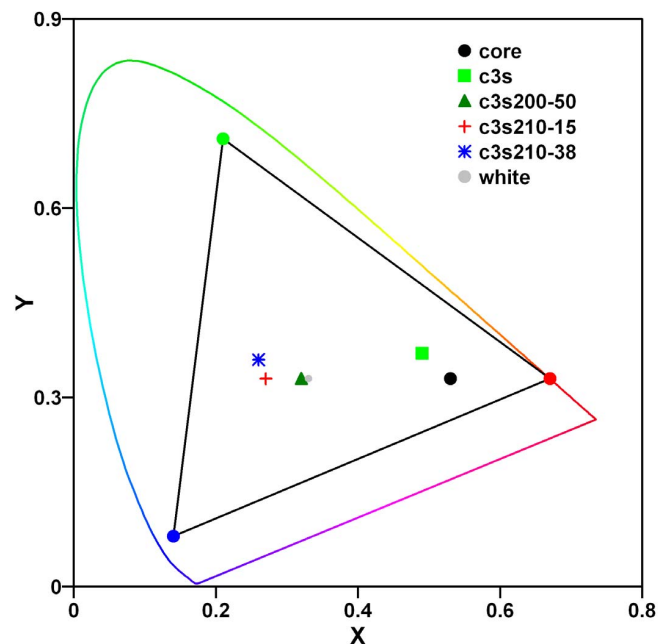
Figure 8.6: CIE coordinates of the emission of NCs annealed at different temperatures [147]. The gray dot in the middle defines the white light. The white light emitting NCs (green triangle) have the net color very close to the standard white light.

117

a big lattice mismatch causing strain between the layers [148]. The (110) plane in wurzite CdSe has 0.22 nm interplanar lattice spacing. The same value for the (103) plane in wurzite ZnS is about 0.175 nm (section 3.3.2). Therefore, the whole system might be sensitive to all factors able to change the arrangement of atoms in these NCs. Atoms on the surface of NCs possibly rearrange upon heating in a way that the CdSe shell becomes better passivated by the outer ZnS layer. This would lead to a stronger emission from the shell, which is what is observed experimentally.

8.3   Intra-nanocrystal energy transfer

Time-resolved investigations were performed in order to study the interactions between the core and shell emission in the onion-like NCs (figure 8.7). The excitation wavelength in these experiments was 400 nm allowing simultaneous excitation of the CdSe core and the CdSe shell. The fluorescence intensity decay of the pure core (red cruve) has an average fluorescence lifetime of 20 ns. The average fluorescence lifetime of the shell measured at 500 nm (green curve) is more than 30 ns. One can notice two components in the fluorescence decay of the core in the onion-like NCs (black curve). The fast component coincides with the fluorescence lifetime of the pure core. The fluorescence decays with practically the same time constant in the first 150 ns in the pure core and in the core of onion-like NCs. However, after 150 ns the core in the onion-like NCs decays slower and follows the decay of the shell. This is an indication of energy transfer from the shell to the core so that the shell keeps feeding
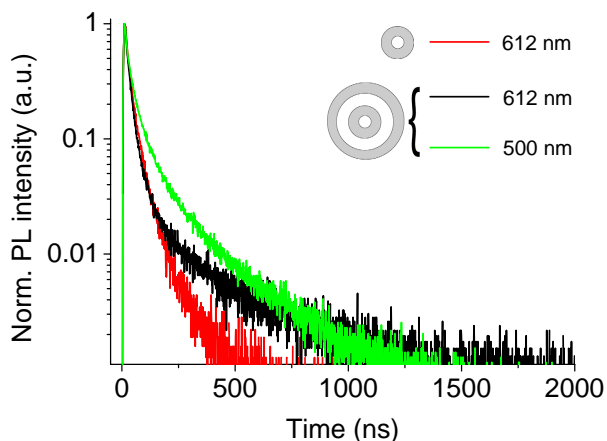
Figure 8.7: Fluorescence decays of pure cores and onion-like NCs at the wavelengths of the core and shell emission. Excitation wavelength was 400 nm allowing to excite both core and shell simultaneously. The fluorescence decay of the core in the multi-shell NC (black curve) follows the decay of the pure core (red curve) in the first 150 ns. After 150 ns the emission continues due to energetic feeding from the shell (green curve).

the core, even after the latter should have decayed completely. Energetically this is the only possible direction of energy transfer since the shell has a wider band gap with an energy of 2.48 eV versus 2.03 eV of the core.

Energy transfer is not the only possible mechanism of interaction between the CdSe core and the CdSe shell. The two are separated by a thin ZnS layer of 0.9 nm thickness. Such a distance can enable separate tunneling of the electron and hole into another CdSe region through the ZnS wall.

One group reported that core-shell coupling happens by tunneling of excitons through the ZnS barrier [149]. Their finding is based on the fact that multi-shell NCs passivated by pyridine molecules, which are hole acceptors, show an attenuated core emission when the NCs are excited below the band edge of the shell. The authors conclude that the Förster mechanism of the core-shell coupling can be excluded, because in their experiment the shell is not optically excited, but still enhances the core emission. According to their publication, the electrons should tunnel even more efficiently than holes that have large effective masses. Therefore the coupling mechanism of the core and shell should be due to exciton tunneling.

In order to verify the hypothesis of energy transfer or exciton tunneling, measurements on the single NC level are necessary. A new publication considered the correlation between the core and the shell emission of a single NC [150]. It was found that a single multi-shell NC does show emission from the core and from the shell. However, the core and the shell do not undergo correlated spectral diffusion on the 200 ms time scale. Therefore, at the current state of investigations it cannot be stated conclusively whether intra-NC energy transfer takes place from the shell to the core and, if it does, what the mechanism is. It is not completely clear whether separate electrons and holes tunnel or the whole exciton tunnels, which is equivalent with the Dexter energy transfer. Further investigations on single onion-like NCs may answer this question.

8.4 Conclusion

In this chapter the optical properties of white light emitting onion-like CdSe/ZnS/CdSe/ZnS NCs were investigated. These particles are interesting for lighting applications. The shade of white light can be controlled by annealing the particles after their synthesis. The change in spectrum upon annealing is due to the variation of the shell emission intensity, while the intensity of the core stays unchanged.

It was shown that multi-shell NCs may involve intra-NC energy transfer from the CdSe shell to the CdSe core. However, only further investigations on the single NC level can allow a conclusive statement about the actual presence of energy transfer and its mechanism.

9. Conclusions and outlook

The central theme of this work is energy transfer with nanoparticles. Energy transfer was investigated in four systems. In the first two systems, energy was transferred from fluorescent dyes to gold nanoparticles (AuNPs). The third system consisted of clustered CdTe nanocrystals (NCs), where energy was transferred from smaller NCs to larger NCs. The fourth system was multi-shell CdSe/ZnS/CdSe/ZnS NCs, for which the CdSe shell is the energy donor and the CdSe core is the energy acceptor.

A particular property of energy transfer to AuNPs is its long range. This allowed the development of the first competitive immunoassay based on fluorescence quenching by AuNPs for a therapeutically relevant small molecule, digoxigenin. The radiative and non-radiative rates of the fluorescent marker molecule quenched by the AuNP were determined with the help of time resolved spectroscopy. It was found that the energy transfer process was mainly responsible for fluorescence quenching. The efficiency of energy transfer was 70 %. The developed immunoassay is sensitive in the therapeutically relevant range providing the linear signal for the concentrations from 1 to 8 nM with the limit of detection of 0.5 nM in buffer.

Furthermore, the first sandwich-type protein immunoassay that uses the advantage of AuNPs as efficient long-distance fluorescence quenchers is reported. The immunoassay was demonstrated for cardiac troponin T, a marker for myocardial infarction. Photophysical studies pointed out the dominant role of energy transfer in fluorescence quenching. The radiative rate stayed practically unchanged. The efficiency of energy transfer reached 95 %, which is higher than in the digoxigenin system because AuNPs with 20 nm diameter quench fluorescence more efficiently than the 10 nm AuNPs used for the digoxigenin test. The limit of detection of 0.02 nM in the sandwich immunoassay in buffer is more than an order of magnitude higher than that of the digoxigenin immunoassay.

Critical parameters for efficient fluorescence quenching were determined. These are the fluorescence lifetime and the quantum yield of the fluorophore and the spectral overlap between its fluorescence spectrum and the absorption spectrum of the AuNPs. It was found that dyes with longer lifetimes and higher quantum efficiencies are quenched more efficiently. It could be seen that the quantum yield and fluorescence lifetime are more significant than the spectral overlap, as long as the latter is still provided. From the time resolved measurements the amount of bound and free fluorescent dyes in the assays have been determined. This finding is of great interest for the homogeneous immunoassays, where free dye is not separated from the assay during the detection and thus contributes to the background fluorescence. If time resolved fluorescence is recorded, the free dye contribution can be removed in the data analysis. This leads to an increase of the signal to noise ratio and makes the assays more sensitive. These findings can be of benefit for the future design of biosensors based on fluorescence quenching by AuNPs.

Cascaded energy transfer was shown in colloidal aggregates of CdTe NCs held together by Ca^{2+} ions. Exciton recycling in the NC clusters was demonstrated, which was previously observed only in layered NC structures [24, 25, 127]. When clustering of NCs is performed through dithiol linker molecules, both energy and charge transfer are responsible for the strong decrease of donor fluorescence and relatively small increase of acceptor fluorescence. An attempt was made to create onion-like clusters, where NCs of different sizes were connected by thiolated DNA in a controlled fashion. Although energy transfer could be observed, these structures did not assemble in an organized way because of unexpected nonspecific DNA adsorption on the surface of CdTe NCs.

In this work evidence is shown that energy transfer can happen within one multi-shell CdSe/ZnS/CdSe/ZnS NCs from the CdSe shell to CdSe core because of the difference in band gaps. Time resolved measurements showed that the fluorescence emission of the core in the multi-shell system lasts longer than in the pure core due to the energetic feeding from the shell to the core.

The immunoassays developed in this work were mainly studied in buffer solutions as proof-of-principle experiments without detailed characterization. The assays in serum are the ones relevant for commercial applications. The sensitivities of the developed methods did not reach the current industrial standards. Therefore, further development is needed before an application in molecular diagnostics is directly feasible. Greater energy transfer efficiency and stronger quenching could be achieved by choosing a marker with a higher spectral overlap of its fluorescence spectrum with the AuNP absorption spectrum. A possible approach to avoid the auto-fluorescence of serum would be to use a phosphorescent dye and detect fluorescence several nano-seconds after the excitation when only the emission of the marker is observed. No systematic study on assays using different sizes of AuNPs was made in this work. According to the Gersten-Nitzan model simulations, larger particles can be more efficient quenchers.

The clusters of CdTe NCs investigated in this work are interesting as artificial light harvesting systems. Here, energy is transported to the largest NCs in the cluster although all NCs are initially excited. This effect is potentially interesting for applications in solar cells. The conjugation method by Ca^{2+} ions developed in this work was used by Gross et al. to induce charge separation in close packed layers of CdTe and CdSe NCs [151], which is a step towards such an application. Further developments could be to design ordered aggregates of NCs, in which particles are spatially arranged according to their sizes. This would require development of selective coupling chemistry.

The exact mechanism of the interaction between the core and the shell in multi-shell CdSe/ZnS/CdSe/ZnS NCs process remains unknown. Although exciton tunneling is proposed in the recent publication [149], the detailed single NC investigations are needed to clarify this issue conclusively. Multi-shell CdSe/ZnS/CdSe/ZnS white light emitting nanocrystals demonstrated within this work are interesting materials for lighting. They can be used as a layer on a blue-emitting polymer, which can be excited electrically [152]. Also, applications of such NCs as multicolor biological labels encoding unique spectral information are feasible.

A. Theoretical binding kinetics calculations

Calculations performed in chapter 6 are based on theoretical work by Zuber et al. [114]. The following system of nonlinear differential equations describes the dynamics of assembly of sandwiches and two species where only one antibody is bound to the analyte (figure A.1):

$$
\begin{aligned}
\frac{d[dpa]}{dt} &= k_{+2}[dp]\left([a]_{tot} - ([pa] + [dpa])\right) + k_{+1}[pa]\left([d]_{tot} - ([dp] + [dpa])\right) \\
&\quad - k_{-2}[dpa] - k_{-1}[dpa] \tag{A.1} \\
\frac{d[pa]}{dt} &= k_{+2}([p]_{tot} - ([dp] + [pa] + [dpa]))([a]_{tot} - ([pa] + [dpa])) \\
&\quad - k_{-2}[pa] - k_{+1}[pa]([d]_{tot} + ([dp] + [dpa])) + k_{-1}[dpa] \tag{A.2} \\
\frac{d[dp]}{dt} &= k_{+1}([p]_{tot} - ([dp] + [pa] + [dpa]))([d]_{tot} - ([dp] + [dpa])) \\
&\quad - k_{-1}[dp] - k_{+2}[dp]([a]_{tot} - ([pa] + [dpa])) + k_{+2}[dpa], \tag{A.3}
\end{aligned}
$$

where d, p, a denote dye-antibody, protein and AuNP-antibody respectively. Concentrations
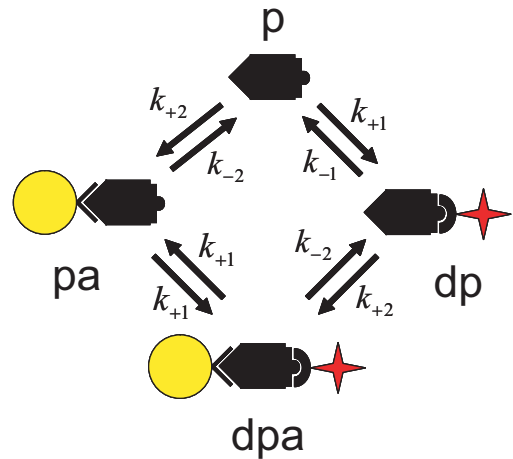
Figure A.1: Scheme of the binding reactions taking place in the sandwich type immunoassay. Association and dissociation constants are ascribed to each binding site.

of separate components are denoted by brackets. k_{+1}, k_{-1}, k_{+2} and k_{-2} are dynamical association and dissociation constants of the reaction. Dynamical constants for both epitopes of TnT were determined on the Biacore device at Roche Diagnostics [85]. The exact values cannot be stated here for non-disclosure reasons.

Abbreviations

a.u. - arbitrary units
AuNP - gold nanoparticle
BSA - bovine serum albumin
CCD - charge-coupled device
CIE - Commission internationale de l'éclairage (International Commission on Illumination)
Dig - digoxigenin
DNA - deoxyribonucleic acid
F(ab')2 - double antigen binding fragment of an antibody
FRET - Förster resonance energy transfer
G - green nanocrystals with emission peak around 550 nm
Ig - immunoglobulin
IgG - immunoglobulin G
LOD - limit of detection
LOQ - limit of quantitation
MPA - mercaptopropionic acid
NC - nanocrystal
Nd:YAG - neodymium-doped yttrium aluminum garnet
NIR - near infrared nanocrystals with emission peak around 730 nm
NP - nanoparticle
OD - optical density
OPO - optical parametric oscillator
PBDT - disodium 1,4 - phenylene-bis (dithiocarbamate)
PL - photoluminescence
PLE - photoluminescence excitation
PMT - photo multiplier
R - red nanocrystals with emission peak around 600 nm
SAXS - small angle X-ray scattering
TCSPC - time correlated single photon counting
TEM - transmission electron microscopy
TGA - thyoglicolic acid
Ti:Sa - titanium-sapphire
TnT - troponin T

List of Figures

List of Tables

Bibliography

[1] G. R. Fleming and G. D. Scholes. Physical chemistry - quantum mechanics for plants. *Nature*, 431(7006):256–257, 2004.

[2] A. Roda, M. Guardigli, E. Michelini, and M. Mirasoli. Nanobioanalytical luminescence: Forster-type energy transfer methods. *Analytical and Bioanalytical Chemistry*, 393(1):109–123, 2009.

[3] T. Virgili, D. G. Lidzey, and D. D. C. Bradley. Efficient energy transfer from blue to red in tetraphenylporphyrin-doped poly(9,9-dioctylfluorene) light-emitting diodes. *Advanced Materials*, 12(1):58–62, 2000.

[4] M. Berggren, A. Dodabalapur, R. E. Slusher, and Z. Bao. Light amplification in organic thin films using cascade energy transfer. *Nature*, 389(6650):466–469, 1997.

[5] Y. X. Liu, M. A. Summers, C. Edder, J. M. J. Frechet, and M. D. McGehee. Using resonance energy transfer to improve exciton harvesting in organic-inorganic hybrid photovoltaic cells. *Advanced Materials*, 17(24):2960–2964, 2005.

[6] Joseph R. Lakowicz. *Principles of fluorescence spectroscopy*. Springer, New York, 3rd edition, 2006.

[7] C. S. Yun, A. Javier, T. Jennings, M. Fisher, S. Hira, S. Peterson, B. Hopkins, N. O. Reich, and G. F. Strouse. Nanometal surface energy transfer in optical rulers, breaking the FRET barrier. *Journal of the American Chemical Society*, 127(9):3115–3119, 2005.

[8] T. L. Jennings, M. P. Singh, and G. F. Strouse. Fluorescent lifetime quenching near d=1.5 nm gold nanoparticles: Probing NSET validity. *Journal of the American Chemical Society*, 128(16):5462–5467, 2006.

[9] J. Seelig, K. Leslie, A. Renn, S. Kuhn, V. Jacobsen, M. van de Corput, C. Wyman, and V. Sandoghdar. Nanoparticle-induced fluorescence lifetime modification as nanoscopic ruler: Demonstration at the single molecule level. *Nano Letters*, 7(3):685–689, 2007.

[10] S. Saini, S. Bhowmick, V. B. Shenoy, and B. Bagchi. Rate of excitation energy transfer between fluorescent dyes and nanoparticles. *Journal of Photochemistry and Photobiology A: Chemistry*, 190(2-3):335–341, 2007.

[11] P. K. Jain, K. S. Lee, I. H. El-Sayed, and M. A. El-Sayed. Calculated absorption and scattering properties of gold nanoparticles of different size, shape, and composition:

Applications in biological imaging and biomedicine. *Journal of Physical Chemistry B*, 110(14):7238–7248, 2006.

[12] E. Dulkeith, M. Ringler, T. A. Klar, J. Feldmann, A. M. Javier, and W. J. Parak. Gold nanoparticles quench fluorescence by phase induced radiative rate suppression. *Nano Letters*, 5(4):585–589, 2005.

[13] P. Anger, P. Bharadwaj, and L. Novotny. Enhancement and quenching of single-molecule fluorescence. *Physical Review Letters*, 96(11), 2006.

[14] E. E. Connor, J. Mwamuka, A. Gole, C. J. Murphy, and M. D. Wyatt. Gold nanoparticles are taken up by human cells but do not cause acute cytotoxicity. *Small*, 1(3):325–327, 2005.

[15] S. Y. Shim, D. K. Lim, and J. M. Nam. Ultrasensitive optical biodiagnostic methods using metallic nanoparticles. *Nanomedicine*, 3(2):215–232, 2008.

[16] K. A. White and N. L. Rosi. Gold nanoparticle-based assays for the detection of biologically relevant molecules. *Nanomedicine*, 3(4):543–553, 2008.

[17] R. Wilson. The use of gold nanoparticles in diagnostics and detection. *Chemical Society Reviews*, 37(9):2028–2045, 2008.

[18] P. G. Van Patten. Enhancement of optical gain in semiconductor nanocrystals through energy transfer. *Journal of Physical Chemistry C*, 112(29):10622–10631, 2008.

[19] N. Tessler, V. Medvedev, M. Kazes, S. H. Kan, and U. Banin. Efficient near-infrared polymer nanocrystal light-emitting diodes. *Science*, 295(5559):1506–1508, 2002.

[20] S. Coe, W. K. Woo, M. Bawendi, and V. Bulovic. Electroluminescence from single monolayers of nanocrystals in molecular organic devices. *Nature*, 420(6917):800–803, 2002.

[21] P. V. Kamat. Quantum dot solar cells. Semiconductor nanocrystals as light harvesters. *Journal of Physical Chemistry C*, 112(48):18737–18753, 2008.

[22] S. Kumar and G. D. Scholes. Colloidal nanocrystal solar cells. *Microchimica Acta*, 160(3):315–325, 2008.

[23] K. E. Sapsford, L. Berti, and I. L. Medintz. Materials for fluorescence resonance energy transfer analysis: Beyond traditional donor-acceptor combinations. *Angew Chem Int Ed Engl*, 45(28):4562–4589, 2006.

[24] T. Franzl, D. S. Koktysh, T. A. Klar, A. L. Rogach, J. Feldmann, and N. Gaponik. Fast energy transfer in layer-by-layer assembled CdTe nanocrystal bilayers. *Applied Physics Letters*, 84(15):2904–2906, 2004.

[25] T. A. Klar, T. Franzl, A. L. Rogach, and J. Feldmann. Super-efficient exciton funneling in layer-by-layer semiconductor nanocrystal structures. *Advanced Materials*, 17(6):769–773, 2005.

[26] J. Lee, A. O. Govorov, and N. A. Kotov. Bioconjugated superstructures of CdTe nanowires and nanoparticles: Multistep cascade Forster resonance energy transfer and energy channeling. *Nano Letters*, 5(10):2063–2069, 2005.

[27] M. H. J. Oh, D. J. Gentleman, and G. D. Scholes. Water soluble quantum dot nanoclusters: Energy migration in artifical materials. *Physical Chemistry Chemical Physics*, 8(43):5079–5085, 2006.

[28] D. Battaglia, B. Blackman, and X. G. Peng. Coupled and decoupled dual quantum systems in one semiconductor nanocrystal. *Journal of the American Chemical Society*, 127(31):10889–10897, 2005.

[29] J. Berezovsky, O. Gywat, F. Meier, D. Battaglia, X. Peng, and D. D. Awschalom. Initialization and read-out of spins in coupled core-shell quantum dots. *Nature Physics*, 2(12):831–834, 2006.

[30] Bernard Valeur. *Molecular fluorescence: principles and applications*. Wiley-VCH, Weinheim; New York, 2002.

[31] J. Perrin and Choucroun. Sensitized fluorescence in a liquid environment (activation transfer by molecular induction). *Comptes rendus hebdomadaires des seances de l'Academie des sciences*, 189:1213–1216, 1929.

[32] T. Forster. Zwischenmolekulare Energiewanderung und Fluoreszenz. *Annalen der Physik*, 2(1-2):55–75, 1948.

[33] G. D. Scholes. Long-range resonance energy transfer in molecular systems. *Annual Review of Physical Chemistry*, 54:57–87, 2003.

[34] K. E. Sapsford, L. Berti, and I. L. Medintz. Fluorescence resonance energy transfer - concepts, applications and advances. *Minerva Biotecnologica*, 16(4):247–273, 2004.

[35] B. Wieb van der Meer, George Coker, and S. Y. Simon Chen. *Resonance energy transfer: theory and data*. VCH, New York, 1994.

[36] D. L. Andrews and A.A. Demidov. *Resonance Energy Transfer*. John Wiley & Sons, 1999.

[37] N. L. Vekshin. *Photonics of biopolymers*. Biological and medical physics series,. Springer, Berlin; New York, 2nd edition, 2002.

[38] D. L. Dexter. A theory of sensitized luminescence in solids. *Journal of Chemical Physics*, 21(5):836–850, 1953.

[39] Uwe Kreibig and Michael Vollmer. *Optical properties of metal clusters*. Springer, Berlin; New York, 1995.

[40] M. Thomas, J. J. Greffet, R. Carminati, and J. R. Arias-Gonzalez. Single-molecule spontaneous emission close to absorbing nanostructures. *Applied Physics Letters*, 85(17):3863–3865, 2004.

[41] S. Kuhn, G. Mori, M. Agio, and V. Sandoghdar. Modification of single molecule fluorescence close to a nanostructure: radiation pattern, spontaneous emission and quenching. *Molecular Physics*, 106(7):893–908, 2008.

[42] F. R. Aussenegg, A. Leitner, M. E. Lippitsch, H. Reinisch, and M. Riegler. Novel aspects of fluorescence lifetime for molecules positioned close to metal-surfaces. *Surface Science*, 189:935–945, 1987.

[43] E. Dulkeith, A. C. Morteani, T. Niedereichholz, T. A. Klar, J. Feldmann, S. A. Levi, F. C. J. M. van Veggel, D. N. Reinhoudt, M. Moller, and D. I. Gittins. Fluorescence quenching of dye molecules near gold nanoparticles: Radiative and nonradiative effects. *Physical Review Letters*, 89(20):203002, 2002.

[44] S. Kuhn, U. Hakanson, L. Rogobete, and V. Sandoghdar. Enhancement of single-molecule fluorescence using a gold nanoparticle as an optical nanoantenna. *Physical Review Letters*, 97(1), 2006.

[45] S. Bhowmick, S. Saini, V. B. Shenoy, and B. Bagchi. Resonance energy transfer from a fluorescent dye to a metal nanoparticle. *Journal of Chemical Physics*, 125(18), 2006.

[46] R. Rossetti and L. E. Brus. Time resolved energy-transfer from electronically excited 3b3u pyrazine molecules to planar Ag and Au surfaces. *Journal of Chemical Physics*, 76(2):1146–1149, 1982.

[47] J. Gersten and A. Nitzan. Spectroscopic properties of molecules interacting with small dielectric particles. *Journal of Chemical Physics*, 75(3):1139–1152, 1981.

[48] R. Ruppin. Decay of an excited molecule near a small metal sphere. *Journal of Chemical Physics*, 76(4):1681–1684, 1982.

[49] H. Chew. Transition rates of atoms near spherical surfaces. *Journal of Chemical Physics*, 87(2):1355–1360, 1987.

[50] J. Y. Yan, W. Zhang, S. Q. Duan, X. G. Zhao, and A. O. Govorov. Optical properties of coupled metal-semiconductor and metal-molecule nanocrystal complexes: Role of multipole effects. *Physical Review B*, 77(16):165301, 2008.

[51] J. Vielma and P. T. Leung. Nonlocal optical effects on the fluorescence and decay rates for admolecules at a metallic nanoparticle. *Journal of Chemical Physics*, 126(19), 2007.

[52] M. Caricato, O. Andreussi, and S. Corni. Semiempirical (ZINDO-PCM) approach to predict the radiative and nonradiative decay rates of a molecule close to metal particles. *Journal of Physical Chemistry B*, 110(33):16652–16659, 2006.

[53] H. Mertens, A. F. Koenderink, and A. Polman. Plasmon-enhanced luminescence near noble-metal nanospheres: Comparison of exact theory and an improved Gersten and Nitzan model. *Physical Review B*, 76(11):115123, 2007.

[54] J.I. Gersten. Theory of fluorophore-metallic surface interactions. In J.R. Lakowicz and C.G. Geddes, editors, *Topics in Fluorescence Spectroscopy: Radiative Decay Engineering*, volume 8, pages 197–221. Springer, 2005.

[55] E. Dulkeith. *Optische Charakterisierung von Hybridsystemen aus Gold Nanopartikeln und Farbstoffmolekülen*. Dissertation, Ludwig-Maximilians-Universität München, 2004.

[56] James P. Gosling. *Immunoassays: a practical approach*. The practical approach series; 228. Oxford University Press, Oxford; New York, 2000.

[57] S. M. Andrew and J. A. Titus. Fragmentation of immunoglobulin g. *Curr Protoc Cell Biol*, Chapter 16:Unit 16 4, 2003.

[58] C. A. Marquette and L. J. Blum. State of the art and recent advances in immunoanalytical systems. *Biosensors & Bioelectronics*, 21(8):1424–1433, 2006.

[59] David Wild. *The Immunoassay handbook*. Nature Pub. Group, London, 2nd edition, 2001.

[60] E.F. Ullman. Homogeneous immunoassays. In David Wild, editor, *The Immunoassay handbook*, pages 177–197. Nature Pub. Group, London, 2nd edition, 2001.

[61] M. Seydack. Immunoassays: basic concepts, physical chemistry and validation. In U. Resch-Genger, editor, *Standardization and quality assurance in fluorescence measurements II: bioanalytical and biomedical applications*, volume 2. Springer, New York, 1st edition, 2008.

[62] N. Gaponik, D. V. Talapin, A. L. Rogach, K. Hoppe, E. V. Shevchenko, A. Kornowski, A. Eychmuller, and H. Weller. Thiol-capping of CdTe nanocrystals: An alternative to organometallic synthetic routes. *Journal of Physical Chemistry B*, 106(29):7177–7185, 2002.

[63] L. E. Brus. On the development of bulk optical-properties in small semiconductor crystallites. *Journal of Luminescence*, 31-2(DEC):381–384, 1984.

[64] A. P. Alivisatos. Perspectives on the physical chemistry of semiconductor nanocrystals. *Journal of Physical Chemistry*, 100(31):13226–13239, 1996.

[65] A. L. Efros and M. Rosen. The electronic structure of semiconductor nanocrystals. *Annual Review of Materials Science*, 30:475–521, 2000.

[66] B. O. Dabbousi, J. Rodriguez-Viejo, F. V. Mikulec, J. R. Heine, H. Mattoussi, R. Ober, K. F. Jensen, and M. G. Bawendi. (CdSe)ZnS core-shell quantum dots: Synthesis and characterization of a size series of highly luminescent nanocrystallites. *Journal of Physical Chemistry B*, 101(46):9463–9475, 1997.

[67] R. J. Ellingson, J. L. Blackburn, P. R. Yu, G. Rumbles, O. I. Micic, and A. J. Nozik. Excitation energy dependent efficiency of charge carrier relaxation and photoluminescence in colloidal InP quantum dots. *Journal of Physical Chemistry B*, 106(32):7758–7765, 2002.

[68] A. M. Kapitonov, A. P. Stupak, S. V. Gaponenko, E. P. Petrov, A. L. Rogach, and A. Eychmuller. Luminescence properties of thiol-stabilized CdTe nanocrystals. *Journal of Physical Chemistry B*, 103(46):10109–10113, 1999.

[69] A. Meijerink. Exciton dynamics and energy transfer processes in semiconductor nanocrystals. In A. L. Rogach, editor, *Semiconductor nanocrystal quantum dots*, pages 277–310. Springer, New York, 2008.

[70] G. D. Scholes and D. L. Andrews. Resonance energy transfer and quantum dots. *Physical Review B*, 72(12), 2005.

[71] Z. Y. Tang, Z. L. Zhang, Y. Wang, S. C. Glotzer, and N. A. Kotov. Self-assembly of CdTe nanocrystals into free-floating sheets. *Science*, 314(5797):274–278, 2006.

[72] G. Allan and C. Delerue. Energy transfer between semiconductor nanocrystals: Validity of Forster's theory. *Physical Review B*, 75(19), 2007.

[73] S. Y. Kruchinin, A. V. Fedorov, A. V. Baranov, T. S. Perova, and K. Berwick. Resonant energy transfer in quantum dots: Frequency-domain luminescent spectroscopy. *Physical Review B*, 78(12):125311, 2008.

[74] C. Curutchet, A. Franceschetti, A. Zunger, and G. D. Scholes. Examining Forster energy transfer for semiconductor nanocrystalline quantum dot donors and acceptors. *Journal of Physical Chemistry C*, 112(35):13336–13341, 2008.

[75] R. Baer and E. Rabani. Theory of resonance energy transfer involving nanocrystals: The role of high multipoles. *Journal of Chemical Physics*, 128(18), 2008.

[76] D. Kim, S. Okahara, M. Nakayama, and Y. Shim. Experimental verification of Forster energy transfer between semiconductor quantum dots. *Physical Review B*, 78(15):153301, 2008.

[77] R. B. Mujumdar, L. A. Ernst, S. R. Mujumdar, C. J. Lewis, and A. S. Waggoner. Cyanine dye labeling reagents - sulfoindocyanine succinimidyl esters. *Bioconjugate Chemistry*, 4(2):105–111, 1993.

[78] M. Cooper, A. Ebner, M. Briggs, M. Burrows, N. Gardner, R. Richardson, and R. West. Cy3B (TM): Improving the performance of cyanine dyes. *Journal of Fluorescence*, 14(2):145–150, 2004.

[79] M. E. Sanborn, B. K. Connolly, K. Gurunathan, and M. Levitus. Fluorescence properties and photophysics of the sulfoindocyanine Cy3 linked covalently to DNA. *Journal of Physical Chemistry B*, 111(37):11064–11074, 2007.

[80] N. Marme, J. P. Knemeyer, M. Sauer, and J. Wolfrum. Inter- and intramolecular fluorescence quenching of organic dyes by tryptophan. *Bioconjugate Chemistry*, 14(6):1133–1139, 2003.

[81] M. L. Ferrer, R. Duchowicz, B. Carrasco, J. G. de la Torre, and A. U. Acuna. The conformation of serum albumin in solution: A combined phosphorescence depolarization-hydrodynamic modeling study. *Biophysical Journal*, 80(5):2422–2430, 2001.

[82] `http://www.rcsb.org/pdb/home/home.do` (accessed May 2009).

[83] C. H. Suelter and M. Deluca. How to prevent losses of protein by adsorption to glass and plastic. *Analytical Biochemistry*, 135(1):112–119, 1983.

[84] U. Schobel, H. J. Egelhaaf, D. Frohlich, A. Brecht, D. Oelkrug, and G. Gauglitz. Mechanisms of fluorescence quenching in donor-acceptor labeled antibody-antigen conjugates. *Journal of Fluorescence*, 10(2):147–154, 2000.

[85] M. Wunderlich. Personal communication. 2007.

[86] `http://familydoctor.org/online/famdocen/home/common/heartdisease/treatment/241.html` (accessed March 2009).

[87] T. W. Smith and E. Haber. Digoxin intoxication - relationship of clinical presentation to serum digoxin concentration. *Journal of Clinical Investigation*, 49(12):2377–2386, 1970.

[88] J. Sarko and C. V. Pollack. Cardiac troponins. *Journal of Emergency Medicine*, 23(1):57–65, 2002.

[89] A. Nichtl. Gold conjugates containing detergent. Patent No: US 6,833,275 B1, Dec. 21 2004.

[90] A. L. Rogach, T. Franzl, T. A. Klar, J. Feldmann, N. Gaponik, V. Lesnyak, A. Shavel, A. Eychmuller, Y. P. Rakovich, and J. F. Donegan. Aqueous synthesis of thiol-capped CdTe nanocrystals: State-of-the-art. *Journal of Physical Chemistry C*, 111(40):14628–14637, 2007.

[91] W. W. Yu, L. H. Qu, W. Z. Guo, and X. G. Peng. Experimental determination of the extinction coefficient of CdTe, CdSe, and CdS nanocrystals. *Chemistry of Materials*, 15(14):2854–2860, 2003.

[92] A. Chemseddine and H. Weller. Highly monodisperse quantum sized CdS particles by size-selective precipitation. *Berichte Der Bunsen-Gesellschaft-Physical Chemistry Chemical Physics*, 97(4):636–637, 1993.

[93] C. B. Murray, D. J. Norris, and M. G. Bawendi. Synthesis and characterization of nearly monodisperse CdE (E = S, Se, Te) semiconductor nanocrystallites. *Journal of the American Chemical Society*, 115(19):8706–8715, 1993.

[94] D. E. Gomez, M. Califano, and P. Mulvaney. Optical properties of single semiconductor nanocrystals. *Physical Chemistry Chemical Physics*, 8(43):4989–5011, 2006.

[95] W. R. Algar and U. J. Krull. Adsorption and hybridization of oligonucleotides on mercaptoacetic acid-capped CdSe/ZnS quantum dots and quantum dot-oligonucleotide conjugates. *Langmuir*, 22(26):11346–11352, 2006.

[96] Image is obtained from `http://commons.wikimedia.org/wiki/File:DNA_As_Structure_Formula_(German).PNG` (accessed February 2009).

[97] Greg T. Hermanson. *Bioconjugate techniques*. Academic Press, San Diego, 1996.

[98] S. Sapra, S. Mayilo, T. A. Klar, A. L. Rogach, and J. Feldmann. Bright white-light emission from semiconductor nanocrystals: by chance and by design. *Advanced Materials*, 19(4):569–572, 2007.

[99] Claude Rulliaere. *Femtosecond laser pulses: principles and experiments*. Advanced texts in physics,. Springer, New York, 2nd edition, 2005.

[100] F. J. Duarte. *Tunable lasers handbook*. Optics and photonics. Academic Press, San Diego, 1995.

[101] T. F. Albrecht, J. H. H. Sandmann, J. Feldmann, W. Stolz, E. O. Gobel, H. Hillmer, R. Losch, and W. Schlapp. Design and application of a femtosecond optical parametric oscillator for time-resolved spectroscopy of semiconductor heterostructures. *Applied Physics B-Lasers and Optics*, 60(5):459–467, 1995.

[102] `http://learn.hamamatsu.com/tutorials/streakcamera/` (accessed May 2009).

[103] S. M. Borisov and O. S. Wolfbeis. Optical biosensors. *Chemical Reviews*, 108(2):423–461, 2008.

[104] R. H. Drost, T. A. Plomp, A. J. Teunissen, A. H. Maes, and R. A. Maes. A comparative study of the homogeneous enzyme immunoassay (EMIT) and two radioimmunoassays (RIA's) for digoxin. *Clin Chim Acta*, 79(3):557–67, 1977.

[105] C. X. Zhang, H. L. Qi, and M. N. Zhang. Homogeneous electrogenerated chemiluminescence immunoassay for the determination of digoxin employing Ru(bpy)(2)(dcbpy)NHS and carrier protein. *Luminescence*, 22(1):53–59, 2007.

[106] K. Abicht, H. Kreutzmann, and C. Luley. Determination of the digoxin concentration with the Elecsys digoxin immunoassay. Comparison with 3 different immunoassay methods. *Laboratoriumsmedizin*, 23:156–160, 1999.

[107] A. Dasgupta and P. Datta. Rapid detection of oleander poisoning using digoxin immunoassays - comparison of five assays. *Therapeutic Drug Monitoring*, 26(6):658–663, 2004.

[108] M. Mandy, M. Manchon, R. Meley, J.C. Eynard, and D. Grafmeyer. Dosage de la digoxine: exploitation de 10 ans de controles interlaboratoires. *Annales de biologie clinique*, 63(3):345–349, 2005.

[109] R. S. Nezlin. *The immunoglobulins: structure and function.* Academic Press, San Diego, 1998.

[110] R. C. Valentin and N. M. Green. Electron microscopy of an antibody-hapten complex. *Journal of Molecular Biology*, 27(3):615–617, 1967.

[111] E. F. Ullman, M. Schwarzberg, and K. E. Rubenstein. Fluorescent excitation transfer immunoassay - general method for determination of antigens. *Journal of Biological Chemistry*, 251(14):4172–4178, 1976.

[112] G. Mathis. Rare-earth cryptates and homogeneous fluoroimmunoassays with human sera. *Clinical Chemistry*, 39(9):1953–1959, 1993.

[113] O. D. Wei, M. Lee, X. Yu, E. K. Lee, G. H. Seong, J. Choo, and Y. W. Cho. Development of an open sandwich fluoroimmunoassay based on fluorescence resonance energy transfer. *Analytical Biochemistry*, 358(1):31–37, 2006.

[114] E. Zuber, G. Mathis, and J. P. Flandrois. Homogeneous two-site immunometric assay kinetics as a theoretical tool for data analysis. *Analytical Biochemistry*, 251(1):79–88, 1997.

[115] R. F. Dutra and L. T. Kubota. An SPR immunosensor for human cardiac troponin T using specific binding avidin to biotin at carboxymethyldextran-modified gold chip. *Clinica Chimica Acta*, 376(1-2):114–120, 2007.

[116] H. A. Katus, A. Remppis, S. Looser, K. Hallermeier, T. Scheffold, and W. Kubler. Enzyme linked immuno assay of cardiac troponin T for the detection of acute myocardial infarction in patients. *J Mol Cell Cardiol*, 21(12):1349–53, 1989.

[117] M. Muller-Bardorff, T. Rauscher, H. Kampmann, S. Schoolmann, F. Laufenberg, D. Mangold, R. Zerback, A. Remppis, and H. A. Katus. Quantitative bedside assay for cardiac troponin T: A complementary method to centralized laboratory testing. *Clinical Chemistry*, 45(7):1002–1008, 1999.

[118] H. Baum, S. Braun, W. Gerhardt, G. Gilson, G. Hafner, M. MullerBardorff, W. Stein, G. Klein, C. Ebert, K. Hallermayer, and H. A. Katus. Multicenter evaluation of a second-generation assay for cardiac troponin T. *Clinical Chemistry*, 43(10):1877–1884, 1997.

[119] D. Hermsen, F. Apple, L. Garcia-Beltran, A. Jaffe, B. Karon, E. Lewandrowski, A. Muhlbacher, R. Muller, J. Ordonez, F. Pagani, M. Panteghini, T. Plecko, and J. Jarausch. Results from a multicenter evaluation of the 4th generation Elecsys Troponin T assay. *Clin Lab*, 53(1-2):1–9, 2007.

[120] H. J. Gruber, C. D. Hahn, G. Kada, C. K. Riener, G. S. Harms, W. Ahrer, T. G. Dax, and H. G. Knaus. Anomalous fluorescence enhancement of Cy3 and Cy3.5 versus anomalous fluorescence loss of Cy5 and Cy7 upon covalent linking to IgG and noncovalent binding to avidin. *Bioconjugate Chemistry*, 11(5):696–704, 2000.

[121] A. S. Susha, A. M. Javier, W. J. Parak, and A. L. Rogach. Luminescent CdTe nanocrystals as ion probes and pH sensors in aqueous solutions. *Colloids and Surfaces A: Physicochemical and Engineering Aspects*, 281(1-3):40–43, 2006.

[122] S. A. Crooker, J. A. Hollingsworth, S. Tretiak, and V. I. Klimov. Spectrally resolved dynamics of energy transfer in quantum-dot assemblies: Towards engineered energy flows in artificial materials. *Physical Review Letters*, 89(18):186802, 2002.

[123] S. Mayilo, J. Hilhorst, A. S. Susha, C. Hohl, T. Franzl, T. A. Klar, A. L. Rogach, and J. Feldmann. Energy transfer in solution-based clusters of CdTe nanocrystals electrostatically bound by calcium ions. *Journal of Physical Chemistry C*, 112(37):14589–14594, 2008.

[124] Y. Ebenstein, T. Mokari, and U. Banin. Fluorescence quantum yield of CdSe/ZnS nanocrystals investigated by correlated atomic-force and single-particle fluorescence microscopy. *Applied Physics Letters*, 80(21):4033–4035, 2002.

[125] D. V. Talapin, A. L. Rogach, E. V. Shevchenko, A. Kornowski, M. Haase, and H. Weller. Dynamic distribution of growth rates within the ensembles of colloidal II-VI and III-V semiconductor nanocrystals as a factor governing their photoluminescence efficiency. *Journal of the American Chemical Society*, 124(20):5782–5790, 2002.

[126] C. R. Kagan, C. B. Murray, and M. G. Bawendi. Long-range resonance transfer of electronic excitations in close-packed CdSe quantum-dot solids. *Physical Review B*, 54(12):8633–8643, 1996.

[127] T. Franzl, T. A. Klar, S. Schietinger, A. L. Rogach, and J. Feldmann. Exciton recycling in graded gap nanocrystal structures. *Nano Letters*, 4(9):1599–1603, 2004.

[128] R. Osovsky, A. Shavel, N. Gaponik, L. Amirav, A. Eychmuller, H. Weller, and E. Lifshitz. Electrostatic and covalent interactions in CdTe nanocrystalline assemblies. *Journal of Physical Chemistry B*, 109(43):20244–20250, 2005.

[129] R. Koole, P. Liljeroth, C. D. Donega, D. Vanmaekelbergh, and A. Meijerink. Electronic coupling and exciton energy transfer in CdTe quantum-dot molecules. *Journal of the American Chemical Society*, 128(32):10436–10441, 2006.

[130] R. Koole, B. Luigjes, M. Tachiya, R. Pool, T. J. H. Vlugt, C. D. M. Donega, A. Meijerink, and D. Vanmaekelbergh. Differences in cross-link chemistry between rigid and flexible dithiol molecules revealed by optical studies of CdTe quantum dots. *Journal of Physical Chemistry C*, 111(30):11208–11215, 2007.

[131] J. M. Wessels, H. G. Nothofer, W. E. Ford, F. von Wrochem, F. Scholz, T. Vossmeyer, A. Schroedter, H. Weller, and A. Yasuda. Optical and electrical properties of three-dimensional interlinked gold nanoparticle assemblies. *Journal of the American Chemical Society*, 126(10):3349–3356, 2004.

[132] M. Heilemann, P. Tinnefeld, G. S. Mosteiro, M. G. Parajo, N. F. Van Hulst, and M. Sauer. Multistep energy transfer in single molecular photonic wires. *Journal of the American Chemical Society*, 126(21):6514–6515, 2004.

[133] G. Sanchez-Mosteiro, E. M. H. P. van Dijk, J. Hernando, M. Heilemann, P. Tinnefeld, M. Sauer, F. Koberlin, M. Patting, M. Wahl, R. Erdmann, N. F. van Hulst, and M. F. Garcia-Parajo. DNA-based molecular wires: Multiple emission pathways of individual constructs. *Journal of Physical Chemistry B*, 110(51):26349–26353, 2006.

[134] A.M. Pyle and J.K. Barton. Probing nucleic acids with transition metal complexes. In Stephen J. Lippard, editor, *Progress in Inorganic Chemistry*, volume 38, pages 413–476. John Wiley & Sons, Inc., 1990.

[135] J.L. Coffer, S.R. Bigham, R.F. Pinizzotto, and H. Yang. Characterization of quantum-confined CdS nanocrystallites stabilized by deoxyribonucleic acid (DNA). *Nanotechnology*, 3:69–76, 1992.

[136] Q. Xu, J. H. Wang, Z. Wang, Z. H. Yin, Q. Yang, and Y. D. Zhao. Interaction of CdTe quantum dots with DNA. *Electrochemistry Communications*, 10(9):1337–1339, 2008.

[137] W. R. Algar and U. J. Krull. Towards multi-colour strategies for the detection of oligonucleotide hybridization using quantum dots as energy donors in fluorescence resonance energy transfer (FRET). *Analytica Chimica Acta*, 581(2):193–201, 2007.

[138] N. Ma, E. H. Sargent, and S. O. Kelley. One-step DNA-programmed growth of luminescent and biofunctionalized nanocrystals. *Nat Nanotechnol*, 4(2):121–5, 2009.

[139] G. P. Mitchell, C. A. Mirkin, and R. L. Letsinger. Programmed assembly of DNA functionalized quantum dots. *Journal of the American Chemical Society*, 121(35):8122–8123, 1999.

[140] D. J. Zhou, J. D. Piper, C. Abell, D. Klenerman, D. J. Kang, and L. M. Ying. Fluorescence resonance energy transfer between a quantum dot donor and a dye acceptor attached to DNA. *Chemical Communications*, (38):4807–4809, 2005.

[141] R. Gill, I. Willner, I. Shweky, and U. Banin. Fluorescence resonance energy transfer in CdSe/ZnS-DNA conjugates: Probing hybridization and DNA cleavage. *Journal of Physical Chemistry B*, 109(49):23715–23719, 2005.

[142] S. M. Wu, X. Zha, Z. L. Zhang, H. Y. Xie, Z. Q. Tian, J. Peng, Z. X. Lu, D. W. Pang, and Z. X. Xie. Quantum-dot-labeled DNA probes for fluorescence in situ hybridization (FISH) in the microorganism Escherichia coli. *Chemphyschem*, 7(5):1062–1067, 2006.

[143] I. L. Medintz, L. Berti, T. Pons, A. F. Grimes, D. S. English, A. Alessandrini, P. Facci, and H. Mattoussi. A reactive peptidic linker for self-assembling hybrid quantum dot-DNA bioconjugates. *Nano Letters*, 7(6):1741–1748, 2007.

[144] D. J. Zhou, L. M. Ying, X. Hong, E. A. Hall, C. Abell, and D. Klenerman. A compact functional quantum dot-DNA conjugate: Preparation, hybridization, and specific label-free DNA detection. *Langmuir*, 24(5):1659–1664, 2008.

[145] P. Reiss, M. Protiere, and L. Li. Core/shell semiconductor nanocrystals. *Small*, 5(2):154–68, 2009.

[146] Ben G. Streetman and Sanjay Banerjee. *Solid state electronic devices*. Prentice Hall series in solid state physical electronics. Pearson/Prentice Hall, Upper Saddle River, N.J., 6th edition, 2006.

[147] CIE coordinates were calculated using software GoCIE obtained from `http://www.geocities.com/krjustin/gocie.html` (accessed January 2006).

[148] Z. H. Yu, L. Guo, H. Du, T. Krauss, and J. Silcox. Shell distribution on colloidal CdSe/ZnS quantum dots. *Nano Letters*, 5(4):565–570, 2005.

[149] E. A. Dias, S. L. Sewall, and P. Kambhampati. Light harvesting and carrier transport in core/barrier/shell semiconductor nanocrystals. *Journal of Physical Chemistry C*, 111(2):708–713, 2007.

[150] E. A. Dias, A. F. Grimes, D. S. English, and P. Kambhampati. Single dot spectroscopy of two-color quantum dot/quantum shell nanostructures. *Journal of Physical Chemistry C*, 112(37):14229–14232, 2008.

[151] D. Gross, A. S. Susha, T. A. Klar, E. Da Como, A. L. Rogach, and J. Feldmann. Charge separation in type II tunneling structures of close-packed CdTe and CdSe nanocrystals. *Nano Letters*, 8(5):1482–1485, 2008.

[152] S. Nizamoglu, E. Mutlugun, O. Akyuz, N. K. Perkgoz, H. V. Demir, L. Liebscher, S. Sapra, N. Gaponik, and A. Eychmueller. White emitting CdS quantum dot nanoluminophores hybridized on near-ultraviolet LEDs for high-quality white light generation and tuning. *New Journal of Physics*, 10, 2008.